# Stony Brook University

# Turbulent Combustion Study of Scramjet Problem

A Dissertation Presented

by

**Xiaoxue Gong**

to

The Graduate School

in Partial Fulfillment of the

Requirements

for the Degree of

**Doctor of Philosophy**

in

**Applied Mathematics and Statistics**

Stony Brook University

**August 2015**

**Stony Brook University**

The Graduate School

**Xiaoxue Gong**

We, the dissertation committee for the above candidate for the
Doctor of Philosophy degree, hereby recommend
acceptance of this dissertation.

**James Glimm - Dissertation Advisor**
**Professor, Department of Applied Mathematics and Statistics**

**Robert Harrison - Chairperson of Defense**
**Professor, Department of Applied Mathematics and Statistics**

**Roman Samulyak - Member**
**Professor, Department of Applied Mathematics and Statistics**

**Alan C. Calder - Outside Member**
**Professor, Department of Physics and Astronomy**

This dissertation is accepted by the Graduate School.

Charles Taber
Dean of the Graduate School

Abstract of the Dissertation

# Turbulent Combustion Study of Scramjet Problem

by

**Xiaoxue Gong**

**Doctor of Philosophy**

in

**Applied Mathematics and Statistics**

Stony Brook University

**2015**

In this thesis we study the turbulent mixing and turbulent combustion in a model scramjet combustor with a Large Eddy Simulation (LES) strategy. LES resolves the large and energetic motions while the small subscale motions are modeled. Here the filtered Navier-Stokes equations are solved by a fifth-order finite difference Weighted-Essentially Non-Oscillatory (WENO) scheme dimension by dimension. Subgrid terms are closed by the dynamic Smagorinsky model. Chemical source terms are calculated directly using a finite rate chemistry model with a reduced chemistry mechanism. The equilibrium turbulent boundary layer model of J. Larsson is used to calculate the shear stress

and heat flux at the wall. Inflow turbulent is generated by the digital filtering method.

The main result is a methodology to predict the mesh convergence for three-dimensional turbulent combustion simulation, based on a less expensive suites of one-dimensional and two-dimensional simulations. We first determine the grid requirements for finite rate chemistry with detailed and reduced chemical mechanism respectively in the context of one-dimensional simulations. These criteria are verified through simulation in a two-dimensional context and refined with corrections due to turbulent transport. They are then applied to three-dimensional simulations. A grid sensitivity study of the turbulent boundary layer is conducted in a 2D context.

Simulation results are validated through comparison with a simulation of the same problem conducted by J. Larsson, using a different methodology and by comparison to experiments performed at Stanford University.

*To my parents and my husband*

# Table of Contents

# List of Figures

# List of Tables

# Acknowledgements

I would like to express my special appreciation and sincere gratitude to my advisor, Professor James Glimm, who gave me patient guidance and inspiring suggestions on my research. Professor Glimm is a tremendous advisor, who is always willing to spend time to help his student to overcome difficulties in research and to grow from a student to a professional researcher. Professor Glimm is also a role model. The devotion and enthusiasm he has for research motivate me in my pursuit of Ph.D degree and future career. I feel proud to be his student and enjoy the five-years time worked under the guidance of Professor Glimm.

I would like to thanks Professor Robert Harrison, Roman Samulyak and Alan Calder for being my dissertation committee. You are the most outstanding professors in your field of specialization. I feel grateful to have you in my defense committee. I am also thankful for your valuable suggestions on my thesis.

I want to thanks the Army Research Organization for their support of this research through grants W911NF1310249 and W911NF1410482. Same thanks goes to U.S. Department of Energy via Los Alamos National Laboratory and Center for Turbulence Research of Stanford University. I want to express

special thanks to Professor Johan Larsson for sharing information and inspiring discussions.

Many thanks to my group members and my friends: Dr. Tulin Karman, Ying Xu, Hyunkyung Lim, Vinay Mahadeo and Ryan Kaufman. Among them, I want to express my special gratitude towards Tulin and Ryan for their time on reviewing my thesis and presentation.

I also want to thanks Dr. Houman in Google. I spent a wonderful summer in his team last year as an intern. He inspired me to use my math and statistical skills to find solutions for industry problems.

Lastly, I want to thanks my parents for their unconditional love and support. I want to express my special thanks to my husband, Youlong, for his love, patience, encouragement and support during my Ph.D study and during our long distance relationship.

# Chapter 1

# Introduction

## 1.1 Backgound

A jet engine is an air breathing engine which carries fuel on board and uses oxygen ingested from the atmosphere for combustion. There are three kinds of jet engine: turbo-machinery based jet engines, ramjets, and supersonic combustion ramjets (scramjets). The specific impulses of these jet engines are shown in Fig 1.1. This figure indicates the advantage of scramjet when the Mach number is above six. The scramjet is the most promising engine for hypersonic flight. It has been a very hot research area for last several decades.

The schematic plot of HyShot-II, a scramjet combustion chamber, is shown in Fig 1.2. The structure of the scramjet combustion chamber is simple. The front part (inlet ramp) of the engine generates the shocks which compress the inflow supersonic air. The velocity of the inflow air decreases as a result of the compression but it is still supersonic. Meanwhile, the fuel is injected (transversely in HyShot II) into this high enthalpy crossflow. After the fuel

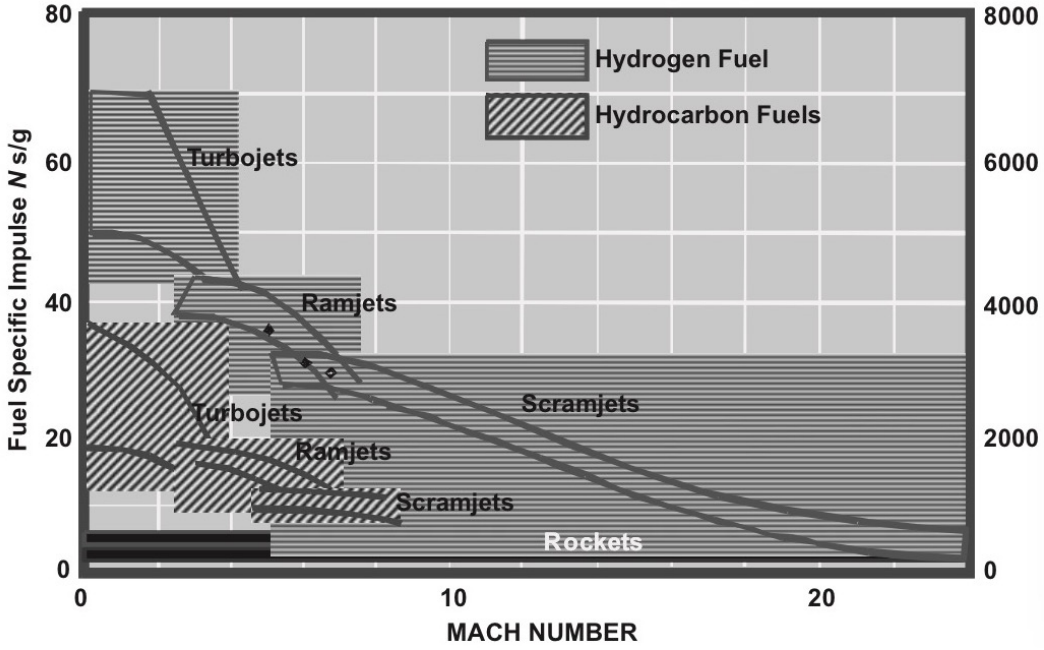


Figure 1.1: Specific impulses of three kinds of jets and rocket [60].

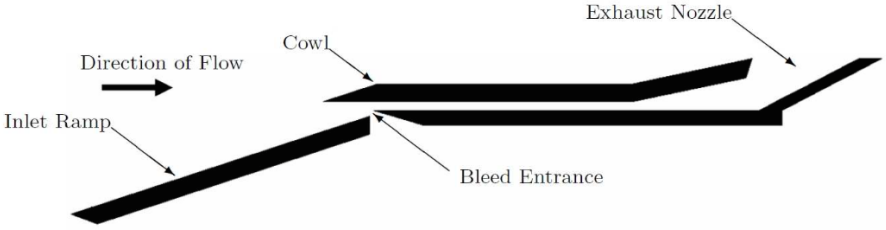


Figure 1.2: A schematic diagram for HyShot-II Model (Image source Gardner [23] ).

mixes with the air, it burns and expands to the outlet and generates thrust for the aircraft. There is no ignition device needed. Although the structure is simple, the physical phenomena in the combustion chamber are complex due to shock waves, chemical reactions, turbulent mixing and turbulent boundary layers. These effects are nonlinear and couples with each other. This fact makes the prediction and simulation of the scramjet combustion difficult.

The research for scramjet engine has stretched over several decades. The evolution of scramjet development can be found in a review paper of Fry [17]. Many flight and ground experiments have been conducted. Among them, the HyShot II scramjet engine designed by the University of Queensland, Australia, was successfully launched in 2002. The HEG facility of the German Aerospace Agency DLR has carried out HyShot II scramjet ground tests [23].

This thesis focuses on the numerical simulation of a model scramjet combustor designed by Gamba [21]. Gamba carried out experiments to investigate the mixing, ignition, and combustion in supersonic combustion in the compact, optically accessible scramjet combustor model at Stanford 6" Expansion Tube Facility. Fig. 1.3 shows the configuration plot of the model scramjet combustor. The diagnostic techniques of this experiment include the PLIF (Planar Laser Induced Fluorescence) imaging of OH concentration on orthogonal planes, the Chemiluminescence imaging of $OH^*$ and the pressure measurement at the top wall.

Besides flight and ground experiments, numerous Computational Fluid Dynamic (CFD) techniques have been used to understand the physics inside scramjet combustion chamber. The fuel choices in these simulations include

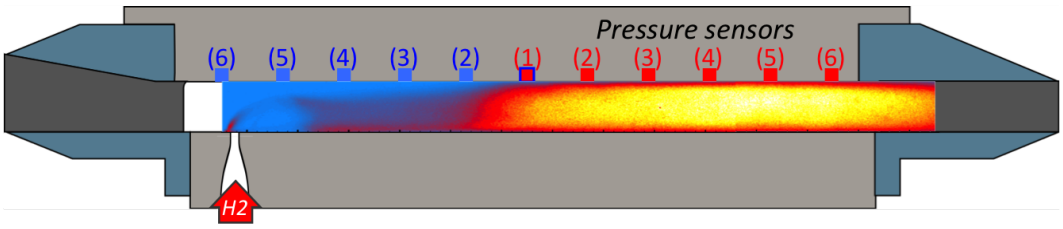


Figure 1.3: A diagram for the model scramjet combustor (Image source Gamba [21]).

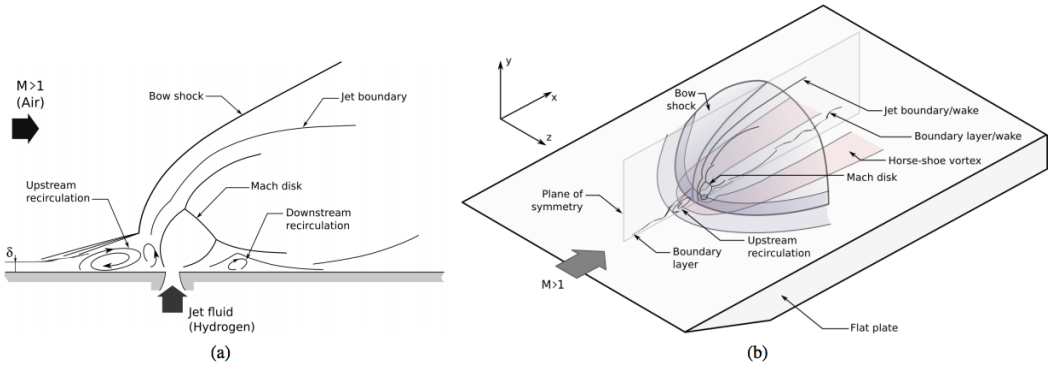


Figure 1.4: A schematic plot of the transverse jet in supersonic cross flow (Image source Gamba [20] ).

hydrocarbon fuel and hydrogen fuel. For simulation approach, both Reynolds Average Navier-Stokes (RANS) approach [14, 18, 44, 49] and Large Eddy Simulation (LES) approach [6, 36, 29] are applied. Various combustion models are used with either detailed or reduced chemistry mechanism. The most popular method among them is the flamelet method.

One classical flow structure in scramjet simulation is the transverse jet in supersonic cross flow (JICF). Fig. 1.4 is the schematic plot of JICF which has many flow features [20]: the vortical structures generated by the interaction

of the jet with the crossflow, a bow shock produced by the blockage effect of the jet, the upstream recirculation region caused by the bow-shock-induced boundary layer separation, and another recirculation region downstream of the injector. One important parameter, which determine the characteristics of JICF, is the jet-to-crossflow momentum flux ratio J defined as

$$J = \frac{\rho_{\text{jet}} u_{\text{jet}}^2}{\rho_\infty u_\infty^2} \tag{1.1}$$

The jet exit Reynolds number defined as

$$Re_{\text{D}} = \rho_{\text{jet}} U_{\text{jet}} D / \mu_{\text{jet}} \tag{1.2}$$

is another important parameter. Here D is the diameter of $H_2$ injector. Gamba [20] used the OH PLIF imaging to investigate the reaction in JICF at J = 5.0. He measured the thickness of the diffusion flame (OH layer) near the injector and found the thickness of the flame is between 300 - 900 microns. The Kolmogorov length scale in the scramjet combustor is approximately 10 microns (the estimation of the Kolmogorov length scale is in Sec. 5.1). Thus the Kolmogorov scale is much smaller than the chemical scale. Thus We have the numerical capacity to resolve chemistry while we do not have the capacity to resolve turbulence. The fact leads us to choose the "finite rate chemistry" method. We will further discuss it in Chap. 4.

## 1.2 Thesis Structure

This thesis presents our work of the numerical simulation of the model scramjet combustor by Gamba. It is organized as follows.

The first chapter explains the background of scramjet simulation.

The second chapter includes the major theories, governing equations and numerical methods used in scramjet simulation. Basic knowledge of turbulence and three turbulence modelling methodologies are introduced. The governing Naiver-Stokes equations of compressible fluid are covered. We explain the main modules in the compressible Frontier code we use to simulate model scramjet combustor:

1. The hyperbolic module: The numerical discretization scheme for solving the hydrodynamics dimension by dimension.

2. The EOS module: The Equation of State and transport properties.

3. The parabolic module: Molecular transport effects and subgrid scaled terms.

4. Turbulent inflow generation.

The third chapter focuses on the implementation and grid sensitivity study of the turbulent boundary layer through suits of two dimensional simulation.

The fourth chapter studies the chemical combustion in the combustion chamber. The finite rate chemistry mechanism with both detailed and reduced chemical mechanism is explored. Then grid sensitivity study of one-

dimensional laminar flames and two-dimensional diffusional flames are conducted. The thickened flame model is also explored.

The fifth chapter shows the result and analysis of scramjet 3D simulation, which applies the resolution predicted from the third and fourth chapter. The scramjet 3D simulation result is compared with the experiment and the Larsson's simulation.

The sixth chapter concludes the results in this thesis and makes suggestion for future study.

# Chapter 2

# Turbulence Theory, Governing Equations and Numerical Methods

## 2.1 Introduction to Turbulence

Turbulence is "unsteady, periodic motion in which all three velocity components fluctuate, mixing matter, momentum, and energy." Many flows in nature are turbulent, see Fig. 2.1. Turbulent flows occur at high Reynolds numbers, when different scales of eddies arise from the complex interaction between the viscous terms and the inertia terms in the momentum equations [19]. Here, Reynolds number is defined as the ratio of inertial stress and viscous stress and can often be expressed as $uL/\nu$ ($u$ is velocity, $L$ is character length and $\nu$ is the viscosity coefficient).

At low Reynolds numbers, flows are laminar. Transitions from laminar flow to turbulence flow occur between Re = 2000 to Re = 13000. There are several characteristics of turbulence [64].

1. Randomness. Turbulent flows are chaotic and can not be described by

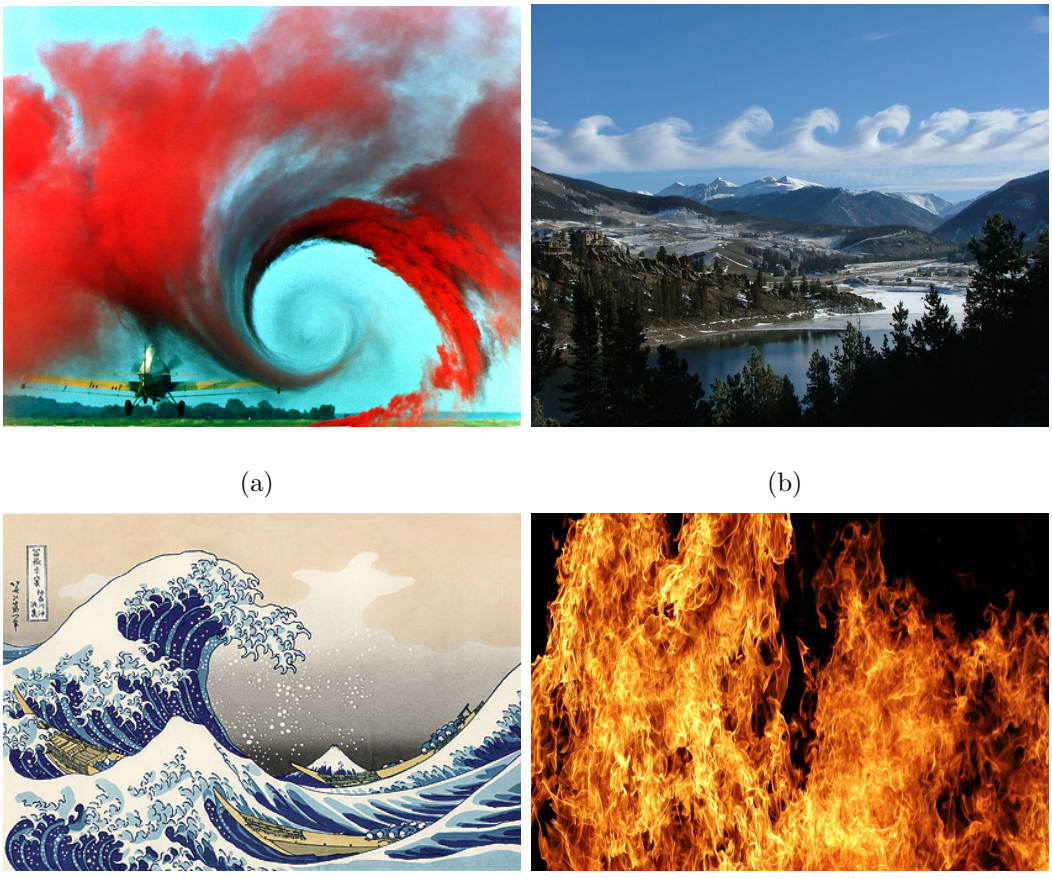

(a) (b)

(c) (d)

Figure 2.1: Turbulence in nature, (a) wake behind the plane, (b) cloud under Kelvin-Helmholtz instability, (c) “The Great Wave Off Kanagawa”, (d) turbulent flame.

deterministic methods. Instead, turbulent flows are usually described through statistical approaches.

2. Diffusivity. The diffusivity of turbulence speeds up the mixing , the momentum, heat and mass transfer process. The diffusivity of turbulent is very important in many applications, for example, the turbulence combustion process of scramjet chamber.

3. Dissipation. The viscous shear stress transfers energy from kinetic energy to the internal energy of the flow. Thus a sustained turbulence flow requires a continuous supply of energy.

The existence of turbulence has a large influence on the flow. For example, the near wall turbulence increases the shear stress at the wall; the turbulence in combustion chamber speeds up the mixing and the chemical reactions.

Although turbulence is an important phenomenon, understanding turbulence is difficult. Actually, turbulence was considered by Nobel Laureate and Richard Feynman to be "one of the biggest outstanding problems in classical physics." Two important theories of turbulence are the *energy cascade* and the *Kolmogorov hypotheses*.

The turbulent flow field contains eddies with different sizes. The large eddies have most of kinetic energy. They are unstable and transfer the energy to smaller eddies. The smaller eddies follow similar processes, and transfer the energy to even smaller eddies. The *energy cascade* is the process that the kinetic energy that enters the turbulence at the large scale eddies is transferred to smaller and smaller scale eddies, until the Reynolds number of these eddies

is small enough and these eddies are stable. The kinetic energy of the smallest scale eddies is dissipated away through viscosity and convert into heat. This process is summarized by L.F. Richardson [58] as:

*Big whirls have little whirls*
*Which feed on their velocity;*
*And little whirls have lesser whirls,*
*And so on to viscosity*
*in the molecular sense.*

We denote the energy dissipation rate at which turbulence kinetic energy is converted into thermal internal energy as $\epsilon \equiv \nu \frac{\partial u_i^{'}}{\partial x_k} \frac{\partial u_i^{'}}{\partial x_k}$.

The Kolmogorov's hypothesis is based on three hypothesis together with dimensional arguments. The first hypothesis of similarity states that "in every turbulent flow at sufficiently high Reynolds number, the statistics of the small scale motions ($l < l_{EI}$) have a universal form that is uniquely determined by $\epsilon$ and $\nu$." Here $l_{EI}$ is the length scale which separates the large, energetic, geometric dependent scales from small universal scales. The size range $l < l_{EI}$ is called the universal equilibrium range. The range where $l > l_{EI}$ is called the energy containing range.

The second hypothesis of similarity states that " in every turbulent flow at sufficiently high Reynolds number, the statistics of the motions of scale $l$ in the range $l_0 \gg l \gg \eta$ have a universal form that is uniquely determined by $\epsilon$ and independent of $\nu$." This hypothesis splits the universal equilibrium range into two subranges: the inertial subrange where motions are uniquely

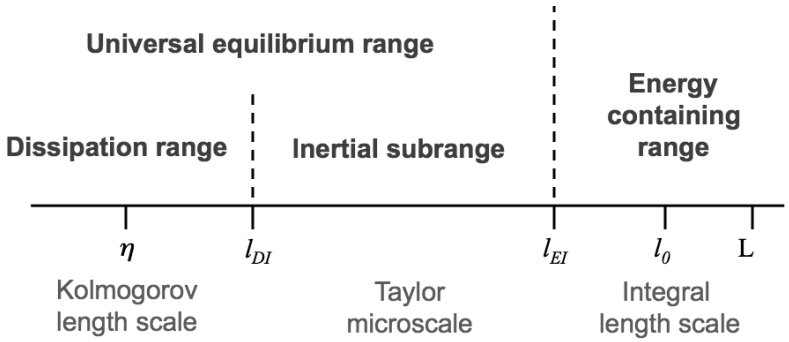


Figure 2.2: Turbulence length scales [57]

determined by $\epsilon$ and the dissipation range where motions are affected by viscousity. Different length scales are related to these three ranges of turbulence, summarized as Fig 2.2.

The large and energetic eddies have a length scale of the same order with the problem geometry, denoted by $l$ and velocity length scale of $u_c$. The Kolmogorov length scale, velocity scale and time scale are:

$$\text{length scale: } \eta_k = \left(\frac{\nu^3}{\epsilon}\right)^{1/4} \tag{2.1}$$

$$\text{velocity scale: } u_\eta = \left(\nu^3\epsilon\right)^{1/4} \tag{2.2}$$

$$\text{time scale: } \tau_\eta = \left(\frac{\nu}{\epsilon}\right)^{1/2} \tag{2.3}$$

The ratios of the Kolmogorov scales to the integral scales are related to the Reynolds number by

$$\frac{\eta}{l} \sim Re^{-3/4} \tag{2.4}$$

$$\frac{u_\eta}{u_c} \sim Re^{-1/4} \tag{2.5}$$

$$\frac{\tau_\eta}{\tau} \sim Re^{-1/2} \tag{2.6}$$

The intermediate scales in the inertial range of turbulence are called as the Taylor scales $\lambda_T$. The ratio of Taylor scales to the Kolmogorov scales and the energetic large scales are:

$$\frac{\lambda_T}{l} \sim Re^{-1/2} \tag{2.7}$$

$$\frac{\lambda_T}{\eta} \sim Re^{1/4} \tag{2.8}$$

The distribution of the turbulent kinetic energy over these three scales can be observed by a spectral analysis. In the spectrum analysis we represent different length scales by their wave number (k) and represent the velocity field in Fourier space. By multiplying the velocity at a particular wave number with its complex conjugate we get the spectrum analysis presenting the distribution of kinetic energy across ranges of wave numbers.

Kolmogorov's 5/3 spectrum law states that the energy spectrum $E(\kappa)$ in the inertial range follows $E(\kappa) = C\epsilon^{2/3}\kappa^{-5/3}$ where $\epsilon$ is the energy dissipation rate, $\kappa$ is XXX and $C$ is the universal Kolmogorov constant. The typical energy spectrum of all three ranges are shown in Fig. 2.3.

## 2.2 Conservation Laws and Governing Equations

### 2.2.1 Navier-Stokes Equation

The governing equations for our simulation are the reactive compressible Navier-Stokes equations for an ideal reactive gas [51, 56], which describe the

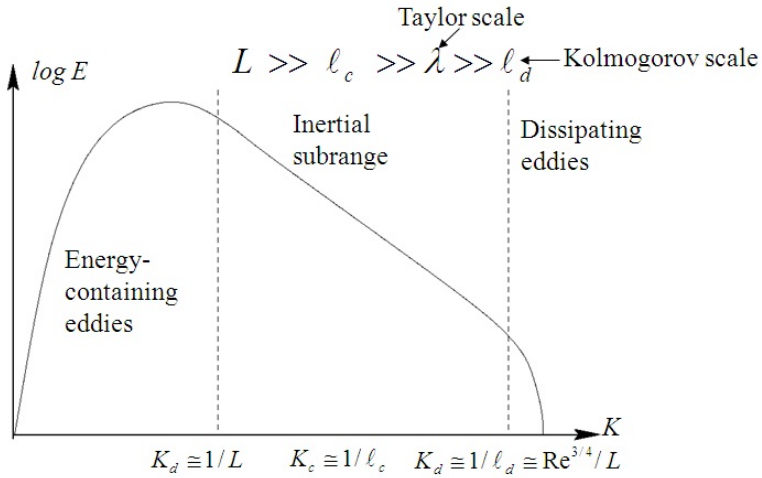


Figure 2.3: Schematic plot of a typical turbulent energy spectrum [47].

conservation of mass, momentum and energy:

$$\frac{\partial \rho}{\partial t} + \frac{\partial}{\partial x_j}\left(\rho u_j\right) = 0 \ , \tag{2.9}$$

$$\frac{\partial}{\partial t}\left(\rho u_i\right) + \frac{\partial}{\partial x_j}\left(\rho u_i u_j\right) + \frac{\partial p}{\partial x_i} = \frac{\partial \tau_{ij}}{\partial x_j} \ , \tag{2.10}$$

$$\frac{\partial E}{\partial t} + \frac{\partial\left[\,(E+p)\,u_j\right]}{\partial x_j} = \frac{\partial}{\partial x_j}\left(\tau_{ij} u_i\right) - \frac{\partial q_j}{\partial x_j} + H \ , \tag{2.11}$$

together with the balance equation for the mass fraction of each species in the mixture:

$$\frac{\partial}{\partial t}\left(\rho Y_i\right) + \frac{\partial}{\partial x_j}\left(\rho u_j Y_i\right) = \frac{\partial^2}{\partial x_j^2}\left(\rho d_i Y_i\right) + \dot{m}_i \ . \tag{2.12}$$

Here $\rho$ is the density, $u$ is the velocity, $E$ is the specific energy, $Y_i$ is the mass fraction of species $i$, and $\dot{m}_i$ is the production rate of species $i$. $H$ is the rate of heat release from the chemical reactions. The viscous stress tensor $\tau_{ij}$ derived

from Newtonian fluid reflects the proportionality between the shear stress and the rate of deformation:

$$\tau_{ij} = 2\mu S^*_{ij} = \mu \left[ \left( \frac{\partial u_i}{\partial x_j} + \frac{\partial u_j}{\partial x_i} \right) - \frac{2}{3}\delta_{ij} \frac{\partial u_k}{\partial x_k} \right] , \tag{2.13}$$

where $\mu$ is the dynamic viscosity coefficient and $\delta$ is the Kronecker delta. The heat flux $q_j$ is calculated by Fourier's law of conduction, an empirical-base derivation relates the heat transfer with temperature gradient,

$$q_j = -k \frac{\partial T}{\partial x_j} , \tag{2.14}$$

where $T$ is the temperature and $k$ is the thermal conductivity coefficient. Calculation of the production rates $\dot{m}_i$ and hear release rate $H$ will be introduced in Sec. 4.1.

### 2.2.2 Equations of State for Single Species and Mixture

The compressible Navier-Stokes equations (2.9-2.11) are open equations since the number of unknown variables ($\rho$, $\boldsymbol{u}$, $E$ and $P$) is larger than the number of equations. The equation of state (EOS) is needed to couple the pressure $P$ and the specific energy $E$ in order to close the Navier-Stokes equations. In other words, we require functions

$$P = P(E, \rho, \boldsymbol{u}) \qquad \text{and} \qquad E = E(P, \rho, \boldsymbol{u}) . \tag{2.15}$$

EOS are thermodynamic equations describing the state of matter under

a given set of physical conditions. The state of gas is commonly described by the state variables: pressure $P$, temperature $T$ and specific volume $V = 1/\rho$. Actually, experiments show that only two state variables are needed to define the state of pure gas in equilibrium or undergoing a steady or quasi-steady process. In other words, there exists a function $f(P, V, T) = 0$.

Specific internal energy $e$ is defined as the energy associated with the random, disordered motion of molecules. The e is a function of the state or state variables (since state is described by state variables):

$$e = e(V, T) \ . \tag{2.16}$$

Specific enthalpy H is defined as

$$H = e + PV \ . \tag{2.17}$$

Using the first law of thermal dynamics, it can be derived that the specific heat for a constant volume process is

$$C_v = \left(\frac{\partial e}{\partial T}\right)_V \ . \tag{2.18}$$

It can be derived that the specific heat for a constant pressure process is

$$C_p = \left(\frac{\partial H}{\partial T}\right)_P \ . \tag{2.19}$$

The $C_p$ and $C_v$ are thermodynamic properties and depend only on the state.

Besides the internal energy $e$ and the enthalpy $H$, another important thermodynamics concept is the entropy $S$ defined by the second law of thermodynamics. Combining the first and second law, we have the *fundamental thermodynamics identity*:

$$de = -PdV + TdS + \Sigma_i u_i dN_i \ . \tag{2.20}$$

Here last term $\Sigma_i u_i dN_i$ denotes the change of internal due to changing numbers of particles. $N_i$ is the number of particle $i$ and $u_i$ is the chemical potential of partical $i$.

Our model scramjet combustor simulation makes an assumption of *ideal-gas* EOS. The *ideal-gas* satisfies the law of Boyel and Gay-Lussac (law of ideal gas):

$$PV = \frac{RT}{M} \tag{2.21}$$

where R is the universal gas constant and M is the molecular weight of the gas. It can be derived, through the concept of entropy, that the internal energy of an ideal gas only depends on the temperature of the gas and is independent of the specific volume, i.e, $e = e(T)$. The enthalpy

$$H = e(T) + PV = e(T) + \frac{RT}{M} \tag{2.22}$$

of ideal-gas is also a function of the temperature only. It is easy to see $C_p$ and $C_v$ are both functions of T only. Since internal energy $e$ only depends on T,

we have

$$de = \left(\frac{\partial e}{\partial T}\right)_V dT + \left(\frac{\partial e}{\partial V}\right)_T dV = C_v(T)dT \tag{2.23}$$

since the second term $\frac{\partial e}{\partial V} = 0$. We can also have

$$dH = C_p(T)dT \tag{2.24}$$

Subtract Eq. (2.23) from Eq. (2.24) we get

$$dH - de = (C_p(T) - C_v(T))dT \tag{2.25}$$

Since $dH - de = d(H - e) = d(PV) = d(\frac{RT}{M})$, we can further derive

$$C_p(T) - C_v(T) = \frac{R}{M} \ . \tag{2.26}$$

The ratio of specific heats is denoted by $\gamma$:

$$\gamma = \frac{C_p}{C_v} \tag{2.27}$$

The specific heat $C_p(T)$ of all ideal-gas is approximated by fourth order polynomials with the coefficients calculated through a least square fit by NASA [43]

$$\frac{Cp}{R} = a_1 + a_2T + a_3T^2 + a_4T^3 + a_5T^4 \tag{2.28}$$

$H(T)$ follows the integral form of equation (2.28)

$$\frac{H}{RT} = a_1 + \frac{a_2}{2}T + \frac{a_3}{3}T^2 + \frac{a_4}{4}T^3 + \frac{a_5}{5}T^4 + \frac{a_6}{T} \tag{2.29}$$

Here $a_1$, $a_2$, $a_3$, $a_4$, $a_5$, $a_6$ and $a_7$ are the numerical coefficients tabulated in NASA thermodynamic table [43]. The pressure $P$ and the internal energy $E$ of a ideal gas can be coupled by equation:

$$e = H(T) + PV = \left( a_1 + \frac{a_2}{2}T + \frac{a_3}{3}T^2 + \frac{a_4}{4}T^3 + \frac{a_5}{5}T^4 + \frac{a_6}{T} + \frac{1}{M} \right) RT \tag{2.30}$$

1. when we know $P$ and $V$, we first calculated the temperature as $T = PVM/R$, then use the temperature to calculate $e$.

2. when we know $e$ and $V$, we solve the non-linear equation of $e = H(T) + \frac{RT}{M}$ for the temperature of $T$, then $P$ is calculated by $P = RT/(MV)$.

The specific energy $E$ is related to the specific internal energy e by $E = e + \rho(u^2 + v^2 + w^2)/2$.

The mixture of ideal gas is also an ideal gas. The above equations can be used with some modifications. To adapt the EOS of pure species to a mixture, the molecular weight $M$ is replaced by the average $M$ for mixture of $n$ species:

$$M = \sum_{i=1}^{n} Y_i M_i \tag{2.31}$$

The specific heat $C_p$ and enthalpy $H$ of mixture can be calculated empirically by:

$$C_p = \sum_{i=1}^{n} Y_i C_{p_i} \ , \tag{2.32}$$

and

$$H = \sum_{i=1}^{n} Y_i H_i \ . \tag{2.33}$$

### 2.2.3 Transport Properties

The transport properties included in the our model scramjet combustor are viscosity, thermal conductivity, and mutual diffusivity. The dynamic viscosity and thermal conductivity are calculated by semi-empirical mixture rules [10]:

$$\mu = \sum_{i=1}^{n} \frac{\mu_i}{1 + \frac{M_i}{Y_i} \sum_{j=1, j\neq i}^{j=n} \frac{Y_j G_{ij}}{M_j}} \ , \tag{2.34}$$

$$k = \sum_{i=1}^{n} \frac{k_i}{1 + \frac{M_i}{Y_i} \sum_{j=1, j\neq i}^{j=n} \frac{Y_j G_{ij}}{M_j}} \ , \tag{2.35}$$

where dimensionless quantity $G_{ij}$ are

$$G_{ij} = \frac{1}{\sqrt{8}} \left(1 + \frac{M_i}{M_j}\right)^{-1/2} \left[1 + \left(\frac{\mu_i}{\mu_j}\right)^{-1/2} \left(\frac{M_j}{M_i}\right)^{1/4}\right]^2 \ . \tag{2.36}$$

The dynamic viscosity and thermal conductivity of a single gas species are computed by the elementary gas model:

$$\mu_i = 2.6693 \cdot 10^{-5} \frac{\sqrt{M_i T}}{\delta_i^2 \Omega_{ij}^{(2,2)}} \ . \tag{2.37}$$

$$k_i = \mu_i \left(c_{p,i} + \frac{5}{4} \frac{R}{M_i}\right) \ . \tag{2.38}$$

Here $M_i$ is the molecular mass of species $i$. $\delta_i$ is a characteristic diameter of the molecule $i$, which is often called the collision diameter. The dimensionless quantity $\Omega_{ij}$ is called the "collision integral for viscosity" which accounts for the paths molecules take during a binary collision. $C_p$ is the heat capacity, the

calculation of which has been introduced in Sec. 2.2.2.

The calculation of the binary diffusion coefficient of mixture is complex and is omitted here. Details of the binary diffusion coefficient calculation can be found in [15].

## 2.3 Turbulent Modeling Approaches

There are three main methodologies for turbulent flow simulation: Reynolds-averaged Navier-Stokes (RANS), large eddy simulation (LES) and direct numerical simulation (DNS). All these three methodologies solve the governing Navier-Stokes equations. However they have a different way of predicting the fluid dynamics.

In Sec. 2.1, we describe three different length scales of turbulence. DNS is the simulation methodology which resolves the turbulent scale down to the Kolmogorov scales. RANS only resolves the large and energetic scales. LES lies midway between DNS and RANS. The grid resolutions of these three kinds of turbulence simulation approaches are illustrated in Figure 2.4. We introduce these methodologies and discuss their advantages and disadvantages.

### 2.3.1 DNS

DNS solves the Navier-Stokes equations directly without any turbulence modeling. In DNS, the whole range of spatial and temporal scales of turbulence, from the large integral scale $l_c$ down to the small Kolmogorov scale $\eta_k$, are resolved directly.

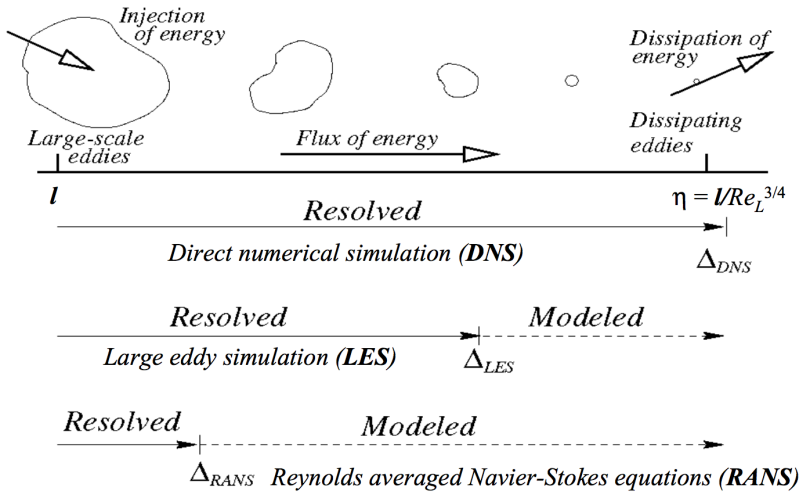


Figure 2.4: Grid resolution of DNS, LES and RANS [47]

DNS is computationally expensive. We know from Sec. 2.1 that $\frac{\eta_k}{l} \sim Re^{-3/4}$. Since DNS needs to resolve both the large integral scale and the small Kolmogorov scale, the number of grids needed to resolve the small scales in each dimension is $\sim Re^{3/4}$. Thus the total number of grids in three dimensional simulation is $\sim Re^{9/4}$. Assuming the time resolution is proportional to space resolution, the overall cost is about $Re^3$.

This huge computational cost prevents the use of DNS for a wide variety of flows, especially at large Reynolds number. For a three dimensional flow with $Re \approx 5000$, the grid points needed will be 250 million cells. Thus the application of DNS is restricted to flows with low Reynolds number.

Although DNS is expensive, the accuracy of the DNS result can be comparable with the experiment. In circumstances when the experiment data are unavailable, the DNS data is often used for validation and verification purpose.

In conclusion, DNS works as a powerful research tool for turbulent flows at low to moderate Reynolds numbers.

### 2.3.2 RANS

The RANS solves the time-averaged Navier-Stokes equations. In RANS, the fluid dynamics are decomposed into two parts: the time averaged part and the fluctuation part. There are two kinds of decomposition: the Reynolds averaging decomposition and the Favre averaging decomposition. In the Reynolds averaging decomposition, an instantaneous solution variable $\phi$ is decomposed into time averaging part $\bar{\phi}$ and fluctuation part $\phi'$:

$$\phi = \bar{\phi} + \phi' \tag{2.39}$$

In the Favre averaging decomposition, an instantaneous solution variable $\phi$ is decomposed into mass weighted time averaging part $\widetilde{\phi}$ and fluctuation part $\phi''$:

$$\phi = \widetilde{\phi} + \phi'' \tag{2.40}$$

where

$$\widetilde{\phi} \equiv \frac{\overline{\rho\phi}}{\bar{\rho}} \tag{2.41}$$

In derivation of governing RANS equations, Reynolds averaging is applied to density $\rho$, pressure $p$, shear stress $\tau$ and heat flux $q$; while Favre averaging is applied to the velocity field $u$, specific internal energy $e$ , and specific enthalpy $h$. The Governing Favre-Averaged Navier-Stokes Equation for compressible

flow are:

1. continuity equation

$$\frac{\partial \bar{\rho}}{\partial t} + \frac{\partial}{\partial x_i}\left(\bar{\rho}\widetilde{u}_i\right) = 0 \ , \tag{2.42}$$

2. momentum equation

$$\frac{\partial}{\partial t}\left(\bar{\rho}\widetilde{u}_i\right) + \frac{\partial}{\partial x_j}\left(\bar{\rho}\widetilde{u}_i\widetilde{u}_j\right) + \frac{\partial \bar{p}}{\partial x_j} = \frac{\partial}{\partial x_j}\left(\bar{\tau}_{ij} - \overline{\rho u_i^{''} u_j^{''}}\right) \ , \tag{2.43}$$

3. energy equation

$$\begin{aligned}
&\frac{\partial}{\partial t}\left[\bar{\rho}\left(\widetilde{e} + \frac{1}{2}\widetilde{u}_i\widetilde{u}_i\right) + \frac{1}{2}\overline{\rho u_i^{''} u_i^{''}}\right] + \frac{\partial}{\partial x_j}\left[\bar{\rho}\left(\widetilde{h} + \frac{1}{2}\widetilde{u}_i\widetilde{u}_i\right) + \frac{\widetilde{u}_j}{2}\overline{\rho u_i^{''} u_i^{''}}\right] \\
&\qquad = \frac{\partial}{\partial x_j}\left[\left(\bar{\tau}_{ij} - \overline{\rho u_i^{''} u_j^{''}}\right)\widetilde{u}_i - \bar{q}_j\right] \\
&\qquad + \frac{\partial}{\partial x_j}\left[-\overline{\rho u_j^{''} h^{''}} - \overline{\rho u_j^{''} u_i^{''} u_i^{''}} + \overline{\rho u_i^{''} \tau_{ij}}\right] \ .
\end{aligned} \tag{2.44}$$

Here we have four unknown terms,

1. $\overline{\rho u_i^{''} u_j^{''}}$, Favre-averaged reynolds stress tensor,
2. $\overline{\rho u_j^{''} h^{''}}$, turbulent transport of heat,
3. $\overline{\rho u_j^{''} u_i^{''} u_i^{''}}$, turbulent transport of kinetic energy,
4. $\overline{\rho u_i^{''} \tau_{ij}}$, turbulent molecular diffusion.

These terms reflect the effect of turbulence on the mean flow.

To close the mean flow equations, a turbulence model is needed to calculate these terms. These turbulence models are often based on the Boussinesq

hypothesis that the Reynolds stress could be linked to the mean rate of deformation:

$$\tau_{ij} = -\overline{\rho u_i'' u_j''} = \mu_t \left( \frac{\partial U_i}{\partial x_j} + \frac{\partial U_j}{\partial x_i} \right) \tag{2.45}$$

where $\mu_t$ is the turbulent viscosity.

There are many flavors of RANS turbulence model. To name a few, there are zero equation model, the mixing length model; the one equation models, like the Spalart-Almaras model; the two equation models, the $k - \epsilon$ style models and the $k - \omega$ model for example; the seven equation model, namely, the Reynolds stress model. The number of equations represent the number of additional PDEs that need to be resolved. More details of these RANS model can be found in [47].

Compared with DNS, RANS can obtain an averaged solution on a much coarser grid. Thus RANS is very economical by computational resource and time. For many applications, the averaged solution or the steady state solution is preferable. Thus RANS is a widely used approach for engineering problems.

However, RANS could not predict the transient behaviour of fluctuating flow field. In problems like turbulent mixing and combustion where the chemical reactions are driven by the unsteady turbulent mixing of the fuel and the oxidizer, RANS might lose its accuracy.

### 2.3.3 LES

In LES, the larger turbulent motions are resolved, while the effects of smaller scale motions are modeled. LES lies in the midway between DNS

and LES in terms of computational expense and simulation accuracy. LES is motivated by the shortcomings of DNS and RANS. Compared with RANS, LES is more accurate because it resolves the large scale unsteady motions down to the inertial range. Compared with DNS, LES is more economic in computational cost because DNS spends most of the computational resource in resolving the small dissipative motions while LES models the effect of these motions.

The governing equations of LES are the space filtered Navier-Stokes equation. The motions and eddies with scale smaller than the filter width are removed by the filtering. The larger and important eddies remain and are governed by the resulting equations.

A space filter $G$ decomposes a variable $\phi(x)$ into the sum of a filtered component $\bar{\phi}$ and a residual component $\phi^{'}$. The filtered conponent is defined by

$$\bar{\phi} = \int \phi(x^{'})G(x, x^{'})dx^{'} \tag{2.46}$$

For compressible flow, the *Favre filtering* is defined in the similar way as the *Favre Averaging* in Sec. 2.3.2:

$$\widetilde{\phi} = \frac{\int \rho(x^{'})\phi(x^{'})G(x, x^{'})dx^{'}}{\int \rho(x^{'})G(x, x^{'})dx^{'}} \tag{2.47}$$

The Favre filtered Navier-Stokes equations for compressible flow are [40]:

1. Filtered continuity equation

$$\frac{\partial \bar{\rho}}{\partial t} + \frac{\partial \bar{\rho}\widetilde{u}_i}{\partial x_j} = 0 \ ,$$

2. Filtered momentum equation

$$\frac{\partial \bar{\rho}\widetilde{u}_i}{\partial t} + \frac{\partial \bar{\rho}\widetilde{u}_i\widetilde{u}_j}{\partial x_j} + \frac{\partial \bar{P}}{\partial x_j} = \frac{\partial}{\partial x_j}\left(\bar{\tau}_{ij} - \overline{T}_{ij}\right) \ ,$$

3. Filtered energy equation

$$\frac{\partial \bar{E}}{\partial t} + \frac{\partial (\bar{E}+\bar{P})\widetilde{u}_j}{\partial x_j} = \frac{\partial \bar{\tau}_{ij}\widetilde{u}_j}{\partial x_j} + \frac{\partial}{\partial x_j}\left(\bar{\kappa}\frac{\partial \widetilde{T}}{\partial x_j}\right) + \frac{\partial}{\partial x_j}\left(\sum \widetilde{H}_k \bar{\rho}\widetilde{D}\frac{\partial \widetilde{\psi}}{\partial x_j}\right) - \frac{\partial q_i^H}{\partial x_i} + \overline{S_e} \ ,$$

4. Filtered concentration equation

$$\frac{\partial \bar{\rho}\widetilde{\psi}_k}{\partial t} + \frac{\partial \bar{\rho}\widetilde{\psi}_k\widetilde{u}_j}{\partial x_j} = \frac{\partial}{\partial x_j}\left(\bar{\rho}\widetilde{D}\frac{\partial \widetilde{\psi}_k}{\partial x_j}\right) - \frac{\partial q_{k,j}^{(\psi)}}{\partial x_j} + \overline{S}_{\psi,k} \ .$$

The subgrid scaled (SGS) terms $\tau_{ij}$, $q_i^{(H)}$, and $q_i^{(\psi)}$ are expressed as

$$\tau_{ij} = \rho\left(\widetilde{u_i u_j} - \widetilde{u}_i\widetilde{u}_j\right) \ , \tag{2.48}$$

$$q_i^{(H)} = \bar{\rho}\left(\widetilde{c_p T u_i} - \widetilde{c}_p\widetilde{T}\widetilde{u}_i\right) \ , \tag{2.49}$$

$$q_{k,i}^{(\psi)} = \bar{\rho}\left(\widetilde{\psi_k u_i} - \widetilde{\psi}_k\widetilde{u}_i\right) \ . \tag{2.50}$$

Here the filtered variable $\bar{\rho}$, $\widetilde{\psi}$, $\widetilde{u}_i$ , $\bar{p}$ and $\bar{E}$ denotes, respectively, the filtered density, species mass fraction, velocity, pressure, and total specific

energy $\bar{E} = \bar{\rho}\widetilde{e} + \bar{\widetilde{u}}_k^2/2 + \tau_{kk}/2$. $\widetilde{H}_k$ is the species enthalpy of species $k$:

$$\widetilde{H}_k = \widetilde{e}_k + \frac{\bar{p}}{\bar{\rho}} \tag{2.51}$$

where $\widetilde{e}_k$ is the filtered specific internal energy of each species. we assume $q_i^{(T)} = 0$ [26]. The viscous stress tensor $\bar{\tau}_{ij}$ is

$$\bar{\tau}_{ij} = \bar{\mu}\left(\left(\frac{\partial \widetilde{u}_i}{\partial x_j} + \frac{\partial \widetilde{u}_j}{\partial x_i}\right) - \frac{2}{3}\frac{\partial \widetilde{u}_k}{\partial x_k}\delta_{ij}\right) \tag{2.52}$$

where $\mu = \overline{\nu\rho}$ is the filtered dynamic viscosity.

There are several SGS models to close the space filtered Navier-Stokes equation. We discuss the Classical Smagorinsky model [62] and the dynamic Smagorinsky model [24] in detail in this section.

### Classical Smagorinsky Model

The Smagorinsky model assumes a the local equilibrium of the subgrid scales. The Smagorinsky model for eddy-viscosity is combined with the Yoshizawa model for SGS turbulent kinetic energy. For compressible flow, the subgrid terms in species concentration and energy equation also use the gradient-transport models.

The SGS stress $T_{ij}$ is decomposed into anisotropic and isotropic tensors and each tensor is modeled separately:

$$T_{ij} = (T_{ij} - T_{kk}\frac{\delta_{ij}}{3}) + T_{kk}\frac{\delta_{ij}}{3} \tag{2.53}$$

with

$$\text{an-isotropic tensor} \quad T_{ij}^a = T_{ij} - T_{kk}\frac{\delta_{ij}}{3} \tag{2.54}$$

and

$$\text{isotropic tensor} \quad T_{ij}^i = T_{kk}\frac{\delta_{ij}}{3} \tag{2.55}$$

The anisotropic part is modelled based on the concept of turbulent viscosity

$$T_{ij}^a = -2\bar{\rho}\nu_t\widetilde{S}_{ij}^a \tag{2.56}$$

where $\widetilde{S}_{ij} = \frac{1}{2}\left(\frac{\partial\widetilde{u}_i}{\partial x_j} + \frac{\partial\widetilde{u}_j}{\partial x_i}\right), S_{ij}^a = \widetilde{S}_{ij} - \frac{\delta_{ij}}{3}\widetilde{S}_{kk}$, By the classical Smagorinsky model, the simple algebraic model holds for $\nu_t$:

$$\nu_t = (C_s\bar{\Delta})^2|\bar{S}| \tag{2.57}$$

with $\bar{\Delta} = (\Delta x\Delta y\Delta z)^{1/3}$ and $\bar{S} \equiv \sqrt[2]{2S_{ij}S_{ij}}$. $C_s$ is a constant with value between 0.065-0.25. Thus for the anisotropic part we have

$$T_{ij}^a = -2\bar{\rho}(C_s\bar{\Delta})^2|\bar{S}|S_{ij}^a \tag{2.58}$$

The isotropic part of SGS stress based on Yoshizawa model [74] with the argument that $k_{SGS} = (C_I\Delta)^2|\widetilde{S}|^2$,

$$T_{kk} = -2\bar{\rho}(C_I\bar{\Delta})^2|\bar{S}|^2 \tag{2.59}$$

$C_s$ is a model constant. The full SGS terms can be expressed as:

$$T_{ij} = -2\bar{\rho}(C_s\bar{\Delta})^2|\bar{S}|S^a_{ij} + \frac{\delta_{ij}}{3}2\bar{\rho}(C_I\bar{\Delta})^2|\bar{S}|^2 \tag{2.60}$$

A gradient-transport assumption is used for the SGS mass species transport,

$$\lambda_{kj} = -\bar{\rho}\frac{\nu_t}{Sc_t}\frac{\partial\widetilde{Y}_k}{\partial x_j} \tag{2.61}$$

where $Sc_t$ is the turbulent Schmidt number. The SGS heat transport can be derived with similar assumption,

$$Q_j = -\frac{\widetilde{c_p\nu_t}}{Pr_t}\frac{\partial\widetilde{T}}{\partial x_j} = -k_t\frac{\partial\widetilde{T}}{\partial x_j} \tag{2.62}$$

where $Pr_t$ is the turbulent Prandtl number.

Once the four coefficients $C_S$, $C_I$, $Pr_t$ and $Sc_t$ are specified, the filtered Navier-Stokes equation for compressible flow is closed. According to Germano et al. [24], there are several limitations of the classical Smagorinsky model. First, the model constant $C_S$, $C_I$, $Pr_t$ and $Sc_t$ should be changed to adapt to different flows. Second, the model does not have a correct limiting behaviour neat walls. Third, the model always assumes a positive eddy viscosity, even for laminar flows.

To overcome these limitations, a Dynamic Smagorinsky Model (DSM) is introduced by Germano [24].

**Dynamic Smagorinsky Model**

The Dynamic Smagorinsky model calculates the model coefficients $C_S$, $C_I$, $Pr_t$ and $Sc_t$ dynamically. In DSM, a dynamic procedure is introduced base on the Smagorinsky model applied at two different filter levels. The SGS stress at grid level $\bar{\Delta}$ is

$$T_{ij} = -2\bar{\rho}(C_s\bar{\Delta})^2|\widetilde{S}|\widetilde{S}^a_{ij} + \frac{\delta_{ij}}{3}2\bar{\rho}(C_I\bar{\Delta})^2|\widetilde{S}|^2 \tag{2.63}$$

A test filter is introduced with a filter width $\widehat{\bar{\Delta}}$ larger than the grid filter. The SGS stress at the test filter level $\widehat{\bar{\Delta}}$ is by defination:

$$t_{ij} = \widehat{\overline{\rho u_i u_j}} - \frac{\widehat{\overline{\rho u_i}}\widehat{\rho u_i}}{\widehat{\bar{\rho}}} \tag{2.64}$$

At the same time the SGS stress at the test filter level can be modeled by:

$$T_{ij} = -2\widehat{\bar{\rho}}(C_s\widehat{\bar{\Delta}})^2|\widehat{\widetilde{S}}|\widehat{\widetilde{S}}^a_{ij} + \frac{\delta_{ij}}{3}2\widehat{\bar{\rho}}(C_I\widehat{\bar{\Delta}})^2|\widehat{\widetilde{S}}|^2 \ . \tag{2.65}$$

By applying Germano's identity, we have

$$L_{ij} = t_{ij} - \widehat{T}_{ij} = \left(\frac{\widehat{\overline{\rho u_i \rho u_i}}}{\bar{\rho}}\right) - \frac{\widehat{\overline{\rho u_i}}\widehat{\rho u_i}}{\widehat{\bar{\rho}}} \tag{2.66}$$

where $L_{ij}$ is the Leonard stress tensor. The anisotropic part of $L_{ij}$ is

$$L^1_{ij} = t^a_{ij} - \widehat{T}^a_{ij} = 2(C_s\bar{\Delta})^2\widehat{\bar{\rho}|\widetilde{S}|\widetilde{S}^a_{ij}} - 2(C_s\widehat{\bar{\Delta}})^2\widehat{\bar{\rho}}|\widehat{\widetilde{S}}|\widehat{\widetilde{S}}^a_{ij} = C_s^2 M^a_{ij} \tag{2.67}$$

where

$$M_{ij}^a = \left[ \widehat{\bar{\rho}|\widetilde{S}|\widetilde{S}_{ij}^a} - 2\left(\frac{\widehat{\bar{\Delta}}}{\bar{\Delta}}\right)^2 \widehat{\bar{\rho}}|\widehat{\widetilde{S}}|\widehat{\widetilde{S}}_{ij}^a \right] \bar{\Delta}^2 \tag{2.68}$$

Eq. (2.67) includes 5 independent equations but only has one unknown variables $C_s$. Lily [39] proposed a least-squared approach to solve for $C_s$:

$$C_s^2 = \frac{\langle L_{ij}^2 M_{ij}^2 \rangle}{\langle M_{ij}^2 M_{ij}^2 \rangle} \ , \tag{2.69}$$

where $\langle . \rangle$ operator denotes the average over equation number. If the value of $C_s^2$ is negative, its value will be clipped to zero.

Actually, the value of $C_s^2$ calculated from this equation is quite unstable with space and time. The value of $C_s^2$ may be zero in large fraction of the flow field after clipping. To remove the large fluctuations and the zero values of $C_s^2$, different averaging approaches are proposed. Usually the numerator and denominator are averaged over homogeneous flow directions. Meneveau [46] proposed an averaging method based on the fluid imaginary particle trajectory. Some authors used a time averaging of $C_s^2$ which might introduce errors before the flow becomes statistical stationary. In the absence of a homogeneous flow direction, local averaging may be used. In our model scramjet comustor simulation, the local averaging method is applied. the $C_s^2$ is clipped to be zero.

The model coefficient $C_I$ is computed as

$$C_I^2 = \frac{\langle L_{kk}^i \rangle}{\langle M_{kk}^i \rangle} \tag{2.70}$$

where

$$M_{kk}^{i} = \left[ -\overline{\widehat{\rho\left(\widetilde{2}S_{ij}\widetilde{S}_{ij}\right)}} + 2\left(\frac{\widehat{\bar{\Delta}}}{\bar{\Delta}}\right)^{2} \widehat{\bar{\rho}}\left(2\widehat{\widetilde{S}}_{ij}\widehat{\widetilde{S}}_{ij}\right)\right] \bar{\Delta}^{2} \tag{2.71}$$

Applying similar procedures to the SGS mass species transport and the SGS heat transport, we can have $Pr_t$ and $Sc_t$ calculated as:

$$Pr_t = C_s \frac{\langle (\sum M_i^{P(H)} M_i^{(H)})^{+} \rangle}{\langle (\sum L_i^{(H)} M_i^{(H)})^{+} \rangle} \tag{2.72}$$

where

$$L_i^{(H)} = \widehat{\bar{\rho}\widetilde{c}_p\widetilde{T}\widetilde{u}_i} - \frac{\widehat{\bar{\rho}\widetilde{c}_p}\widehat{\bar{\rho}\widetilde{T}}\widehat{\bar{\rho}\widetilde{u}_i}}{\widehat{\bar{\rho}}} \ , \tag{2.73}$$

$$M_i^{(H)} = \Delta^2 \left(\bar{\rho}\widetilde{c}_p|\widetilde{S}|\frac{\partial \widehat{T}}{\partial x_i}\right) - \widehat{\Delta}^2\widehat{\bar{\rho}\widetilde{c}_p}|\widehat{\widetilde{S}}|\frac{\partial \widehat{\widetilde{T}}}{\partial x_i} \ , \tag{2.74}$$

and

$$Sc_t = C_s \frac{\langle (\sum M_i^{(\psi)} M_i^{(\psi)})^{+} \rangle}{\langle (\sum L_i^{(\psi)} M_i^{(\psi)})^{+} \rangle} \tag{2.75}$$

where

$$L_i^{\psi} = \widehat{\bar{\rho}\widetilde{u}_i\widetilde{\psi}} - \frac{\widehat{\bar{\rho}\widetilde{u}_i}\widehat{\bar{\rho}\widetilde{\psi}}}{\widehat{\bar{\rho}}} \ , \tag{2.76}$$

$$M_i^{\psi} = \Delta^2\widehat{\bar{\rho}|\widetilde{S}|\frac{\partial\widetilde{\psi}}{\partial x_i}} - \widehat{\Delta}^2\widehat{\bar{\rho}}|\widehat{\widetilde{S}}|\frac{\partial\widehat{\widetilde{\psi}}}{\partial x_i} \ . \tag{2.77}$$

## 2.4 Numerical Scheme

In our model scramjet combustor simulation, a conservative finite difference approach is used as the numerical discretization scheme. Since the

governing equations in our project are the conservative of mass, momentum, energy and weight of species, the conservative methods (include the conservative finite difference methods and the finite volume methods) are more suitable than the conventional finite difference methods. The conservative methods are also better for the shock-capturing problems: they can estimate the shock speed correctly and satisfy the the Rankine-Hugoniot relation across discontinuities.

In conservative finite difference methods, the governing equations can be solved dimension by dimension. Thus the conservative finite difference methods are better than the finite volume methods, which could be computationally expensive for multi-dimensional problems with high order accuracy. For each dimension, we have the equation

$$\frac{\partial U}{\partial t} + \frac{\partial F}{\partial x} = 0 \tag{2.78}$$

where $F$ is a function of $U$. The discretization is simple:

$$\frac{\partial \widehat{U}_i}{\partial t} + \frac{F_{i+\frac{1}{2}} - F_{i-\frac{1}{2}}}{\Delta x} = 0 \tag{2.79}$$

where $\widehat{U}_i$ is the cell-averaged conservative variable of cell $i$, $F_{i\pm\frac{1}{2}}$ is the flux at location $i \pm \frac{1}{2}$ (cell faces of cell $i$). The value of $F_{i\pm\frac{1}{2}}$ can be approximate $F_i$'s in cell centers of local stencil using reconstruction or interpolation.

In our model scramjet combustor simulation, a 5th order finite differ-

ence Weighted Essentially Non-Oscillatory (WENO) scheme of Jiang and Shu [31] is used as our conservative finite difference scheme. WENO schemes use the idea of adaptive stencils to automatically adjust the stencil weight. It can achieve high order accuracy and non-oscillatory property near discontinuities [31]. WENO schemes have been widely used to solve compressible Navier-Stokes equations, together with high-order Runge-Kutta methods.

The WENO scheme is constructed based on Essentially Non-Oscillatory (ENO) scheme. Harten [25] constructed the first ENO scheme in 1987. The first WENO scheme is a third order finite volume scheme by Liu, Osher and Chan [41]. The fifth order finite difference WENO scheme applied in our problem is constructed by Jiang and Shu [31] in 1996.

The reason we prefer the finite difference WENO over the finite volume WENO is that the finite difference WENO is more economic and FronTier has structured grid. Although the finite volume WENO scheme can allow for non-smooth and non-structured scheme, the finite volume WENO scheme are several times expensive than the finite difference WENO scheme at the same order of accuracy.

The ENO scheme applies uniform high order polynomial reconstruction of $F_{i\pm\frac{1}{2}}$ on local stencils. There are several candidate stencils available for this kind of polynomial reconstruction. ENO chooses the smoothest stencil and use that stencil to reconstruct flux $F_{i+\frac{1}{2}}$. Near discontinuity, ENO choose the stencil on the continuous side. Thus the ENO scheme is locally adaptive.

Different from ENO, WENO makes use of all available stencil. Different weights are assigned to different stencils based on the smoothness of each stencil. In smooth region, it assigns similar weights to all stencils and could achieve a higher order of accuracy than ENO. Near discontinuity, WENO assigns small weight to the discontinues stencils and large weight to continuos stencil. In this way, the WENO scheme is also locally adaptive.

There are several steps in of WENO reconstruction [61]. Take Eq. (2.78) as example.

(a) we need to split $F(u)$ into two monotone parts:

$$f(u) = f^+(u) + f^-(u) \tag{2.80}$$

to ensure $df^+(u)/du \geq 0$ and $df^-(u)/du \leq 0$. The Lax-Friedrichs splitting is commonly used:

$$f^{\pm}(u) = \frac{1}{2}(f(u) \pm \alpha u) \tag{2.81}$$

where

$$\alpha = max_u|f^{'}(u)| \tag{2.82}$$

In the following steps, reconstruction of $df^+(u)/du \geq 0$ and $df^-(u)/du \leq 0$ are conducted separately.

(b) The approximation of $F_i$ from each sub-stencils needs to be computed. Here we have three stencils and each stencil has three points.

The approximations are:

$$f^{(0)}_{i+1/2} = \frac{1}{3}\bar{f}_{i-2} - \frac{7}{6}\bar{f}_{i-1} + \frac{11}{6}\bar{f}_i \tag{2.83}$$

$$f^{(1)}_{i+1/2} = -\frac{1}{6}\bar{f}_{i-1} + \frac{5}{6}\bar{f}_i + \frac{1}{3}\bar{f}_{i+1} \tag{2.84}$$

$$f^{(2)}_{i+1/2} = \frac{1}{3}\bar{f}_i + \frac{5}{6}\bar{f}_{i+1} - \bar{f}_{i+2} \tag{2.85}$$

(c) The weights $\gamma_0$, $\gamma_1$, $\gamma_2$ need to be found to make the combination

$$f_{i+1/2} = \gamma_0 f^{(0)}_{i+1/2} + \gamma_1 f^{(1)}_{i+1/2} + \gamma_2 f^{(2)}_{i+1/2} \tag{2.86}$$

to have fifth order accuracy. The value of $\gamma$'s is $\gamma_0 = \frac{1}{10}$, $\gamma_1 = \frac{3}{5}$, $\gamma_2 = \frac{3}{10}$

(d) Find the nonlinear weights $\omega_0$, $\omega_1$, $\omega_2$ to make

$$u_{i+1/2} = \omega_0 f^{(0)}_{i+1/2} + \omega_1 f^{(1)}_{i+1/2} + \omega_2 f^{(2)}_{i+1/2} \tag{2.87}$$

fifth order in smooth regions and non-oscillatory at shocks. The $\omega$'s can be calculated by

$$\omega_k = \frac{\alpha_k}{\alpha_1 + \alpha_1 + \alpha_2} \tag{2.88}$$

where

$$\alpha_k = \frac{\gamma_k}{(\epsilon + IS_k)^p} \tag{2.89}$$

Here $\epsilon$ is introduced here to prevent zero denominator. Its value is

set to be $\epsilon = 10^{-6}$.

The $IS$'s are calculated by taylor expansion analysis:

$$IS_0 = \frac{13}{12}(f_{-2} - 2f_{-1} + f_0)^2 + \frac{1}{4}(f_{-2} - 4f_{-1} + 3f_0)^2 \tag{2.90}$$

$$IS_1 = \frac{13}{12}(f_{-1} - 2f_0 + f_1)^2 + \frac{1}{4}(f_{-1} - f_1)^2 \tag{2.91}$$

$$IS_2 = \frac{13}{12}(f_0 - 2f_1 + f_2)^2 + \frac{1}{4}(3f_0 - 4f_1 + f_2)^2 \tag{2.92}$$

The time discretization of WENO schemes is realized by third-order TVD Runge-Kutta method:

$$u^{(1)} = u^n + \Delta t L(u^n) \tag{2.93}$$

$$u^{(2)} = \frac{3}{4}u^n + \frac{1}{4}u^{(1)} + \frac{1}{4}\Delta t L(u^{(1)}) \tag{2.94}$$

$$u^{n+1} = \frac{1}{3}u^n + \frac{2}{3}u^{(2)} + \frac{2}{3}\Delta t L(u^{(2)}) \tag{2.95}$$

Thus we have 3rd-order in time and 5th-order in space finite difference WENO scheme.

In implementation of the WENO scheme into the compressible hyperbolic solver, we apply eigenvalue decomposition to the hyperbolic part of Navier-Stokes Equation and apply WENO scheme to decomposed equations on eigenvector space.

The draw back of WENO is that it can lead to numerical damping of turbulence, since these fluctuations can be seen as shock-like oscillations by

the scheme. In many scramjet simulation, authors use separate schemes for shock-capturing and the non-shock part. ENO or WENO is used near the shock while other schemes are used at other place. For example, in the LES simulation of hyshot-II[38], Larsson uses unstructured essentially non-oscillatory (ENO) second-order to accurate capture shock and a HLLC approximate Riemann solver in continous region.

## 2.5 Turbulent Inflow Generation

When LES and DNS approach are used for turbulence simulation and the turbulence in the flow field is mainly resolved, accurate prescription of inflow turbulence is required. There are many effective methods to generate inflow turbulence. These methods fall into two categories: synthetic turbulence techniques and rescaling-reintroducing method. The synthetic turbulence techniques generate a random field using models and this is added to a mean flow profile. The rescaling-reintroducing method takes the flow field at a downstream station, rescales it and impose it as inflow condition. We will introduce rescaling-reintroducing method in Sec. 3.5.2.

The random-noise method is a widely used synthetic turbulence techniques. However, the turbulence generated by the random-noise method lacks energy in the low wavenumber range. As the result, the pseudo turbulence would damp to zero quickly.

Another popular synthetic turbulence technique is the digital filtering

approach by Klein [33]. which is later improved by Xie [71] and Touber [65]. The digital filtering method of Klein [33] assumes that the second order correlation of homogenuous turbulence has a Gaussian form while Xie [71] and Touber [65] assume it has a exponential form. The method use here follow Touber's procedure.

To enforce the inflow turbulence to have a second order correlation of exponential form, the digital filtering method applies the discrete filter operator $F_N$

$$v_k = F_N(r_k) = \sum_{j=-N}^{N} b_j r_{k+j} \tag{2.96}$$

where the filter coefficient

$$b_j \approx \frac{\widetilde{b}_j}{\left(\sum_{k=-N}^{N} \widetilde{b}_k^2\right)} \tag{2.97}$$

and

$$\widetilde{b}_k = \exp\left(-\frac{\pi k}{n}\right) \tag{2.98}$$

The new set of variables $v$ has zero-mean and two-points correlation of:

$$\frac{\overline{v_k v_{k+m}}}{\overline{v_k v_k}} = \exp\left(-\frac{\pi m}{2n}\right) \tag{2.99}$$

Assume $v_k$ is assigned to one dimensional flow field with grid size of $\Delta x$ and integral length scale of $I_x$. We set n to be $I_x/\Delta x$ and $N$ to be $2n$.

Then the correlation function $R(x_k + x)$ of one dimensional flow field is:

$$R(x_k + x) = R(x_k + m\Delta x) = \frac{\overline{v_k v_{k+m}}}{\overline{v_k v_k}} = \exp\left(-\frac{\pi m}{2n}\right) = \exp\left(-\frac{\pi x}{2I_x}\right) \tag{2.100}$$

is exponential form. Here $x_k$ is a point of reference, $x + x_k$ is a point some distance away from the reference point and $m = x/\Delta x$. $I_x$ is the integral length scale.

To generate a two-dimensional inflow velocity profile for three-dimensional flow, the two-dimensional filter coefficients are defined as

$$b_{jk} = b_j b_k \ . \tag{2.101}$$

At the zero time step, the velocity field (fluctuation part) is computed by Eq. (2.96). At the next step, the velocity field is calculated in the same way and then correlated in time to the previous calculated velocity field by:

$$\Psi_k = v_k^{old} \exp\left(-\frac{\pi \Delta t}{2\tau}\right) + v_k \sqrt{1 - \exp\left(-\frac{\pi \Delta t}{2\tau}\right)} \ . \tag{2.102}$$

Here $\Psi_k$ is the velocity field for the new step, $v_k^{old}$ is the velocity field of old step and $v_k$ is the filtered velocity field, $\Delta t$ is the time step and $\tau$ is the Lagrangian time scale. Eq. (2.102) enforced the velocity field to follow the two-points correlation in steam-wise direction.

For turbulent inflow with mean inflow velocity of $\bar{u}$, $\bar{v}$, $\bar{w}$ and Reynolds

stress value of $R$, the velocities at inflow boundary are:

$$\begin{bmatrix} u \\ v \\ w \end{bmatrix} = \begin{bmatrix} \langle u \rangle \\ \langle v \rangle \\ \langle w \rangle \end{bmatrix} + \begin{bmatrix} \sqrt{R_{11}} & 0 & 0 \\ R_{21}/\sqrt{R_{11}} & \sqrt{R_{22} - (R_{21}/\sqrt{R_{11}})^2} & \\ 0 & 0 & \sqrt{R_{33}} \end{bmatrix} \begin{bmatrix} u^u \\ v^v \\ w^w \end{bmatrix} \tag{2.103}$$

where $u^u, v^v, w^w$ are the velocity fluctuation calculated by Eq. (2.102).

Experiment shows that the scramjet model combustor has an inflow turbulence intensity of 1.6% ($u^{'}/U$ where $u^{'}$ is the rms value in one the three components). Considering that the energy in the randomized filed tends to dissipate very quickly and we are using WENO solver, a turbulence inflow with density of 2.3% is implemented. We have

$$R_{11} = R_{22} = R_{33} = \overline{u^{'}u^{'}} = \overline{v^{'}v^{'}} = \overline{w^{'}w^{'}} = 1939m^2/s^2 \tag{2.104}$$

and

$$R_{ij} = 0 \ (i \neq j) \tag{2.105}$$

The integral length scale $I_x$ is set to 1.0 cm.

# Chapter 3

# Turbulent Boundary Layer

In the supersonic ramjet problem, LES is used to simulate the turbulent flow. Turbulence gives rise to eddies of different length scales. The large and most energetic eddies scale with the bulk velocity and the integral length scale while the smallest eddies scale with the dissipation rate and the Kolmogorov length scale. By Kolmogorov's hypothesis, these small eddies are universal and can be modeled. LES computes the energetic and flow dependent large eddies directly and models the small eddies. LES can achieve good accuracy with a lower computational cost than Direct Numerical Simulation (DNS) at high Reynolds numbers.

LES loses its power for flows at a boundary layer. LES assumes a separation between the large energetic eddies and the small eddies. At a boundary layer, the large and energetic eddies scale with the distance from the wall. The grid size that resolves the main stream flow is not sufficient to resolve such energetic eddies at the boundary layer. To resolve the boundary layer, refined grids near the boundary are commonly

used. Wall-resolved LES has a grid scaled with the small eddies at the wall, including the inner most part of the boundary layer. However, the computational cost to resolve the inner most layer can be as expensive as DNS. Due the computational burden to resolve the inner layer, it is generally accepted that the inner layer should be modeled, rather than resolved.

Despite the difficulty of resolving the boundary layer, the ability to capture near wall processes is very important for the scramjet simulation. Larsson [36] has performed a Rayleigh-Fanno analysis of the Hyshot combustor at nominal conditions, with combustion heat release, wall friction and wall heat losses taken from RANS. It shows that the pressure-change due to these phenomena is about +1 bar (with combustion heat release), +1 bar (with wall friction), and -1 bar (with wall heat losses) compared with the RANS pressure of 2.5 bar.

## 3.1 Introduction to Turbulent Boundary Layer

Turbulent boundary flow is different from a laminar boundary flow. In a laminar boundary flow, there are well-behaved stream lines. In a turbulent boundary flow, many vortices exist in the near wall region. Fig. 3.1 shows a photo of a fully developed Turbulent Boundary Layer (TBL). The existence of these vortices changes the mean velocity profile at the boundary. Fig. 3.2 compares the velocity profile for a laminar boundary layer and a turbulent boundary layer. The velocity gradient close

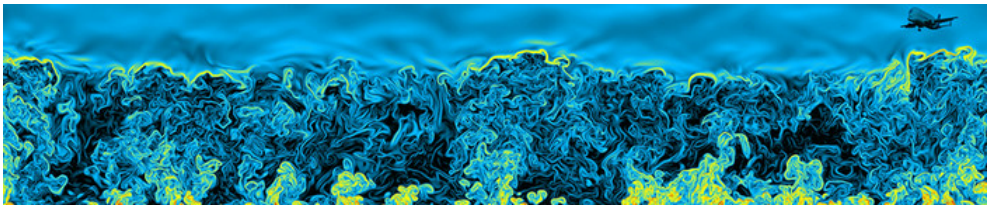

Figure 3.1: Turbulent boundary layer filled with eddies of many different scales (Image source J. R. Garcia [22].)

to the wall is much steeper for a TBL than for a laminar boundary layer.

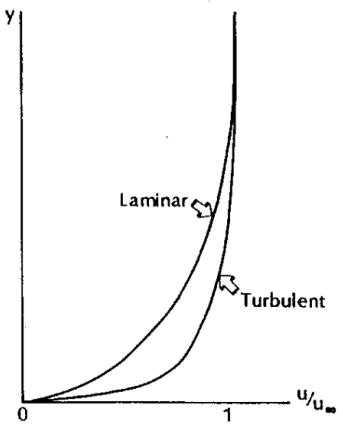


Figure 3.2: Comparison of laminar and turbulent velocity profiles. (Image source Hoffman [27].)

In this section, we follow the exposition of Pope [57]. A TBL has several layers and each layer has distinct turbulent characteristics. These layers are shown in Fig. 3.3.

Here $\delta$ is the boundary layer thickness. The boundary layer thickness $\delta$ has many definitions. The most widely used one is $\delta_{99}$, the value of

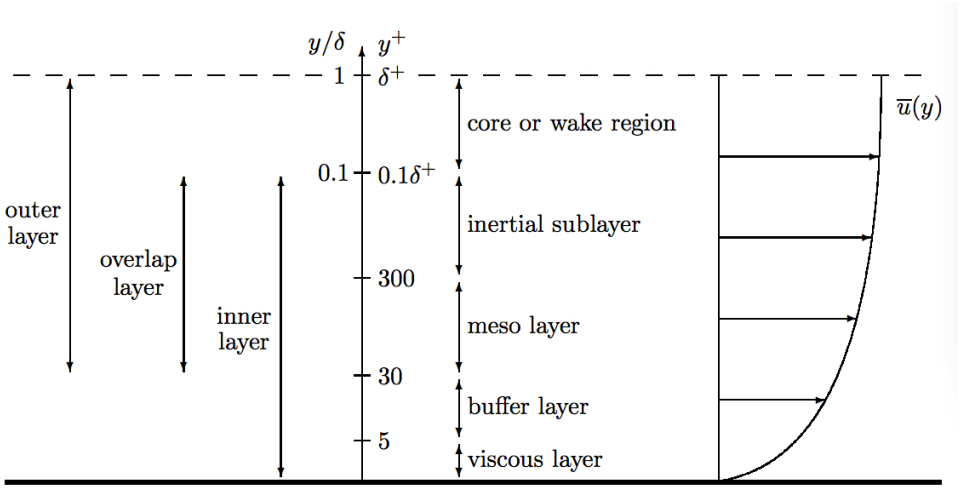


Figure 3.3: Structure of a turbulent boundary layer [37].

wall-normal distance at which point where wall-parallel velocity reaches 99% of the free stream velocity.

Close to the wall, the kinetic viscosity $\nu$ and the wall shear stress $\tau_w$ are the most important parameters. Corresponding viscous velocity scales and length scales are defined based on the the kinetic viscosity $\nu$ and wall shear stress $\tau_w$. The friction velocity:

$$u_\tau \equiv \sqrt{\frac{\tau_w}{\rho_w}} \tag{3.1}$$

is the viscous velocity scale. The velocity measured in terms of the friction velocity is denoted by

$$u^+ \equiv \frac{u}{u_\tau} = \frac{u}{\sqrt{\frac{\tau_w}{\rho_w}}} \, . \tag{3.2}$$

The viscous length scale near the wall is $\delta_\nu = \nu/u_\tau$, which we call the wall unit. The distance from the wall measured in wall-units is denoted by

$$y^+ \equiv \frac{y}{\delta_\nu} = \frac{\nu}{u_\tau} y \ . \tag{3.3}$$

$y^+$ and $u^+$ are dimensionless variables. $y^+$ can be seen as a local Reynolds number. It determines the relative important effects of the viscous and turbulence phenomena. In the viscous wall region, defined as $y^+ < 50$, the effects of molecular viscosity on the shear stress are large; while in the outer layer, defined as $y^+ > 50$, the effects of molecular viscosity can be neglected. In the viscous sublayer, defined as $y^+ < 5$, the turbulent shear stress is much smaller than molecular shear stress.

According to Prandtl, the inner layer in a sufficiently high Reynolds number flow has a velocity profile determined by viscous scale. and the inner layer profile is independent of the main stream velocity. In other words, $u^+$ is a function of $y^+$ only. The inner layer can be divided into three parts: the viscous sublayer, the buffer layer and the log-law layer. In the viscous sublayer, where $y^+ < 5$, the turbulent shear stress can be neglected compared to the molecular shear stress. A linear relationship holds for the viscous sublayer:

$$u^+ = y^+ \ . \tag{3.4}$$

In the overlap region of the inner and outer layers, the logarithmic law

of the wall of Von Karman holds:

$$u^+ = \frac{1}{\kappa} ln(y^+) + B \ . \tag{3.5}$$

Here, $B$ is a constant and $\kappa$ is the von Karman constant, with approximate values:

$$\kappa = 0.41, \quad B = 5.2 \ . \tag{3.6}$$

The region between the viscous sublayer and the log-law region is called the buffer layer.

## 3.2 Wall Resolved LES

Wall Resolved LES has expensive calculation cost for flow with high Reynolds number. To resolve the whole boundary layer stucuture, the Wall Resolved LES need to resolve the dynamics of the inner layer dominated by quasi-streamwise vortices which have sizes in same order with viscose length scale $\delta_\nu$. To resolve the inner layer, it need a constant grid spacing scaled with wall unit.

Assume that the domain LES resolves in the inner layer has a size of $C_1\delta \times C_2\delta \times N\delta_\nu$ (We assume we solve the inner layer from the wall up to the position of $y^+ = N$). To resolve the inner layer, LES should have a grid size of $\Delta \sim \delta_\nu$. Thus the grid needed in the wall parallel direction is $C_i\delta/\Delta \sim \delta/\delta_v$ $(i = 1, 2)$ cells. According to Pope, the length scale ratio $\delta/\delta_v$ increases approximately as $0.09Re^{0.88}$. Here the Reynolds number

is the bulk Reynolds number of the main stream:

$$Re_b \equiv \frac{U_b \delta}{\nu} \ . \tag{3.7}$$

In the wall normal direction, we need $N$ cells. Thus the total number of cells needed to resolve the inner layer is

$$N_{\text{inner}} = N \left( \frac{C_1 \delta}{\Delta} \right) \left( \frac{C_2 \delta}{\Delta} \right) \sim \left( \frac{\delta}{\delta_\nu} \right)^2 \sim Re_b^{1.76} \ . \tag{3.8}$$

Thus it is very expensive for LES to resolve the inner layer.

In contrast to the inner layer, the cost to resolve the outer layer is much smaller. In the inviscid outer layer, the energetic motions scale with the outer length scale $\delta$. Chapman [13] estimated the number of cells need to resolve the outer layer is proportional to $Re^{0.4}$ for flat plat boundary layer and independent of $Re$ for plane channel flow.

Fig. 3.4 shows the number of cells needed to resolve the boundary layer for plane channel flow. At Reynolds number of $O(10^6)$, about 99% of the points are used to resolve the inner layer (the inner 10% of the boundary layer). For high Reynolds numbers, we could only afford the coarse grid size which only resolve the out layer in LES. The computational cost of the coarse grid is still independent or weekly dependent of $Re$.

When the LES is implemented on coarse grid which only resolved the outer layer and does not resolve the inner layer, numerical errors rises in the near-wall region. As we seen in Fig. 3.2, velocity gradient is larger

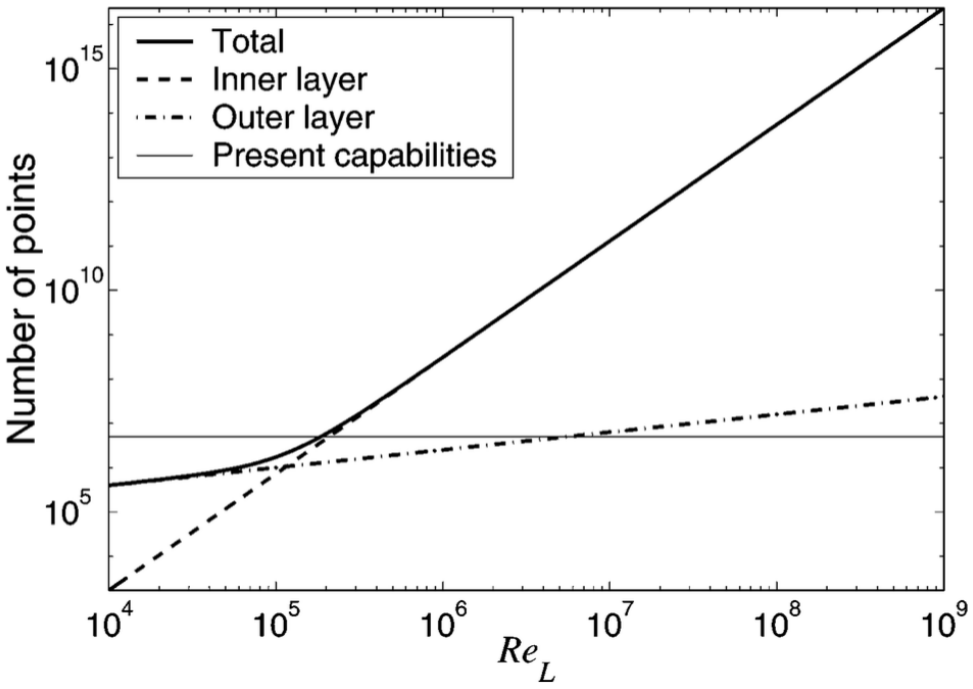


Figure 3.4: The number of cells needed to resolve the boundary layer for plane channel flow. (Image source Piomelli [53].)

near the wall. Coarse grid LES will underestimate the wall shear stress and distorts the exterior LES if the no extra model is applied for inner layer LES. Thus wall model is needed for the inner layer on the coarse grid simulation.

## 3.3 Wall Modeled LES

There are many approaches for the modeling of inner layer [53]. These models are divided to two catergories: wall stress models that calculate the wall shear stress and hybrid LES/RANS method.

Hybrid LES/RANS method (left plot of Fig. 3.5) uses the RANS to simulation the near-wall region and LES in the exterior region. The grid resolution tangential to the wall are determined by the exterior LES, the grid resolution normal to the wall are determined by RANS. The hybrid LES/RANS method is a successful and widely used wall model. However, Hybrid LES/RANS method is numerically more expensive than wall-stress model because full evolution equations are solved down to the wall. Another drawback of hybrid LES/RANS method is that the skin friction calculated is consistently under-predicted by around $10\% - 15\%$.

In the wall-stress model, the LES extends all the way down to the wall. LES only resolves the outer layer motion. The inner layer motion is resolved by a simplified wall model. The wall model relate the instantaneous velocity and temperature in the overlap layer from the LES to the wall shear stress and heat flux, and provides them as a boundary

condition back to the LES.

The wall model can be algebraic functions, the logarithmic law for example, or differential equations (the thin boundary layer equation) solved on a local embedded grid. The wall model used in our model scramjet combustor simulation is the equilibrium wall model of Larsson [32].

## 3.4 Equilibrium Wall Model

The equilibrium wall model is derived from the thin boundary layer equation with the assumption that the change of physical variables along direction tangential to the wall is much smaller compared with the change along wall normal direction and we can introduce the approximation that the physical variables are constant along wall parallel directions. Another assumption is the equilibrium assumption (the pressure is constant). As a result there are only two independent variables in the equilibrium wall model for compressible flow: the velocity and the temperature. The governing equations for equilibrium wall model are:

$$\frac{\partial}{\partial y}\left[(\mu+\mu_t)\,\frac{\partial u}{\partial y}\right]=0\ , \tag{3.9}$$

and

$$\frac{\partial}{\partial y}\left[c_p\left(\frac{\mu_t}{Pr_t}+\frac{\mu}{Pr}\right)\frac{\partial T}{\partial y}+(\mu+\mu_t)\,u\frac{\partial u}{\partial y}\right]=0\ . \tag{3.10}$$

Here $\rho_w$ and $\tau_w$ are the local instantaneous density and wall stress. The thin boundary layer equation and the equilibrium wall model equations

are simplified RANS equations. See Sec. A for the deviation.

The interaction of the inner layer wall model and outer layer LES is shown in Fig. 3.5. We first pick a point in the overlap region of the inner layer and outer layer as the matching point. The governing one dimensional equations Eqs. (3.9-3.10) are solved on embeded grid from the matching point all the way down to the wall. The temperature, velocity and species concentration at the matching point from LES set the outer boundary condition of Eqs. (3.9-3.10). The no-slip boundary condition of Eqs. (3.9-3.10) is applied at the Wall. After Eqs. (3.9-3.10) are solved, we obtain the tangential velocity and temperature gradient in wall-normal direction, which give the wall shear stress and heat flux. Then the wall shear stress and heat flux are fed back to the outer layer LES.

In order to resolve the wall normal velocity and temperature gradient, the first off-wall point should have a small distance from wall in the same order of wall-units. The our implementation, the first node is at $y^+ = 1$. Then geometric grid stretching is used for embedded grid from wall to the matching point. In this way, the number of grid points $N$ from the wall to the matching point is proportional to $log(Re)$. It is weakly dependent on the Reynolds number. In our simulation, N is approximately 50.

The calculation of the viscosity coefficient $\mu$ and heat capacity $c_p$ of the gas mixture are introduced in Sec. 2.2.3. The dynamic viscosity $\mu_t$ is

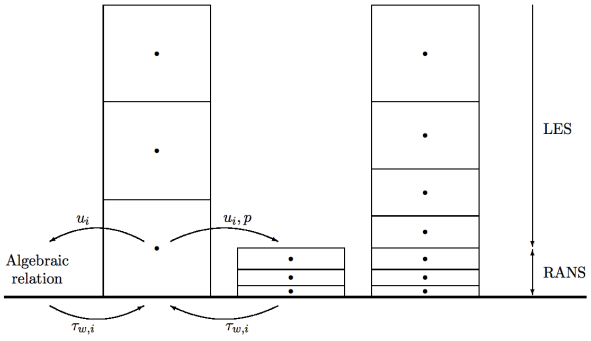


Figure 3.5: Sketch of Wall model by Larsson [37]. Left plot shows the wall-stress models. The filtered Navier-Stokes equation are solved on the left grid. The wall shear stress are estimated from algebraic relation or by solving thin boundary layer equation on embed grid (middle grid). Right plot demonstrate the hybrid LES/RANS model. The Navier Stokes equations are solved on the right grid with different turbulence models for LES and RANS parts).

computed by the mixing-length model:

$$\mu_t = \kappa \rho_w y \sqrt{\frac{\tau_w}{\rho_w}} \left[ 1 - \exp\left( -\frac{y^+}{A^+} \right) \right]^2 . \tag{3.11}$$

The Von Karman constant $\kappa = 0.41$, and $A^+ = 17$. Since coefficients $\mu$, $\mu_t$, and $c_p$ on the embedded grids are dependent of the solution of one dimensional equations Eqs. (3.9-3.10), an iterative solver needs to be used. We start from an initial guess: linear profiles of $u$ and $T$. We compute coefficients $\mu$, $\mu_t$ and $c_p$ on each point based on the initial linear solution. Then we solve the governing equations Eqs. (3.9-3.10) with single tridiagonal matrix algorithm (TDMA) sweep. After that, we obtain the new state variable $u$ and $T$. We compute the new coefficients $\mu$, $\mu_t$ and $c_p$. We repeat the process until the distribution of state variables $u$ and $T$ converge.

After we have converged to a state variable distribution $u$ and $T$ in the inner layer, we compute the wall shear stress and heat flux by

$$\tau_w = -\mu_w \frac{u_0}{y_0} , \tag{3.12}$$

and

$$q_w = -\frac{c_p}{Pr} \mu_w \frac{T_0 - T_w}{y_0} . \tag{3.13}$$

## 3.5 Grid Sensitivity Study of the Turbulent Boundary Layer Model

### 3.5.1 Configuration

In this section, we study the grid sensitivity of the boundary layer model for 2D simulations of a supersonic flat plate boundary layer. The inflow $O_2$ has an average density of $1.241\times10^{-4}$ kg/m$^3$, velocity of 1890 m/s and temperature of 1276 K, same with the scramjet inflow condition. If we have laminar inflow, the supersonic flow above the flat plate has a transition from a laminar boundary layer to a turbulent boundary layer at a position downstream from the inlet. The transition is shown in Fig. 3.6.

However, the distance from the inlet to the transition point is too long to be computationally affordable. Thus to have fully developed turbulence, the rescaling-reintroducing method of Urbin and Knight [66] is used. We discuss this method in Sec. 3.5.2.

In our TBL simulation, the wall is located at $y = 0$. The computational domain is [240, 10] mm in the stream-wise and wall-normal directions. The recycling station is located at 40 mm downstream of the inflow. To get fully developed boundary layer turbulence through the rescaling and reintroducing method, the simulation was run for about 20 flow throughs. Here $\delta$ is the inflow boundary layer thickness with value of $\delta = 2.25$ mm.

The error in the calculation of the wall shear stress and the heat flux

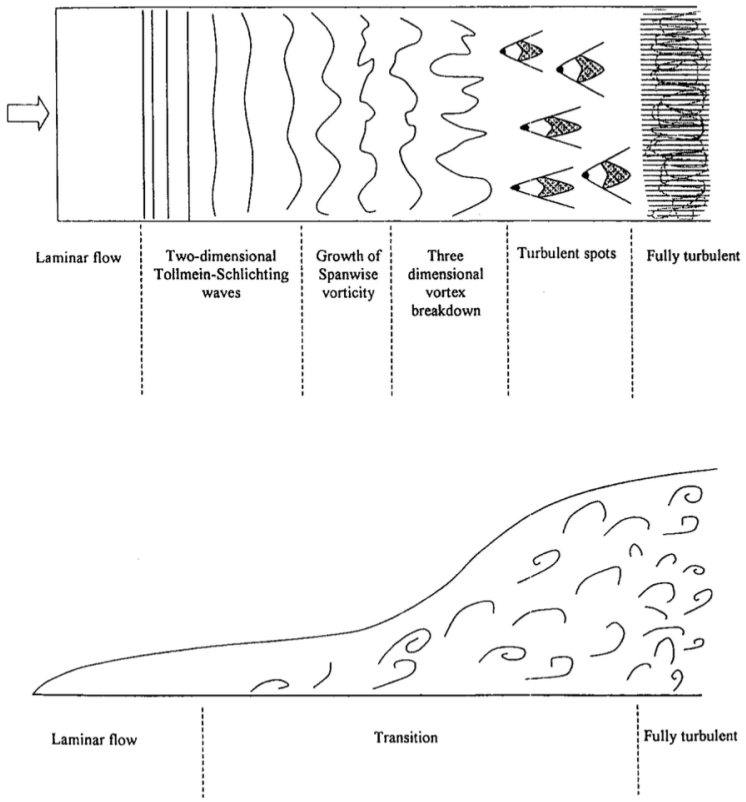


Figure 3.6: Image of an idealized transition process on a flat plate. (Image source Hoffman [27].)

has two sources: First, the model error of the turbulent boundary layer model; Secondly, the discrepancy between the real state variables ($u$ and $T$) and the numerical value of these values. This is to say that the physical profile of the matching point might not be well resolved.

Larsson [32] argued that the second error is un-avoidable, because the first grid cell off the wall can not be well resolved. Larsson also indicates that we could greatly reduced the second error by not using the first grid cell off the wall. We will discuss this question in Section 3.5.3.

### 3.5.2 Turbulent Wall Bounded Flow Generation

We have discussed the digital filtering method in producing the free stream turbulence in Sec. 2.5. The Rescaling-Reintroducing method is a popular method to introduce inflow boundary turbulence. The Rescaling-Reintroducing method was first proposed by Spalar [63]. Lund [42] introduced modifications in the method to deal with the growth terms. Urbin further modified the method to adapt better to the compressible turbulent boundary layer. Here we follow the exposition of Urbin [66].

The idea of the Rescaling-Reintroducing method can be seen in Fig. 3.7. We take the flow field at a downstream station, rescaled it and impose it as inflow condition. In the rescaling step, flow field components are decomposed into time averaged and fluctuation parts. Separate scaling laws are applied to each part.

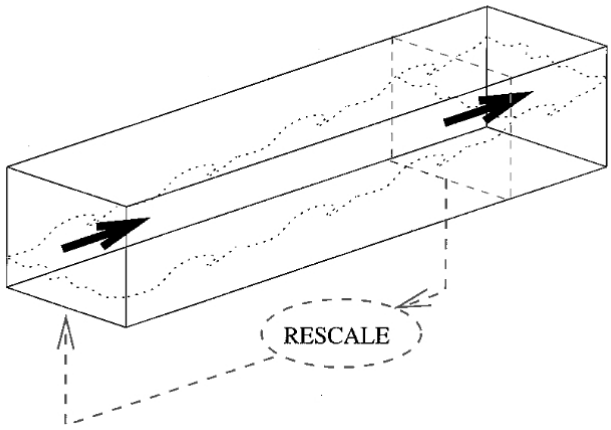


Figure 3.7: Generation of inflow boundary condition. The plot comes from Urbin [66]

For compressible flow, we apply the Van Driest-Fernholz and Finley transformation of the velocity $U$, denoted as $U_{\mathrm{VD}}$:

(3.14)

$$U_{\mathrm{VD}} = \frac{U_\infty}{A} sin^{-1}\left(A\frac{U}{U_\infty}\right) \ , \tag{3.15}$$

and

$$A = \sqrt{\frac{[(\gamma-1)/2]M_\infty^2 Pr_t}{1+[(\gamma-1)/2]M_\infty^2 Pr_t}} \ , \tag{3.16}$$

where $Pr_t = 0.89$. The inner layer and outer layer are scaled in different ways. For the inner layer, we have by the law of the wall:

$$U_{\mathrm{VD}}^{\mathrm{inn}} = \mu_\tau(x) f_1(y^+) \ . \tag{3.17}$$

On the outer layer, we have by the defect law:

$$U_{\mathrm{VD}}^{\infty} - U_{\mathrm{VD}}^{\mathrm{out}} = \mu_{\tau}(x) f_2(\eta) \ , \tag{3.18}$$

where $\eta = y/\delta$ is the outer coordinate. The functions $f_1$ and $f_2$ are both universal and are independent of x. Thus we have the scaling law:

$$U_{\mathrm{VD,\ inl}}^{\mathrm{inn}} = \beta U_{\mathrm{VD,rec}}(y_{\mathrm{in}}^{+}) \ , \tag{3.19}$$

for the inner region and

$$U_{\mathrm{VD,\ inl}}^{\mathrm{out}} = \beta U_{\mathrm{VD,\ rec}}(\eta_{\mathrm{inl}}) + (1-\beta) U_{\mathrm{VD}}^{\infty} \ , \tag{3.20}$$

in the outer layer. Here the subscript inl denotes the inlet and rec denotes the recycling station. $\beta$ is the ratio of friction velocity at the inlet station and the velocity at the recycled station. The treatment of the fluctuation part is similar. The velocity fluctuation in the inner and outer sides are rescaled by:

$$u_{\mathrm{inl}}^{''\mathrm{inn}} = \beta u_{\mathrm{rec}}^{''}(y_{\mathrm{inl}}^{+}, z, t), \quad u_{\mathrm{inl}}^{''\mathrm{out}} = \beta u_{\mathrm{rec}}^{''}(\eta_{\mathrm{inl}}, z, t) \ . \tag{3.21}$$

The rescaling of the mean wall-normal velocity and the temperature is:

$$V_{\mathrm{inl}}^{\mathrm{inn}} = V_{\mathrm{rec}}(y_{\mathrm{inl}}^{+}), \quad V_{\mathrm{inl}}^{\mathrm{out}} = V_{\mathrm{rec}}(\eta_{\mathrm{inl}}) \ , \tag{3.22}$$

and

$$T_{\rm inl}^{\rm inn} = T_{\rm rec}(y_{\rm inl}^{+}), \quad T_{\rm inl}^{\rm out} = T_{\rm rec}(\eta_{\rm inl}) \ . \tag{3.23}$$

Here we assume that the steamwise pressure gradient is small compared with the wall-normal temperature gradient. The fluctuation $v_{\rm inl}^{''\rm inn}$ of the wall-normal velocity is calculated in the similar way of $u^{''}$. Assuming the pressure fluctuations are assumed to be small compared with temperature fluctuations, the fluctuation of temperature is scaled as:

$$T_{\rm inl}^{''\rm inn} = T_{\rm rec}^{''}(y_{\rm inl}^{+}, z, t), \quad T_{\rm inl}^{''\rm out} = T_{\rm rec}^{''}(\eta_{\rm inl}, z, t) \ . \tag{3.24}$$

Finally, we take a weighted average of the inner and outer profile for the complete profile of velocity and temperature:

$$u_{\rm inl} = (U_{\rm inl}^{\rm inn} + u_{\rm inl}^{''\rm inn})[1 - W(\eta_{\rm inl})] + (U_{\rm inl}^{\rm out} + u_{\rm inl}^{''\rm out})W(\eta_{\rm inl}) \ , \tag{3.25}$$

with the weight

$$W(\eta) = \frac{1}{2}\left(1 + \left\{tanh\left[\frac{4(\eta - B)}{(1-2B)\eta + B}\right]/tanh(4)\right\}\right) \ . \tag{3.26}$$

### 3.5.3 Choice of the Matching Point

In the calculation of the wall shear stress and heat flux, the first grid cell off the wall is commonly used as the matching point. Larsson [32] demonstrated that there are persistent numerical and subgrid errors in the matching point if we use this choice, while a better choice can elim-

inate this persistent error.

Assume the wall is located at y = 0 and the matching point is located at $y = y_m$. Assume $y_m$ is located at $y^+ > 50$, in the log layer. The length scale of motions in the log layer is proportional to the wall distance y. Assuming the stress carrying motion has length scale $L_i = C_i y$ (i = 0, 1, 2) and assuming that we need $N$ cells located within this length scale to resolve the stress carrying motion, we have

$$\Delta x_i \leq \frac{L_i}{N} = \frac{C_i y_m}{N} \ . \tag{3.27}$$

If we use the first grid off the wall as the matching point, which means $y_m = \Delta y$, we will have

$$\Delta y \leq C_1 \frac{\Delta y}{N} \ , \tag{3.28}$$

which means $C_1 \geq N$. However, the numerical Nyquist criterion indicates $N \geq 2$. And the kinematic damping by the wall indicates $C_1 < 2$. Thus Eq. (3.28) does not hold. It means that the dynamics at the first grid off the wall could not be well resolved. The TBL model is fed with inaccurate information if we choose the first grid cell off the wall as the matching point.

Larsson observed that it is not required that the TBL to be applied between the first grid point and the wall; actually the TBL model equations are valid for any interval from the wall to a point in the inner layer. Larsson found that he could achieve grid convergence by fixing $y_m$ and refining the grid.

### 3.5.4 Results and Analysis

To study the grid convergence of the wall shear stress and the heat flux as the resolution is varied, we conduct numerical experiments with four levels of resolution, see Table 3.1. At each level of grid resolution, we

Table 3.1: Grid resolution study of the turbulent boundary layer

| simulation | $\Delta$x (mm) | $\Delta$y (mm) |
|---|---|---|
| grid level I | 0.5 | 0.5 |
| grid level II | 0.25 | 0.25 |
| grid level III | 0.125 | 0.125 |
| grid level IV | 0.125 | 0.0625 |

conduct two simulations with two choices of the matching point location: the first choice is to set the matching at a fixed location of $y_m = 0.25$ mm while in the second choice the matching point is the first cell off the wall.

The average shear stress and heat flux at the wall in each simulation are shown in Fig. 3.8. The shear stress and heat flux are averaged from the recycling station to the outlet. The averaged boundary thickness is about 3.0 mm from the recycling station to the outlet, corresponding to a averaged inner layer thickness of about 0.3 mm. Thus the fixed matching poing $y_m = 0.25$ mm is located in the inner layer.

The averaged wall shear stress and heat flux converge with grid refinement when the location of the matching point is fixed ($y = 0.25$ mm).

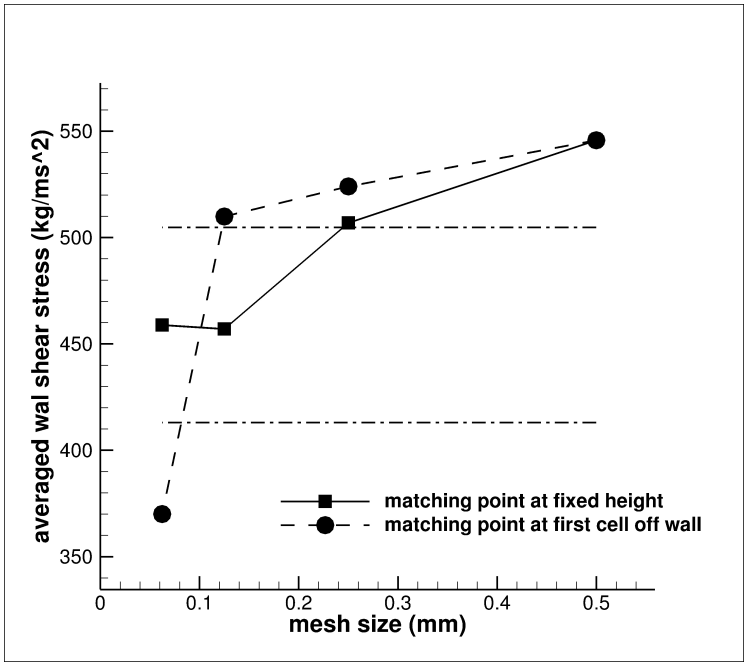


(a) Averaged shear stress at the wall. The dashed dot horizontal lines indicate a ±10 % variation about the averaged shear stress of the finest grid.

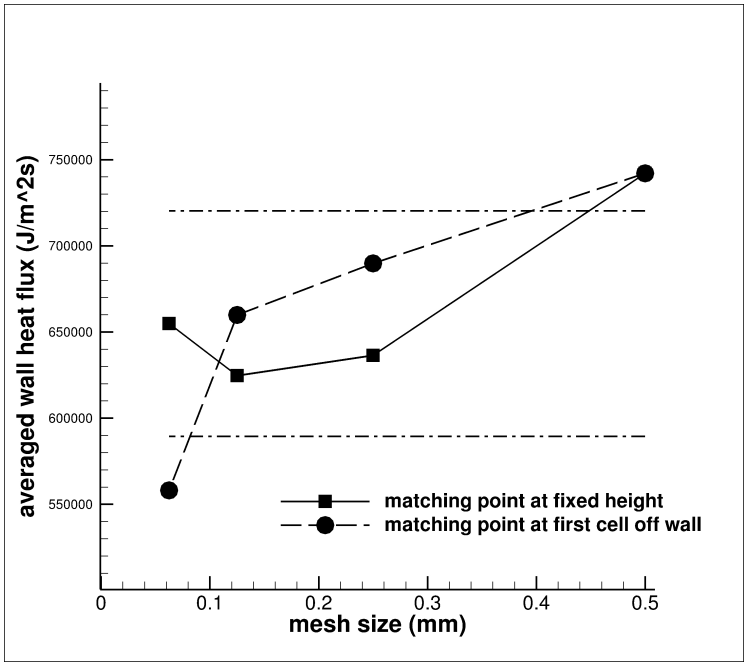


(b) Averaged heat flux at the wall. The dashed dot horizontal lines indicate a ±10 % variation about the averaged heat flux of the finest grid.

The averaged wall shear stress and heat flux computed from use of the first grid cell off the wall as matching point do not converge. This result verifies the point made in Sec.3.5.3: the velocity and temperature profiles at first grid cell off the wall are not well resolved and thus are not accurate; by having the matching point several cells away from the wall, we could achieve convergence of wall shear stress and heat flux.

The average velocity profiles (Fig. 3.9) of four grid resolutions with the matching point fixed at $y = 0.25$ mm also show the convergence trend. The velocity profiles of grid II-IV agree quite well with each other.

Table 3.2: Error ratio of the wall shear stress and heat flux of each simulation. $y_m$ denotes the location of the matching point. By the simulation result of this section, we have an error approximation of the TBL model at different grids.

| $\Delta$y (mm) | $y_m$ (mm) | number of cells from $y_m$ to the wall | number of cells in boundary layer | error ratio in wall shear stress | error ratio in wall heat flux |
|---|---|---|---|---|---|
| 0.5000 | 0.2500 | 1 | 6 | 0.189 | 0.133 |
| 0.2500 | 0.2500 | 2 | 12 | 0.104 | 0.028 |
| 0.1250 | 0.2500 | 3 | 24 | 0.004 | 0.046 |
| 0.0625 | 0.2500 | 5 | 48 | | |
| 0.5000 | 0.2500 | 1 | 6 | 0.189 | 0.133 |
| 0.2500 | 0.1250 | 1 | 12 | 0.142 | 0.053 |
| 0.1250 | 0.0625 | 1 | 24 | 0.111 | 0.008 |
| 0.0625 | 0.0312 | 1 | 48 | 0.194 | 0.148 |

The error ratio of the wall shear stress and heat flux of each simulation are summerized in Table 3.2. Here the marginal convergence of the averaged wall shear stress and heat flux are accessed. Clear convergence

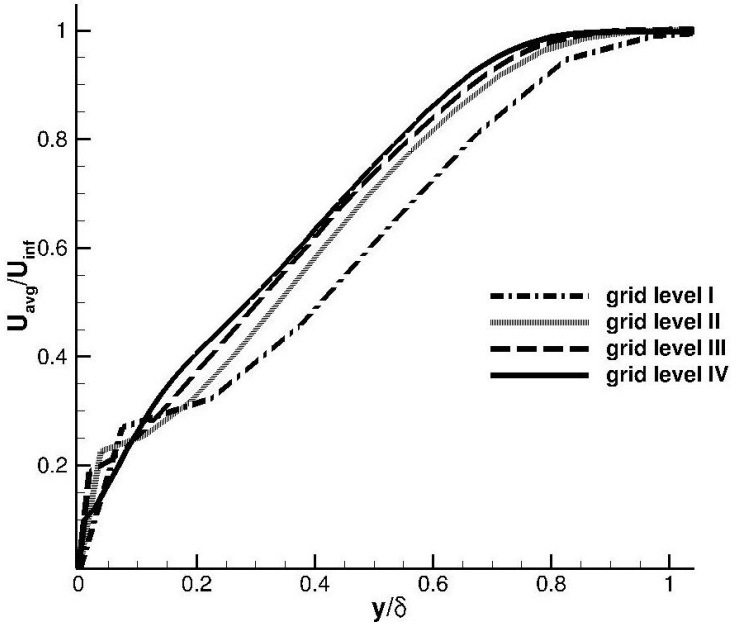


(a) Fixed matching point at y = 0.25 mm

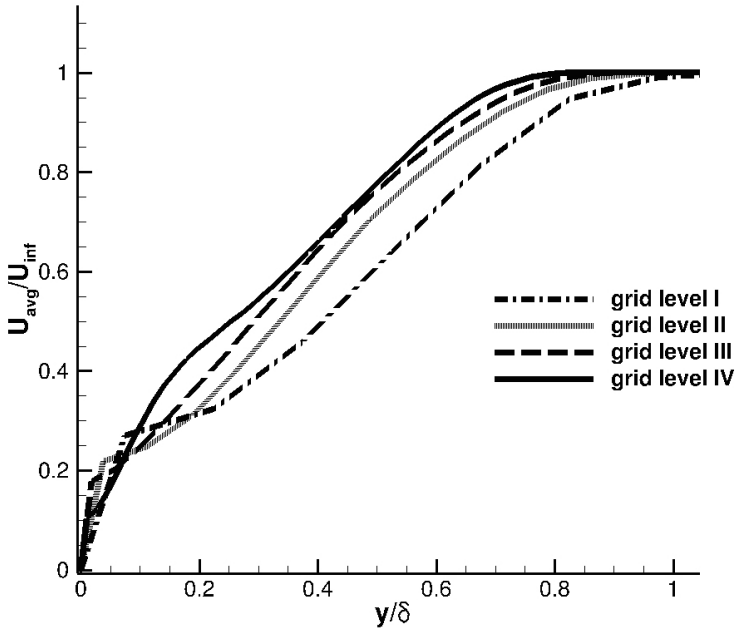


(b) Use first cell off the wall as matching point

Figure 3.9: Average velocity profiles for different grids in the boundary layer. $U_{inf}$ is the free stream velocity. Note specifically the compare of Grid II to III in the range of $0.2 < y/\delta < 0.6$. The importance of (a) over (b) is subtle but

might require one more level of mesh refinement. We observe from Table 3.2 :

(a) At grid level IV and grid level III, when grid size $\Delta y$ is less or equal to 0.125 mm and we have $\geq 3$ cells from the matching point to the wall the ratio of discrepancy is about 5% for both the wall shear stress and the heat flux. The average wall shear stress and heat flux have achieved marginal convergence.

(b) At grid level II when grid size $\Delta y$ is less or equal to 0.25 mm and we have 2 cells from the matching point to the wall, the ratio of error is about 10% for both the wall shear stress and the heat flux;

(c) Using the first cell of the wall as the matching point introduces an consistent error of about 20% in the averaged wall shear stress occurs even at the finest grid level.

As a conclusion, we obtain a decreased error in the calculation of wall shear stress and heat flux as we have more grid resolution within the boundary layer and more cells located between the wall and the matching point wall normal direction. To obtain a better accuracy in the calculation of the wall shear stress and heat flux, it is better to have local mesh refinement at the boundary. If a maximum of 10% error is allowed in the averaged values of wall shear stress and heat flux, it is predicted that a mesh resolution of $\Delta y \geq 0.25$ mm is required for the scramjet simulation.

On the choice of the matching point, we should abandon the use of the

first grid off the wall. The only requirement for he matching point is that it should be located in the inner layer, the matching point could located from the first cell up to the nth cell off the wall where $n = 0.1\delta/\Delta$. Larsson estimated using the fourth cell off the wall is sufficient to have accurate input at the matching point. Thus we can choose the matching point location to be

$$n = min\left(\frac{0.1\delta}{\Delta}, 4\right) \tag{3.29}$$

# Chapter 4

# Turbulent Combustion

In gaseous combustion, two classes of flames are often considered: premixed and non-premixed (diffusion) flames. A premixed flame is a flame in which the oxidizer has been mixed with the fuel before it reaches the flame front. For example, combustion in homogeneous charge spark ignition engines are premixed flames. A diffusion flame is a flame in which the oxidizer combines with the fuel by diffusion. In diffusion flame, reactants are initially separated, and reaction occurs only at interface between fuel and oxidizer. One example of a diffusion flame is a candle flame. The flame in scramjet combustor is also a diffusion flame.

In this chapter, we study the grid sensitivity of our finite rate chemistry model in the context of one-dimensional and two-dimensional flows. The grid sensitivity analysis in three dimensional simulation is too expensive for a detailed exploration of all its many parameters. Based on 1D and 2D simulations, we excluded some model and parameter choices. In 1D, we study the grid sensitivity in resolving the premixed and non-premixed

laminar flames with detailed and reduced mechanism separately. In 2D, we study the the gird sensitivity of turbulent combustion. Then we use the turbulent diffusion coefficient computed in a 2D and 3D context in the 1D problem analysis to and get a less stringent mesh requirement.

## 4.1 Chemical Kinetics

In balance equations for the mass fraction of species i:

$$\frac{\partial}{\partial t}\left(\rho Y_i\right) + \frac{\partial}{\partial x_j}\left(\rho u_j Y_i\right) = \frac{\partial^2}{\partial x_j^2}\left(\rho d_i Y_i\right) \; + \dot{m}_i \; , \tag{4.1}$$

$\frac{\partial}{\partial t}\left(\rho Y_i\right)$ is the local rate of change and $\frac{\partial}{\partial x_j}\left(\rho u_j Y_i\right)$ is the convection term. $\frac{\partial^2}{\partial x_j^2}\left(\rho d_i Y_i\right)$ is the diffusive flux. $\dot{m}_i$ is the chemical source term, the calculation of which involves the chemical Kinetics.

The reaction rate $w_j$ for single reaction $j$ follows the Law of Mass Action: the reaction rate is proportional to the products of the concentration reactants. The reaction rate $w_j$ for reaction $j$ in a mechanism with $n$ reactions is

$$w_j = k_{fj} \prod_{i=1}^{n} \left(\frac{\rho Y_k}{M_i}\right)^{\nu_{ji}} - k_{rj} \prod_{i=1}^{n} \left(\frac{\rho Y_i}{M_i}\right)^{\nu''_{ji}}. \tag{4.2}$$

Here $k_{fj}$ and $k_{rj}$ represent forward and reverse rate coefficients of reaction $j$ as a function of the temperature. $\nu_{ji}$ and $\nu''_{ji}$ are the stoichiometric coefficients of species $i$ for the reaction and production side of reaction

$j$. The forward and reverse rate coefficients $k_{fj}$ and $k_{rj}$ can be computed empirically by the Arrhenius Law. The forward rate coefficient is:

$$k_{fj} = A_j T^{n_j} \exp\left(\frac{-E_j}{RT}\right) , \tag{4.3}$$

where $A_j$, $n_j$ and $E_j$ are the pre-exponential constant, the temperature exponent, and the activation energy of reaction $j$. Their values can be found in the reaction mechanism tables. The reverse rate coefficient $k_{rj}$ is computed from the forward coefficient and the equilibrium constant from reaction $j$ by

$$k_{rj} = \frac{k_{fj}}{\left(\frac{P_a}{RT}\right)^{\sum_{i=1}^{n} \nu_{ji}} exp\left(\frac{\Delta S_j}{R} - \frac{\Delta H_j}{RT}\right)} \tag{4.4}$$

where $P_a = 1$ bar. The $\Delta H_j$ and $\Delta S_j$ are respectively the enthalpy and entropy changes of reaction $j$.

The chemical source term, the production rates $\dot{m}_i$, is the sum over all production terms in the mechanism,

$$\dot{m}_i = \sum_{j=1}^{N} M_i \nu_{ji} w_j , \tag{4.5}$$

where $N$ is the number of reactions, $M_i$ is the molecular mass of species $i$, $w_j$ is the rate for reaction $j$ and $\nu_{ji}$ is the stoichiometric coefficient of species $i$ in the reaction $j$.

The heat release rate is expressed as the sum over the heat release of all

chemical reactions:

$$H_i = \sum_{j=1}^{N} M_i h_i w_j \tag{4.6}$$

where $h_i$ is the heat release in reaction $i$.

In last several decades, lots of experiment has been done to measure the rate of gas phase reactions. Many authors have selected reactions and their rate data and combined them elementary reaction tables. In our problem, the fuel is $H_2$. There are many studies of the detailed hydrogen-air reaction mechanisms, such as Jachimowski's 33-reaction mechanism [30], Hong et al.'s 21-reaction mechanism [28] and Williams's 21-reaction mechanism [70]. Additional discussion can be found from the text and references cited in [2, 5, 73, 59, 16]. The mechanism by [28] has 8 species (H, O, OH, $H_2O$, $H_2$, $O_2$, $HO_2$, and $H_2O_2$) and 20 reactions, as in Tab. 4.1. The rates of each reaction with $H_2$ and $O_2$ mixed stoichiometrically under temperatures of 1276 K and a pressure of 100 kPa are shown in Fig. 4.1.

In the detailed mechanism, the chemical source terms $w_i$'s contain the contributions from many fast reactions. Thus, the reactive chemistry equations contain a system of stiff non-linear equations. Solving these non-linear equation requires an adaptive solver and high computational cost [60].

Therefore, the reduced chemistry mechanisms are developed and are widely used. Balakrishnan [3] conducted a numerical investigation of the extinction and ignition limits in laminar non-premixed counter flow

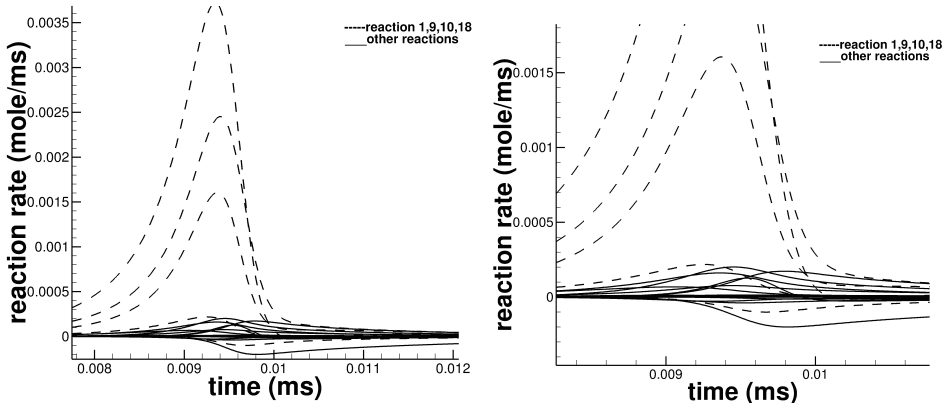


(a) full range of all reactions (b) enlargement showing minor reactions

Figure 4.1: Reaction rates for each reaction in the full chemistry mechanism for $H_2/O_2$ mixed stoichiometrically under model scramjet combustor temperatures of 1276 K and pressure of 100 kPa.

for both detailed and reduced chemistry of $H_2$/Air reactions. Pantano [48] used a four-step reduced mechanism in a 3D direct numerical simulation (DNS) of a spatially evolving planar turbulent reacting jet for the combustion of methane with air.

The reduced reaction mechanism assumes the Quasi-Steady-State for intermediate species. The fast reactions depleting the quasi-steady state intermediate species are eliminated. The slow rate reactions remain and determine the rates of global reactions.

A four-step reaction mechanism [8] for $H_2/O_2$ interactions has been successfully verified against the result of detailed chemistry in the main reaction zone for high-temperature ignition [60]. This four-step reaction mechanism has 15 elementary steps and the 4 global steps.

I) $H + O_2 \rightleftharpoons OH + O$

II) $O + H_2 + M \rightleftharpoons H + OH + M$

III) $OH + H_2 \rightleftharpoons H + H_2O$

IV) $H + H + M \rightleftharpoons H_2 + M$

with global reaction rates as:

$$w_I = w_1 + w_6 + w_{12} + w_{15} - w_{17} + w_{18} - w_{20} + w_{21}$$

$$w_{II} = w_2 - w_3 + w_6 + w_{12} + w_{14} + w_{16} + w_{17} + w_{18} + w_{21}$$

$$w_{III} = w_3 + w_4 + w_8 + w_{10} + w_{13} + w_{15} + w_{18}$$

$$w_{IV} = w_5 + w_9 + w_{10} - w_{12} + w_{16} + w_{17} + w_{20}$$

It neglects $H_2O_2$ and compute the partial density of $HO_2$ from quasi-steady assumption. It aggregates the reaction rates of elementary reactions into 4 global reactions. This four-step reaction mechanism is used in the finite rate chemistry model in our model scramjet combustor simulation.

## 4.2 Flame Structures

### 4.2.1 Premixed Flame

For a premixed flame, the fuel and oxidizer are completely mixed before the combustion takes place. The fuel and oxidizer are mixed at low temperature before they enter the combustion chamber. The chemical

reaction chain is sensitive to the temperature. At low temperature, the "chain-breaking" mechanism drives the reaction chain thus the combustion reactions are "frozin". When a strong heat source (ignitor) raises the temperature beyond the ignition temperature, the combustion starts.

The equivalence ratio of a given mixture is an important parameter for premixed gases. It is defined as

$$\phi = s\frac{Y_F}{Y_O} \tag{4.7}$$

where

$$s = \frac{\nu_O^{'} M_O}{\nu_F^{'} M_F} \tag{4.8}$$

is the mass stoichiometric ratio. Here the index $F$ and $O$ stands for fuel and oxidizer respectively. Rich combustion happens when $\phi > 1$ (the fuel is in excess) and lean combustion happens when $\phi < 1$ (the oxidizer is in excess).

In premixed combustion, there are two stable states, the unburnt states and the burned gas states. They are separated by the flame front as in Fig 4.2. The laminar burning velocity $s_L$, defined as the velocity at which flame front propagate in the direction normal to itself and relative to the flow into the unburnt mixture [51].

A basic case of a premixed flame is a one-dimensional laminar premixed flame. Computing one-dimensional laminar premixed flames can be seen as the first step toward more complex flames. The structure of one

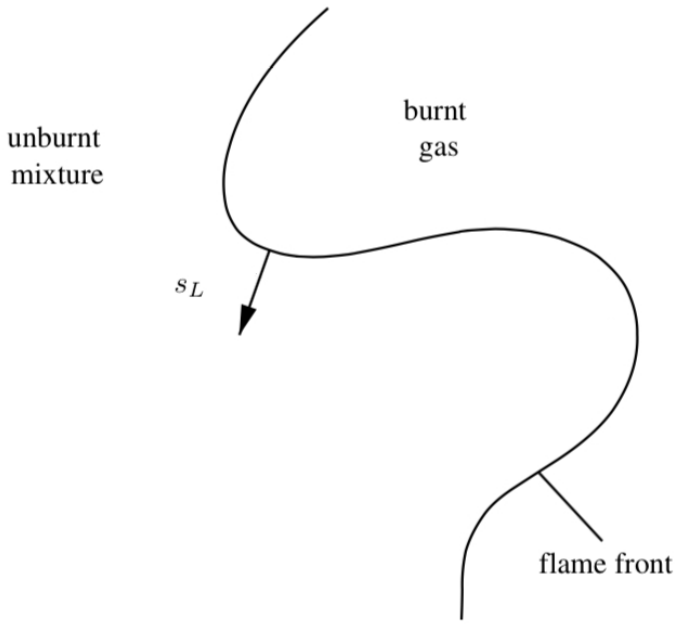


Figure 4.2: Premixed flame (Image source [51]).

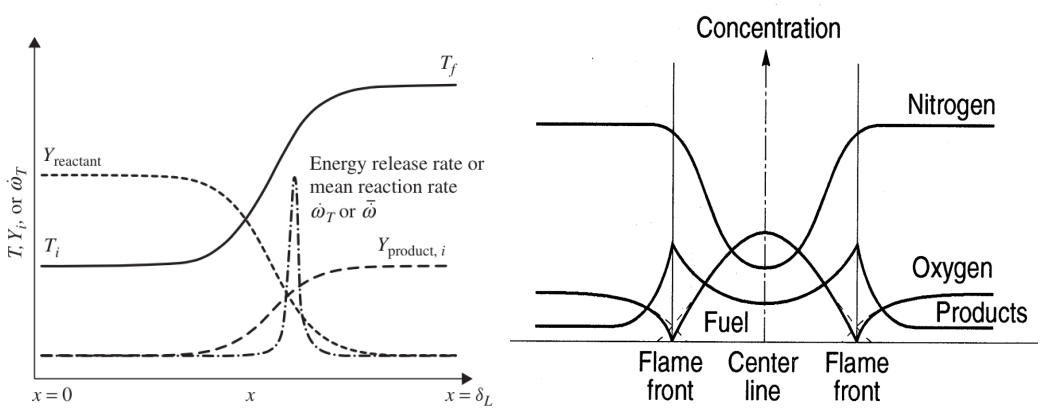


(a) Structure of a laminar premixed flame(b) Structure of a laminar diffusion flame. [1] [35].

Figure 4.3: General Flame structure.

dimensional laminar premixed flame is shown in Fig. 4.3(a).

### 4.2.2 Diffusion Flame

In a diffusion combustion, the fuel and oxidizer enter combustion chamber separately before they mix and burn during continuous inter-diffusion. The combustion occurs at the interface between the fuel and the oxidizer. The structure of a diffusion flame is shown in Fig 4.3(b). In diffusion flames, the simple, measurable parameters, like the rate of burning and the flame velocity in premixed flames, can not be easily defined. The burning in a diffusion flame depends more on rate of mixing than on the rates of chemical processes involved. The rate of reaction is directly related to the amounts of fuel and oxidant diffusing into the reaction zone.

## 4.3 Combustion Models

There are several turbulent combustion models for the premixed and the diffusion flames. For the premixed flames, there are Bray-Moss-Libby Model and Coherent Flame Model which assume the infinitely fast chemistry; there is the flamelet model based on G-equation with finite rate chemistry assumption. For diffusion flames, there are conserved scalar equilibrium model (with infinitely fast chemistry assumption), the flamelet model base on mixture fraction and conditional moment closure model (with finite rate chemistry assumption). The PDF Transport Equation model and the linear Eddy Model work for both diffusion flame and premixed flame. We will discuss the flamelet model for diffusion flames in detail. The description of other models can be found in [51].

William [68] saw the turbulent diffusion flames as an combination of stretched laminar flamelet. Peter [50] derived the flamelet equation Eq. (4.10) for the diffusion flame. The flamelet is a thin reactive-diffusion layer in the turbulence flow field [51]. The flame surface is defined as the surface of stoichiometric mixture where [51]:

$$Z(x,t) = Z_{st} \tag{4.9}$$

Here Z is the mixture fraction. The flamelet equation describe the reactive-diffusive structure at the vicinity of the flame surface. It assumes the mass fraction and temperature can be expressed as a function

of the mixture fraction Z. The governing flamelet equation is:

$$\rho\frac{\partial\psi}{\partial t} = \frac{\rho}{Le}\frac{\chi}{2}\frac{\partial^2\psi}{\partial Z^2} + \omega \tag{4.10}$$

where $\psi$ is the "reactive scaler" [51] which could be the mass fraction of each chemical species or the temperature. If $\psi$ stands for the mass fraction of species $i$, $D$ is the mass diffusivity of the species $i$, $Le$ is the Lewis number $Le_i = \lambda/(\rho c_p D_i) = D/D_i$, and $\omega$ is the chemical production rate. If $\psi$ represent the temperature, $D$ is the thermal diffusivity, $Le$ is 1 and $\omega$ is the heat release rate in chemical reactions. $\chi$ is the scaler dissipation rate defined by

$$\chi = 2D|\bigtriangledown Z|^2 \ . \tag{4.11}$$

The scalar dissipation rate is a very important parameter is diffusion flames. It controls the mixing and determines the reaction rates.

The flamelet equation for mass fraction is derived from the scalar transport equation (of species $k$)

$$\rho\frac{\partial Y_k}{\partial t} + \rho u_i\frac{\partial Y_k}{\partial x_i} - \frac{\partial}{\partial x_i}\left(\rho D\frac{\partial Y_k}{\partial x_i}\right) = \omega_k \tag{4.12}$$

and scalar transport equation for mass fraction $Z$

$$\rho\frac{\partial Z}{\partial t} + \rho u_i\frac{\partial Z}{\partial x_i} - \frac{\partial}{\partial x_i}\left(\rho D\frac{\partial Z}{\partial x_i}\right) = 0 \ . \tag{4.13}$$

Assume $x_i$ is a locally orthogonal coordinate system attached to the flame surface. $x_1$ is normal to the flame surface and $x_2$ and $x_3$ are parallel to the surface. Now replace the coordinate $x_i$ with the mixture fraction $Z$ and $x_2$ and $x_3$ by $Z_2 = x_2$, $Z_3 = x_3$ and $t = \tau$. The coordinate $Z$ is normal to the flame surface by the definition of flame surface. After transformation of the coordinates , Eq. (4.12) is converted to

$$\rho\left(\frac{\partial Y_k}{\partial \tau} + u_2\frac{\partial Y_k}{\partial Z_2} + u_3\frac{\partial Y_k}{\partial Z_3}\right) - \frac{\partial(\rho D)}{\partial x_2}\frac{\partial Y_k}{\partial Z_2} - \frac{\partial(\rho D)}{\partial x_3}\frac{\partial Y_k}{\partial Z_3}$$

$$-\rho D\left[\left(\frac{\partial Z}{\partial x_i}\right)^2\frac{\partial^2 Y_k}{\partial Z^2} + 2\frac{\partial Z}{\partial x_2}\frac{\partial^2 Y_k}{\partial Z \partial Z2} + 2\frac{\partial Z}{\partial x_3}\frac{\partial^2 Y_k}{\partial Z \partial Z3} + \frac{\partial^2 Y_k}{\partial Z_2^2} + \frac{\partial^2 Y_k}{\partial Z_2^3}\right] = \omega_k \tag{4.14}$$

The flamelet model assumes the flame is thin in Z direction, the mass fraction derivative in the flame surface normal direction is much larger than in the flame surface tangential direction. By an order-of-magnitude analysis it can be found that the second derivative of Z and the time derivative are the dominant term on the left side of Eq. (4.14). Other terms can be neglected. Then Eq. (4.10) for mass fraction of species is obtained. The flamelet equation for temperature can be derived in similar way.

To apply the flamelet model to the simulation of turbulent flames, it assumes the "separation of scale": the chemical time scale are small and the reactions only happen in a thin layer near the flame surface. This thin layer is assumed to have a scale smaller than the turbulence scale and the structure of the reaction zone remains laminar and unaffected

by the turbulence.

One of the widely used flamelet models is the steady laminar flamelet model with a steady state flame assumption. The time derivative in Eq. (4.10) could be neglected. The governing equation of steady laminar flamelet model becomes

$$\frac{\rho}{Le}\frac{\chi}{2}\frac{\partial^2\psi}{\partial Z^2}+\omega=0 \tag{4.15}$$

The solution of the steady laminar flamelet model on Z space is a function of the dissipation rate and boundary conditions. Thus the solutions can be pre-calculated and saved in tabular form. After we solve Eq. (4.15) and have the solution of Z in the flow field, the temperature and the mass fraction of each species can be found by a table look up. No calculation is needed for chemical reactions during simulation since all information is precomputed. This greatly reduces the time spend on chemical reactions. There are also unsteady flamelet model, such as the "lagrangian flamelet model" [55] and "Eulerian flamelet Model" [54].

Larsson's simulation uses the "Flamelet/Progress-Variable" model of Pierce and Moin [52]. This model uses the reaction progress variable $C$ as the parameter instead of the scalar dissipation rate $\chi$ in the flamelet model. The progress variable can be defined as the mass fraction of one of the reactants or a sum of several reactants. Larsson [36] takes the mass fraction of $H_2O$ to be the progress variable $C$. An additional transport equation is solved for the filtered progress variable. Similar to the

flamelet model, the flamelet method uses precomputed and tabulated solutions, parameterised in terms of the mass fraction $Z$ and reaction the progress progress variable $C$ To reduce the table dimensions, the operating pressure is assumed a priori as a global constant. The mass fraction of each species $Y_i$ and the source term $w_{H_2O}$ can be computed as the function of the filtered mixture fraction $\tilde{Z}$, the sub filter variance $\tilde{Z}''Z''$ and the filtered $\tilde{C}$:

$$\tilde{Y}_i = \tilde{Y}_i(\tilde{Z}, \widetilde{Z''Z''}, \tilde{C}) \ , \tilde{w}_{H2O} = \tilde{w}_{H2O}(\tilde{Z}, \widetilde{Z''Z''}, \tilde{C}) \ , \tag{4.16}$$

The filtered mixture fraction $\tilde{Z}$, the sub-filter variance $\widetilde{Z''Z''}$ and the filtered $\tilde{C}$ are calculated by the LES transport equations.

In Sec. 1.1 we know that in the our model scramjet combustor simulation with high Reynolds number, the Kolmogorov scale (about 10 microns) is smaller than the flame width, so that the scale separation assumption is not satisfied. The turbulence eddies might penetrate and wrinkle the flame front and destroy the laminar flamelet structure. Thus the locally one-dimension structure and might not be a good approximation of the flames in the scramjet combustion chamber.

Instead, we use a straight-forward approach to simulate the turbulent combustion in our model scramjet combustor simulation: we solve the scalar transport equation for all species for the mass fraction of each species. The chemical production rates are calculated by reaction rates of each chemical reactions directly. At each time step, a system of ODEs

based on the reacting species are solved for the change of mass fraction of each species from chemical reactions:

$$\frac{d\rho Y_k}{dt} = \omega_i = M_k \sum_{j=1}^{n} \nu_{kj} r_j \tag{4.17}$$

We refer to our approach as the "finite rate chemistry approach" in other parts of the thesis. The difference between our finite rate chemistry model and flamelet model is: we plan to resolve the chemical reaction rather than model it.

Our finite rate chemistry model is computationally more expensive than the flamelet model. Since we need to solve systems of ODEs at each time step for every single grid cell. When we use the detailed mechanism, the system of ODEs might include stiff equations. To reduce the computational cost of this approach, a reduced chemistry mechanism is preferred to a detailed chemistry mechanism. We refer to our approach as the "finite rate chemistry approach" in other parts of the thesis.

## 4.4 One Dimensional Laminar Flame Study with Finite Rate Chemistry Model

In this section we apply the finite rate chemistry model to the simulation of one dimensional premixed and the diffusion flames. The purpose of the chapter is to analyze the grid sensitivity of the finite rate chemistry model in resolving the one dimensional flames, to give guidance to the mesh resolution required for three dimensional scramjet simulation.

We considered two $H_2/O_2$ reaction mechanisms: the detailed mechanism [28] and the reduced mechanism [8] are considered here. We predict resolution requirements for these two mechanisms. We also considered the thickened flame model.

### 4.4.1 Simulation Configuration

We consider a long tube at a constant pressure. The initial conditions of 1D study is in consistent with the 3D scramjet simulation configuration. For the premixed flame, $H_2$ and $O_2$ are mixed uniformly in a stoichiometric ratio initially.

For the diffusion flame, $H_2$ is to the left, $O_2$ to the right. $O_2$ has a temperature of 1500 K, higher than the $H_2$ flash point.

The hydro part of the 1D simulation are solved use the WENO scheme described in Sec. 2.4. The molecular diffusion coefficients are computed dynamically with the formula's in Sec. 2.2.3. Two $H_2/O_2$ reaction mech-

anisms: the detailed mechanism [28] and the reduced mechanism [8] are used separately to calculate chemistry source terms.

We try to estimate the mesh requirements for our finite rate chemistry model to resolve the diffusion and premixed flames. Here, a flame is considered to be resolved when certain measured parameter (indicator) of the flame is preserved and is insensitive to changes in grid size. The laminar flame speed are considered to be the indicator of premixed flames. The diffusion flame lacks such a simple, measurable parameter as flame speed. We use the total heat release within 0.12 ms (one flow through in 3D scramjet simulation) as the indicator.

### 4.4.2 Convergence of Premixed Flame

In the numerical experiment, initially we ignite the left end of the tube to generate a flame transverses from left end to the right end in the one dimensional tube with $H_2/O_2$ premixed.

We conduct several numerical simulations of different grid resolution, the grid size ranges from 0.0625 mm to 1 mm.

The convergence of the flame speed is shown in Fig. 4.4. To achieve an error of less than 10%, we need a grid size of 0.0625 mm for the detailed chemistry mechanism and 0.125 mm for the reduced chemistry mechanism.

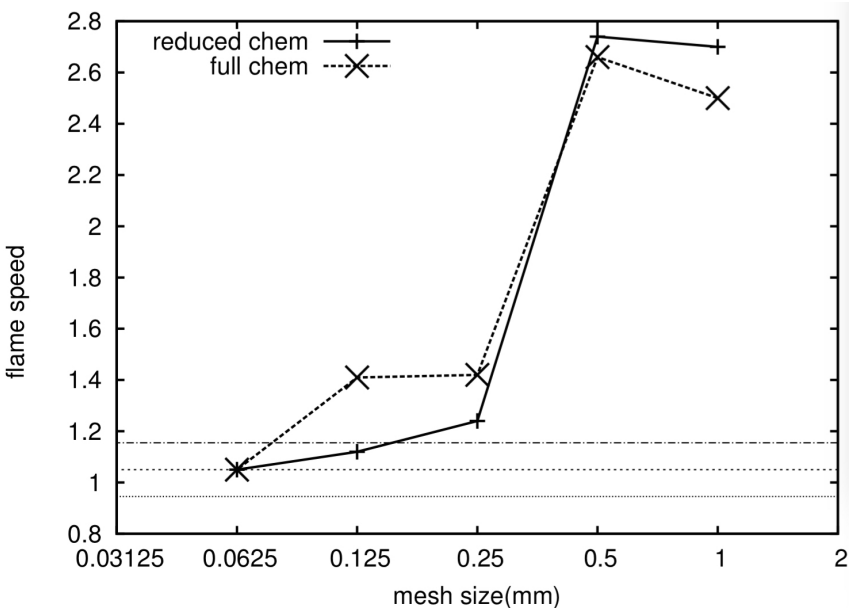


Figure 4.4: Convergence of the flame speed of a premixed flame as a function of the grid resolution. The horizontal lines indicate the fine grid flame speed and a variation of $\pm 10\%$ about this value. The unit of the flame speed is 10 m/s.

### 4.4.3 Convergence of Diffusion Flame

In the numerical experiment, The flame begins as the $H_2/O_2$ is mixed by molecular diffusion in the middle of the tube. The speed of the diffusion flame depends on the diffusion. The width of a diffusion flame is generally thicker than the width of a premixed flame. Thus the grid resolution required to resolve a diffusion is less restrictive than the premixed flame.

We conduct several numerical simulations of different grid resolution, the grid size ranges from 0.0625 mm to 1 mm. The convergence of total energy release is shown in Fig. 4.5. To achieve an error of less than 10%, we need a grid size of approximately 0.1 mm for the detailed chemistry mechanism and approximately 0.5 mm for the reduced chemistry mechanism.

The heat release rate for a diffusion flame depends on the diffusivity. The convergence of heat release rate over grid is also diffusivity correlated. In 2D and 3D simulations, turbulent mixing will speed up the mixing process of $H_2/O_2$ together with molecular diffusion. We compute the average ratio of the turbulent transport coefficient with the molecular transport coefficient in Sec. 4.5.4 and Sec. 5.2. Then we replace the molecular transport coefficient in the 1D diffusion flames with the total transport coefficient (sum of molecular and turbulent transport coefficients). The convergence of heat release rates within 1 flow through under different grid resolutions are re-examined. Minimal mesh requirements to achieve an error of less than 10% of the heat release within 1

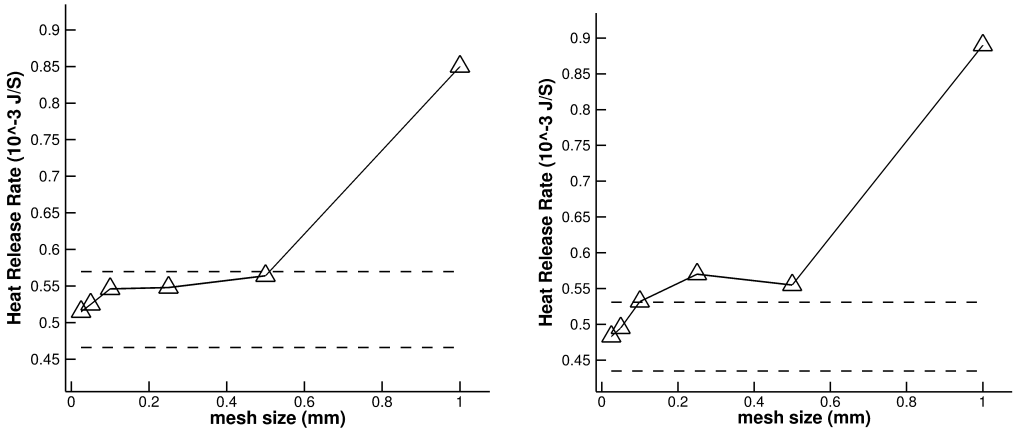


(a) The reduced chemistry mechanism. (b) The detailed chemistry mechanism.

Figure 4.5: Convergence of the heat release rate of a diffusion flame as a function of the grid resolution. Horizontal lines indicate the energy release of the fine grid flame and a ±10% variation about this value.

flow through, for different mechanisms and flow regimes are summarised in Table 4.2.

### 4.4.4 Thickened Flame Model

The thickened flame model [11] thicken the flame front artificially to allow numerical solution of the flame front on a coarser grid. The thickened flame model solves a modified problem, with modified diffusion parameters and reaction rate parameters:

$$D \to TF \times D \quad k \to TF \times k \quad \mu \to TF \times \mu \quad A \to \frac{A}{TF} \quad E \to \frac{E}{TF} \tag{4.18}$$

Here $TF$ is the flame thickening parameter.

Ying [72] has applied the thickened flame model to the simulation of one dimensional hydrogen-oxygen premixed flame. The hydrogen-oxygen premixed flame has a very thin flame front, in the order between $10^{-2}$ cm and $10^{-1}$ cm [72]. If $N$ cells ($N > 3$) lines in the flame width is needed to resolve the flame, the mesh size should be in order of $10^{-3}$ cm. Thus resolving the premixed flame requires very fine grid resolution. After the thickened flame model is applied the the premixed flame, a lower resolution requirement by a factor of eight is obtained, in the case of a thickening factor of 10 [72]. Thus the thickened flame model is very useful in the simulation of premixed flame.

When it comes to the diffusion flames, the thickened flame model delays the ignition time. We conduct 1D diffusion flame simulation with different thickening factor. The heat release rate in these simulations are shown in Fig 4.6. We can observe this ignition delay in Fig 4.6.

In the context of our motivating simulation problem, the flow in the scramjet combustion chamber is supersonic and the residence time of the combustible fuel in the combustion chamber is limited to 12 $ms$. We find that even a modest level of flame thickening (TF = 2), with the associated ignition delay, reduces the overall heat release. Thus this method is not effective. The thickened flame model is excluded form the model lists of 3D scramjet simulation.

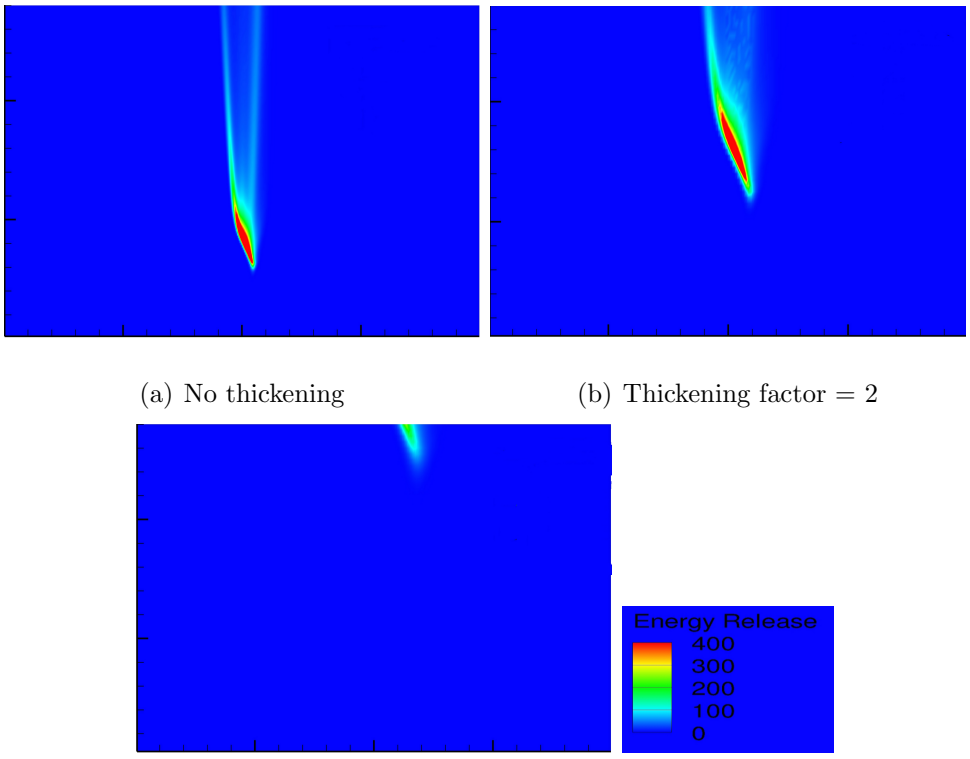


(a) No thickening (b) Thickening factor = 2

(c) Thickening factor = 4 (d)

Figure 4.6: Heat-release rate in diffusion flame by different thickening factors. The x and y axis represent space and time.

### 4.4.5 Conclusion

We have explored both the detailed and the reduced chemistry mechanisms. We find that reduced mechanism requires less stringent grid resolution, by a factor of about 2 to 4 in comparison with the detailed chemistry mechanism. The thickened flame model is excluded since it lead to ignition delay.

## 4.5 Two dimensional Turbulent Flame Study with Finite Rate Chemistry Model

The 2D simulation is more complex than the 1D ones: it contains turbulence, shock waves and boundary layers besides the 1D phenomena of molecular mixing and combustion.

On one hand, turbulence speeds up chemical reactions. The turbulent flow contains a wide range of eddies of different length scales. These eddies increases the mixing process the fuel and oxidizer, allowing the chemical reaction to start. On the other hand, combustion releases heat and generate flow instability by buoyancy and gas expansion, which in turn enhances the turbulence.

In this section, we will study the mesh convergence of LES with finite rate chemistry model in the two-dimensional turbulent reactive flow simulation, and to understand turbulent diffusion, which is also important in the three-dimensional simulation.

### 4.5.1 Simulation Configuration

We choose our 2D simulation as an XZ plane cut from the model scramjet combustor.

The inflow turbulence is generated by a synthetic turbulent generator of Touber [65]. The turbulent intensity is 2.3% and the length scale of the randomised turbulence is about 10 mm. The inflow $O_2$ has an average density of $1.241\times10^{-4}$ kg/m$^3$, velocity of 1890 m/s and temperature of 1276 K. The inflow $H_2$ has a density of $4.2 \times 10^{-4}$ kg/m$^3$, velocity of 615 m/s and a temperature of 300 K.

The grids for our convergence study are defined by Table 4.3.

### 4.5.2 Energy Spectrum Analysis

The dynamic choice of parameters for the SGS construction compares two resolved grid levels, the current grid and a coarser one, the test filter. We assume an asymptotic (power law) behaviour for the dynamic coefficient and then the information taken from these two grid levels is sufficient to predict the unknown coefficient needed to model the sub-grid terms describing the solution at a still smaller grid level. Thus the fundamental requirement for LES is that the computational grid cutoff lies in a scaling region. 2D turbulence has a further complication with two different scaling regions and an inverse cascade, those above and below the length scale of the perturbation driving the turbulence. From

the above analysis, we take as a convergence requirement that the grid cutoff must lie within one of these two scaling ranges.

According to Kolmogorov's hypothesis, fully developed turbulence has three length scales ranges: the dissipation range, the inertial subrange and the energy-containing range [57]. The inertial subrange is a universally equilibrium range, with an energy spectrum of $E(\kappa) = C\epsilon^{2/3}\kappa^{-5/3}$. Beyond the classical $k^{-5/3}$ Kolmogorov scaling, a variety of other exponents have been reported in a variety of contexts. Specifically to the point here is the 2D nature of scaling exponents [34, 7], with a classical theory predicting two scaling ranges, $k^{-5/3}$ for the smaller $k$ values and $k^{-3}$ for larger $k$ values. The transition between the two ranges is the largest $k$ value in the turbulence driver or initial conditions.

Fig. 4.7 displays the temporal turbulent kinetic energy (TKE) spectrum as a function of frequency $k$ for several meshes. The data comes from a probe located in the down stream of model scramjet combustor chamber. We draw three conclusions from this figure. First, we observe an approximate $k^{-5/3}$ and $k^{-3}$ slopes as expected. We interpret this fact as showing that the flow is well resolved. Second, the turbulent kinetic spectra of grid IV agrees quite well with the turbulent kinetic energy spectra of grid III. Thirdly, the inertial range, with a slope of $k^{-5/3}$, starts at a frequency of $2.0 \times 10^5$ Hz. Considering that the average flow speed is 1500 m/s at the probing point, the grid levels I, III and IV correspond to frequencies of $1.8 \times 10^6$ Hz, $3.6 \times 10^6$ Hz and $7.2 \times 10^6$ Hz respectively; the filter sizes of grid levels I, III and IV correspond to

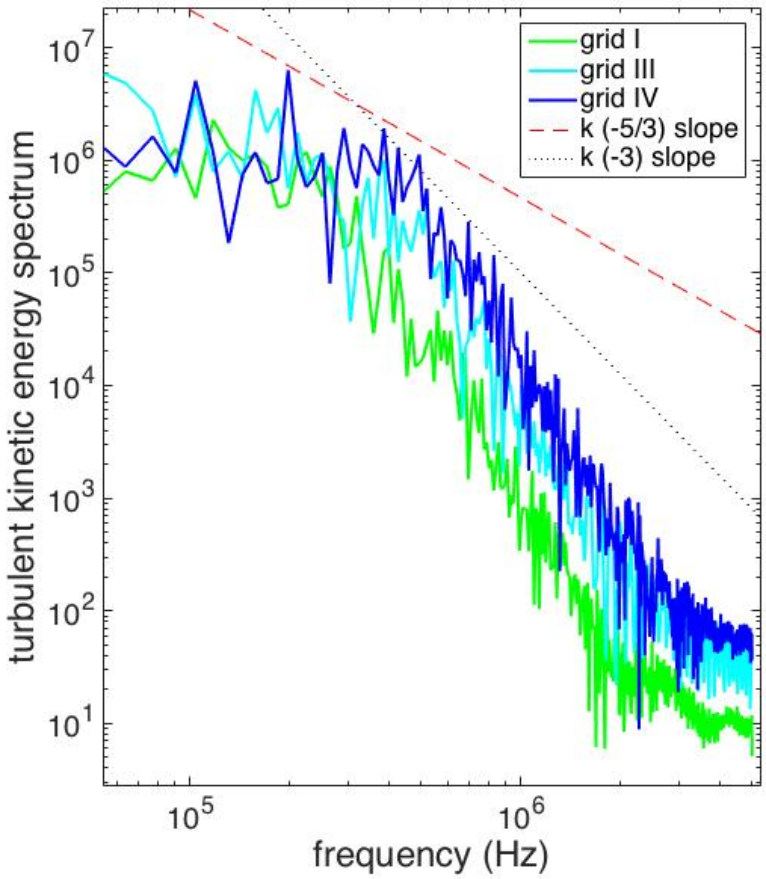


Figure 4.7: Temporal turbulent kinetic energy (TKE) spectra, with several grid sizes, at a down steam location in the chamber. The red doted line shows the $k^{-5/3}$ slope and the black dashed line shows the $k^{-3}$ slope.

half of these frequencies. All of these values are strictly within the second scaling region, meaning that the SGS requirement for a grid cutoff within a scaling region is satisfied.

### 4.5.3 Resolved Fraction of Turbulent Kinetic Energy

Pope [57] introduced a measurement of the turbulent resolution as the comparison of the resolved turbulent kinetic energy to the modeled kinetic energy. The resolved turbulent kinetic energy is

$$k_{res} = 0.5\langle(\tilde{u}_i - \langle\tilde{u}_i\rangle)(\tilde{u}_i - \langle\tilde{u}_i\rangle)\rangle \ . \tag{4.19}$$

The modeled turbulent kinetic energy is estimated as

$$k_{SGS} = \frac{\nu_{SGS}^2}{C_S^2\Delta^2} \tag{4.20}$$

where $\nu_{SGS}$ is the turbulent viscosity in the dynamic SGS model [9]. The ratio $M = k_{SGS}/(k_{SGS} + k_{res})$ of modeled TKE to total TKE is used to measure how much turbulent kinetic energy is modeled by the LES grid, with smaller values, corresponding to more of the turbulence resolved rather than modeled. The spatial distribution of $M$ values for different grids is displayed in Fig. 4.8.

In the interior of the chamber, we see an increase in the resolved turbulent kinetic energy. As we refine the grid, we see the higher $M$ values confined

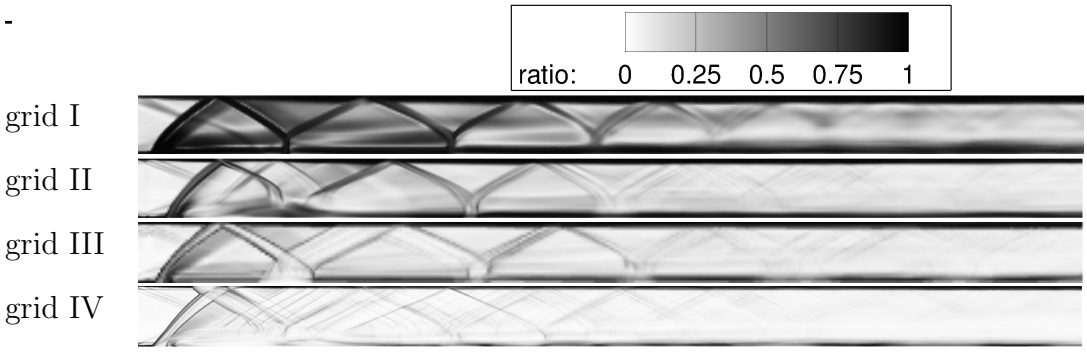


Figure 4.8: The ratio of modeled to total turbulent kinetic energy in the combustion chamber

to the boundary and inlet regions. Thus the turbulence is well resolved at grids II, III and IV [57].

### 4.5.4 Turbulent Diffusion

Turbulent diffusion plays an important role in modelling thermal diffusion and the mixing of reactants at a sub-grid level. Table 4.4 shows the percentage of turbulent diffusion coefficient as a fraction of the total diffusion coefficient. Here the turbulent diffusion coefficient are computed by dynamical Smagorinksy model through Eq (2.57), (2.62) and (2.61); the molecular diffusion coefficient are computed dynamically as in Sec. 2.2.3. These values are averaged over the shear layer within one scramjet residence time. We observe that the percentage of the turbulent diffusion decreases with increasing grid resolution.

In [45], a scaling law was proposed for the turbulent coefficient $D_{coef} =$

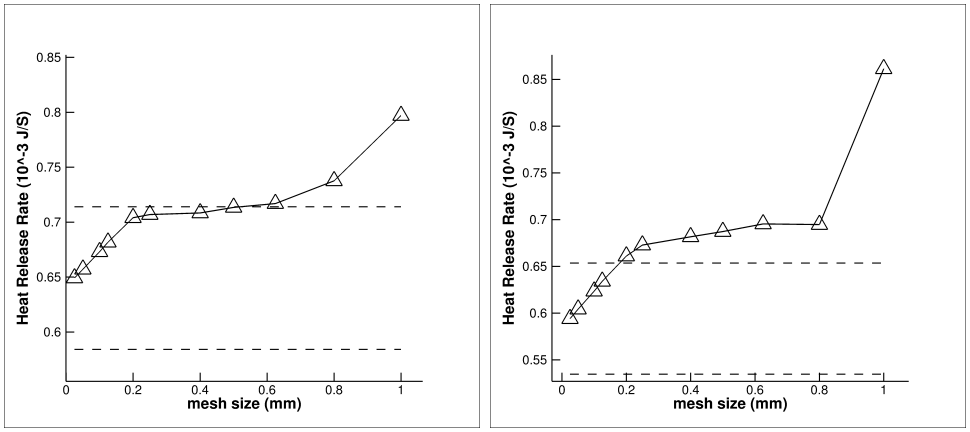


(a) The reduced chemistry mechanism. (b) The detailed chemistry mechanism.

Figure 4.9: Convergence of heat release rate of a diffusion flame as a function of the grid resolution. Horizontal dashed lines indicate the energy release of the fine grid flame and a ±10% variation about this value.

$C\Delta x^{\frac{4}{3}}$. Columns 4, 5 and 6 of Table 4.4 show the scaled mean turbulent transport coefficient. We observe only a mild dependence of the scaled coefficient on grid level, indicating that the scaling removes most of the grid dependence. We re-do the 1D convergence study of heat release of diffusion flame, with new total (molecular plus turbulent) diffusivity (based on the fraction of turbulent viscosity out of total diffusivity), see Fig. 4.9. To achieve an error of less than 10%, we need a grid size of approximately $\Delta x = 0.52$ mm for the reduced chemistry and 0.125 mm for the detailed chemistry.

### 4.5.5 Reaction Width Analysis

The width of each reaction is shown in Table 4.5, for a diffusion flame with 2D turbulent mixing. The flame thickness of reaction $i$ is defined as [69]:

$$\delta_i = \frac{\int_{-\infty}^{\infty} w_i(x)dx}{max_x\{w_i(x)\}} \tag{4.21}$$

where $w_i$ is the rate of reaction i. As the turbulent diffusion coefficient derived from the 2D simulation is mesh dependent, we also specify the mesh used to define it: 0.125 mm. We observe that reactions 1, 9, 10 and 18 have much wider reaction zones than the remaining ones.

For the present analysis, we assume that at least $N$ ($N \geq 3$) cells in the reaction zone of each reaction are needed for numerical resolution. To resolve the detailed chemistry mechanism reaction for the 2D diffusion flame, we need a resolution of 0.22 mm. To resolve the chemistry reaction using the reduced chemistry mechanism for the 2D diffusion flame, we need a resolution of 0.34 mm. Thus the reduced mechanism has a diminished resolution requirement relative to the detailed chemistry mechanism.

### 4.5.6 Grid Sensitivity of the Chemical Reactions

The reaction and turbulence can be observed from a snapshot of temperature and OH concentration in the combustion chamber, see Figs. 4.10 and 4.11. These figures show the increase in the resolved turbulence

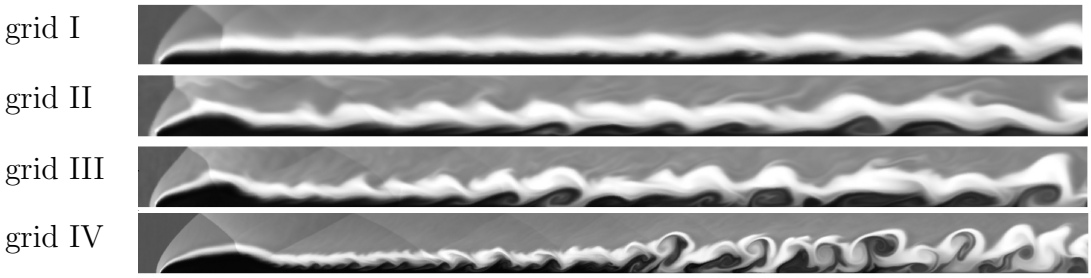


Figure 4.10: Temperature snapshot in the combustion chamber

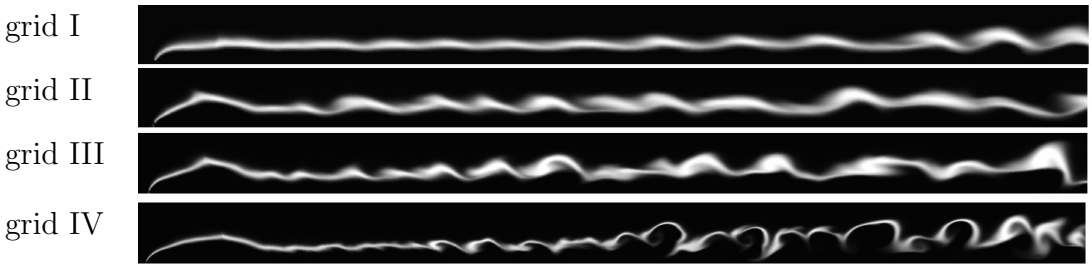


Figure 4.11: OH concentration snapshot in the combustion chamber

level as the mesh is refined. The mesh convergence is measured by two parameters: the total energy released from the chemical reactions in the combustion chamber and the percentage of H atoms that burn into $H_2O$ [38] at the outlet of combustion chamber. The energy release and percentage of H are averaged over scramjet residence time for each grid, see Table 4.6.

With an acceptance discrepancy level set to 10%, the results indicate that the combustion has reached grid-convergence at grid III.

Table 4.1: Reaction Mechanism of Hong [28].

| Reaction |
|---|
| Hydrogen-oxygen chain |
| 1. $H+O_2 \rightleftharpoons O+OH$ |
| 8. $OH+OH \rightleftharpoons H_2O+O$ |
| 9. $O+H_2 \rightleftharpoons H+OH$ |
| 10. $OH+H_2 \rightleftharpoons H+H_2O$ |
| Direct recombination |
| 18.$H_2+M \rightleftharpoons H+H+M$ |
| $H_2+H_2 \rightleftharpoons H+H+H_2$ |
| $H_2+O_2 \rightleftharpoons H+H+O_2$ |
| 7. $H_2O+M \rightleftharpoons H+OH+M$ |
| $H_2O+H_2O \rightleftharpoons OH+H+H_2O$ |
| 19. $O+O+M \rightleftharpoons O_2+M$ |
| 20. $O+H+M \rightleftharpoons OH+M$ |
| Hydroperoxyl reactions |
| 2. $H+O_2(+M) \rightleftharpoons HO_2(+M)$ |
| $H+O_2(+O_2) \rightleftharpoons HO_2(+O_2)$ |
| $H+O_2(+H_2O) \rightleftharpoons HO_2(+H_2O)$ |
| 11. $H+HO_2 \rightleftharpoons OH+OH$ |
| 12. $H+HO_2 \rightleftharpoons H_2O+O$ |
| 13. $H+HO_2 \rightleftharpoons H_2+O_2$ |
| 14. $O+HO_2 \rightleftharpoons OH+O_2$ |
| 15. $H_2O_2+H \rightleftharpoons HO_2+H_2$ |
| Hydrogen peroxide reaction |
| 3. $H_2O_2(+M) \rightleftharpoons 2OH(+M)$ |
| 4. $OH+H_2O_2 \rightleftharpoons HO_2+H_2O$ |
| $OH+H_2O_2 \rightleftharpoons HO_2+H_2O$ |
| 6. $2HO_2 \rightleftharpoons O_2+H_2O_2$ |
| 16. $H_2O_2+H \rightleftharpoons H_2O+OH$ |
| 17. $H_2O_2+O \rightleftharpoons OH+HO_2$ |

Table 4.2: Summary of minimal mesh requirements for reduced and full chemistry, based on 1D flame analysis, but with laminar or 2D or 3D turbulent diffusivity.

| Flow Regime | Full Chemistry | Reduced Chemistry |
|---|---|---|
| 1D laminar flame analysis | 0.1 mm | 0.5 mm |
| 1D flame analysis; 2D turbulent diffusivity | 0.125 mm | 0.52 mm |
| 1D flame analysis; 3D turbulent diffusivity | 0.25 mm | 0.625 mm |

Table 4.3: Grid resolution

| | x $(mm)$ | y $(mm)$ |
|---|---|---|
| Grid I | 0.5 | 0.5 |
| Grid II | 0.5 | 0.25 |
| Grid III | 0.25 | 0.25 |
| Grid IV | 0.125 | 0.125 |

Table 4.4: Turbulent diffusion as a fraction of the total diffusion coefficient. The last three column show scaled values of these quantities to remove the leading order $\Delta x$ effect.

| | turbulent dynamic viscosity fraction | turbulent thermal conductivity fraction | turbulent species (OH) diffusivity fraction | scaled dynamic viscosity coefficient | scaled thermal conductivity coefficient | scaled species (OH) diffusivity coefficient |
|---|---|---|---|---|---|---|
| Grid I | 0.90 | 0.75 | 0.73 | 0.0000360 | 0.00193 | 0.149 |
| Grid II | 0.28 | 0.62 | 0.58 | 0.0000359 | 0.00199 | 0.187 |
| Grid III | 0.26 | 0.40 | 0.57 | 0.0000326 | 0.00203 | 0.184 |
| Grid IV | 0.16 | 0.21 | 0.29 | 0.0000410 | 0.00200 | 0.142 |

Table 4.5: Reaction widths for the detailed chemistry mechanism in 2D diffusion flames.

| No | Reaction | flame width (mm) |
|---|---|---|
| 1 | $H+O_2 \rightleftharpoons O+OH$ | 1.147 |
| 2 | $H+O_2(+M) \rightleftharpoons HO_2(+M)$ | 1.613 |
| | $H+O_2(+O_2) \rightleftharpoons HO_2(+O_2)$ | 1.378 |
| | $H+O_2(+H_2O) \rightleftharpoons HO_2(+H_2O)$ | 1.505 |
| 3 | $H_2O_2(+M) \rightleftharpoons 2OH(+M)$ | 0.862 |
| 4 | $OH+H_2O_2 \rightleftharpoons HO_2+H_2O$ | 1.258 |
| | $OH+H_2O_2 \rightleftharpoons HO_2+H_2O$ | 1.359 |
| 5 | $OH+HO_2 \rightleftharpoons H_2O+O_2$ | 1.467 |
| 6 | $2HO_2 \rightleftharpoons O_2+H_2O_2$ | 0.667 |
| | $2HO_2 \rightleftharpoons O_2+H_2O_2$ | 0.890 |
| 7 | $H_2O+M \rightleftharpoons H+OH+M$ | 1.625 |
| | $H_2O+H_2O \rightleftharpoons OH+H+H_2O$ | 1.250 |
| 8 | $OH+OH \rightleftharpoons H_2O+O$ | 1.219 |
| 9 | $O+H_2 \rightleftharpoons H+OH$ | 1.100 |
| | $O+H_2 \rightleftharpoons H+OH$ | 1.013 |
| 10 | $OH+H_2 \rightleftharpoons H+H_2O$ | 1.096 |
| 11 | $H+HO_2 \rightleftharpoons OH+OH$ | 1.440 |
| 12 | $H+HO_2 \rightleftharpoons H_2O+O$ | 1.445 |
| 13 | $H+HO_2 \rightleftharpoons H_2+O_2$ | 1.345 |
| 14 | $O+HO_2 \rightleftharpoons OH+O_2$ | 1.417 |
| 15 | $H_2O_2+H \rightleftharpoons HO_2+H_2$ | 0.959 |
| 16 | $H_2O_2+H \rightleftharpoons H_2O+OH$ | 1.054 |
| 17 | $H_2O_2+O \rightleftharpoons OH+HO_2$ | 1.313 |
| 18 | $H_2+M \rightleftharpoons H+H+M$ | 1.325 |
| | $H_2+H_2 \rightleftharpoons H+H+H_2$ | 1.373 |
| | $H_2+O_2 \rightleftharpoons H+H+O_2$ | 1.259 |
| 19 | $O+O+M \rightleftharpoons O_2+M$ | 1.319 |
| 20 | $O+H+M \rightleftharpoons OH+M$ | 1.240 |

Table 4.6: Mesh convergence of 2D simulations

| | energy release of reduced chem (J/s) | energy release of detailed chem (J/s) | percentage of H atoms in $H_2O$ in reduced chem | percentage of H atoms in $H_2O$ in detailed chem |
|---|---|---|---|---|
| grid I | 1.036 | 1.106 | 21.9 % | 22.3% |
| grid II | 1.392 | 1.304 | 32.23% | 31.45% |
| grid III | 1.640 | 1.541 | 36.9% | 34.4% |
| grid IV | 1.775 | 1.686 | 41.0 % | 40.2% |

# Chapter 5

# Scramjet 3D Simulation

In Chap. 3 we assess the convergence of the averaged value of wall shear stress and shear flux under 1D context and predict the resolution requirement to achieve grid convergence within 10% error ratio is 0.25 mm. In Sec. 4.4 and Sec 4.5 we made predictions regarding mesh resolutions needed to resolve turbulent combustion to be 0.5 mm. We apply the predicted grid to the simulation of 3D scramjet model scramjet.

We present a 3D finite rate chemistry simulation with a mesh resolution of $[\Delta x, \Delta y, \Delta z]$= [0.5 mm, 0.25 mm, 0.25 mm] for this claim. This simulation compared with a independent simulation by Stanford PSAAP Center on the same problem, and they are compared to experiment results. The comparisons appear to be satisfactory.

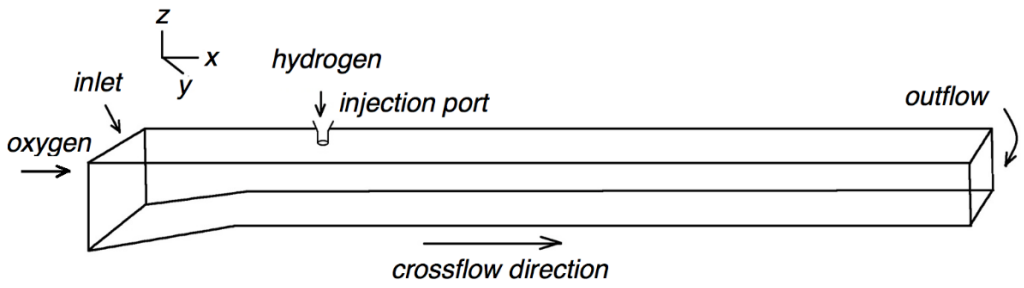


Figure 5.1: Sketch of the model scramjet combustion chamber (Image source [72]).

## 5.1 Model Configuration

The scramjet model model combustor (see Fig. 5.1) [21] studied here is designed to be geometrically simple while representative of realistic scramjet combustion conditions in Mach 5-8 flight conditions. The experiment setup is defined in detail in [21].

The model scramjet combustor has an angled intake ramp followed by a rectangular combustor section 75 mm wide, 15 mm high, and 315.4 mm long. Fuel is injected through a single injector on the center-line which is $D = 2$ mm in diameter. The distance of the injection port downstream from the flat plate leading edge is $L = 70$ mm. Six high-bandwidth pressure transducers are mounted in plugs inserted into the center-line of the top wall of the model combustor to allow pressure measurements [21].

The $H_2$ flows out of the nozzle vertically and is bent downstream by the cross flow $O_2$ stream. The inflowing oxygen has an initial temperature

$T_{O_2} \approx 1200$ K, pressure $P_{O_2} = 0.4$ bar and cross flow velocity $U_{O_2} \approx 1800$ m/s. Together with a kinematic viscosity of $\nu = 5.36 \times 10^{-4}$ m$^2$/s, the Reynolds number for the cross flow can be computed as $Re_{O_2} = LU/\nu = 2.35 \times 10^5$, where $L$ is the height of the $O_2$ inlet. The hydrogen is injected into the combustion chamber with a pressure $P_{H_2} = 12.5$ bar, temperature $T_{H_2} = 300$K and jet exit velocity $U_{H_2} = 1132.5$ m/s. With the kinematic viscosity $\nu = 1.6 \times 10^{-4}$ m$^2$/s, the Reynolds number $Re_{H_2} = DU/\nu = 1.4 \times 10^5$, where $D$ is the diameter of the fuel jet.

We estimate the dissipation rate $\epsilon$ as by $\epsilon = \langle u'u' \rangle^{3/2}/l$, where $l$ is the size of the most energetic turbulent eddies assumed to be a quarter of the diameter of the fuel jet. The Kolmogorov scale $\eta = (\frac{\nu^3}{\epsilon})^{1/4}$ is estimated to be approximately 10 microns.

## 5.2 3D Turbulence and Turbulent Diffusion

3D turbulence has one scaling range, in contrast to the two ranges of 2D turbulence. See Fig. 5.3, showing temporal TKE as in Fig. 4.7. Due to the change of the scaling exponent from -3 to -5/3, we expect larger turbulent diffusivity and a lower fraction of resolved turbulence. In fact the turbulent dynamic viscosity has increased from $2.4 \times 10^{-5}$ kg/m·s (2D) to $7.3 \times 10^{-5}$ kg/m·s (3D), and the fractional resolution of TKE plotted in a XZ cross section, Fig. 5.4, is to be compared to Fig. 4.8 and still shows low levels of modeled turbulence within the flame region.

The turbulent viscosity, turbulent thermal conductivity and the turbu-

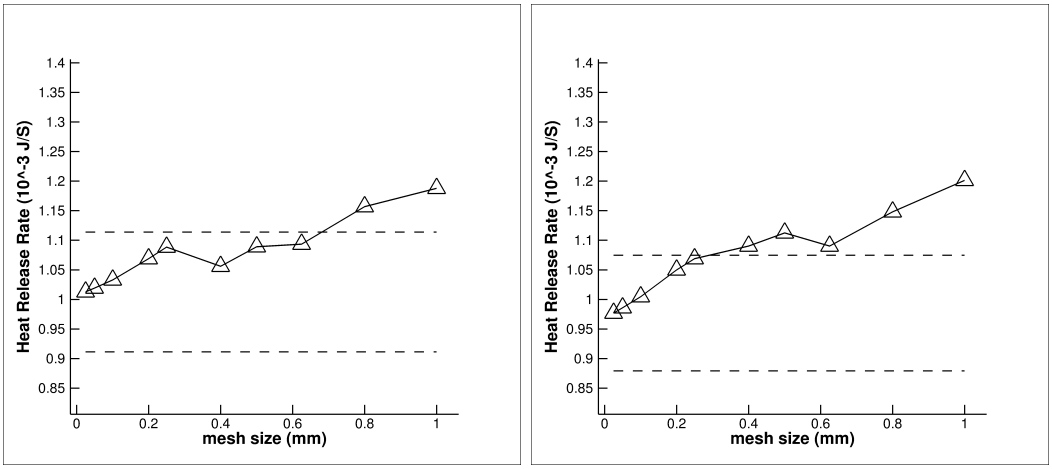


(a) The reduced chemistry mechanism. (b) The detailed chemistry mechanism.

Figure 5.2: Convergence of the heat release rate of a diffusion flame as a function of the grid resolution. Horizontal dashed lines indicate the energy release of the fine grid flame and a ±10% variation about this value.

lent species (OH) diffusivity as a fraction of the total viscosity, thermal conductivity and species (OH) diffusivity are approximately 0.65, 0.67 and 0.84 in the 3D simulation.

We re-do the 1D convergence study of heat release of diffusion flame. with a new total (molecular plus turbulent) diffusivity (i.e., assuming the same ratio between turbulent viscosity and molecular viscosity for the 1D and 3D models), see Fig. 5.2. To achieve an error of less than 10%, we need a grid size of approximately $\Delta x = 0.625$ mm for the reduced chemistry and 0.25 mm for the detailed chemistry.

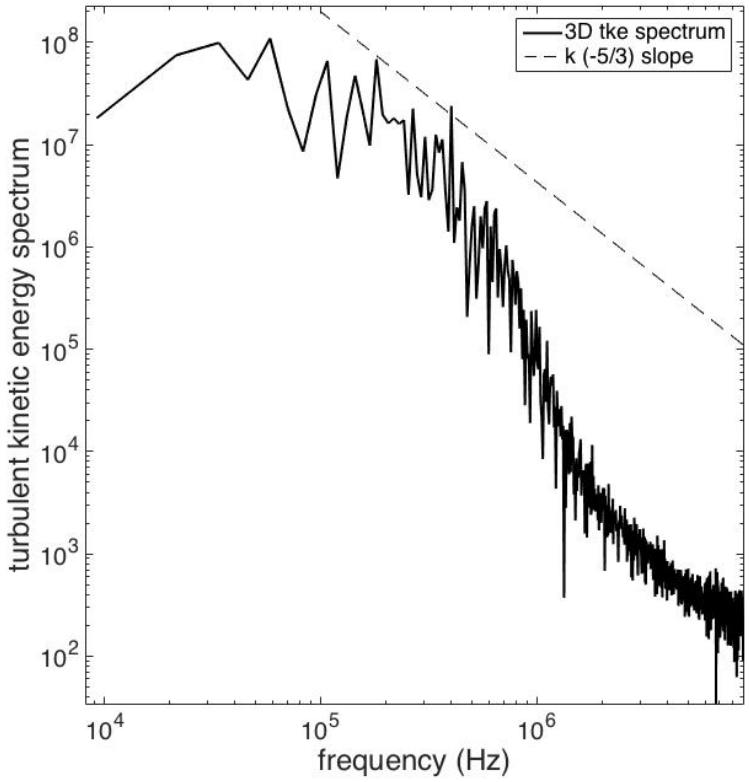


Figure 5.3: Temporal TKE spectra at a down stream location in the chamber. The doted line shows the $k^{-5/3}$ slope.


Figure 5.4: The ratio of modeled to total turbulent kinetic energy in the combustion chamber

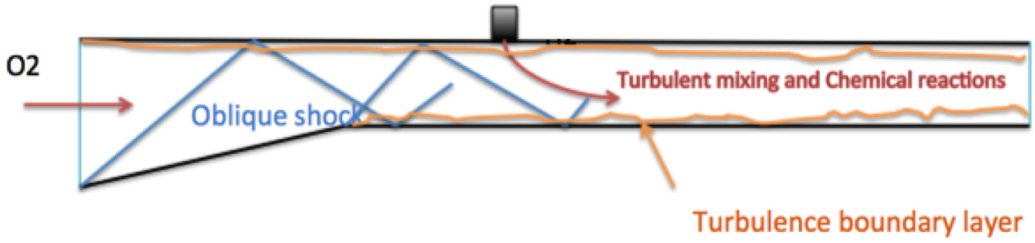


Figure 5.5: Scramjet schematic plot

## 5.3 Turbulent Boundary Layer in Model Scramjet Combustor Simulation

The schematic plot of turbulence boundary layer in the model scramjet combustor is shown in Fig. 5.5. The scramjet simulation has solid wall boundary conditions at the top, bottom, front and back walls. The Sec. 5.3 simulation has a grid resolution of ($\Delta$x, $\Delta$y, $\Delta$z) = (0.5 mm, 0.25 mm, 0.25 mm).

The velocity contour within the combustion chamber is shown in Fig. 5.6. We observe that the main stream velocity is decreasing in the combustion chamber as the flow moves to the outlet. To assess the boundary layer flow, the time averaged velocity normalised the main stream velocity within the combustion chamber is shown in Fig. 5.7.

The boundary layer thickness $\delta$ increase from inlet to the outlet. The boundary layer thickness $\delta_{95}$ at different locations on each wall are shown in Fig. 5.8. Here the boundary layer thickness in Fig. 5.8 is $\delta_{95}$, the value of wall-normal distance at which point the velocity reaches 95% of the

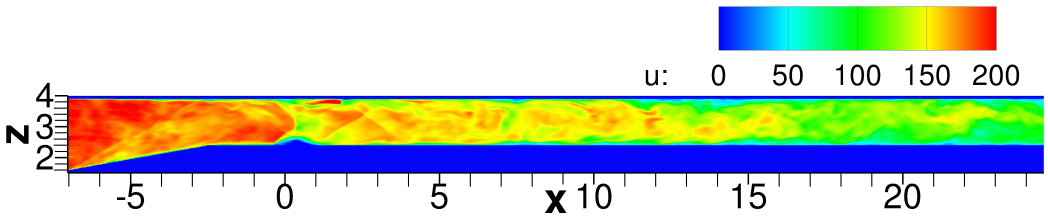


(a) xz plane (y = 1.6 cm). Side wall is located at y = ±3.75 cm

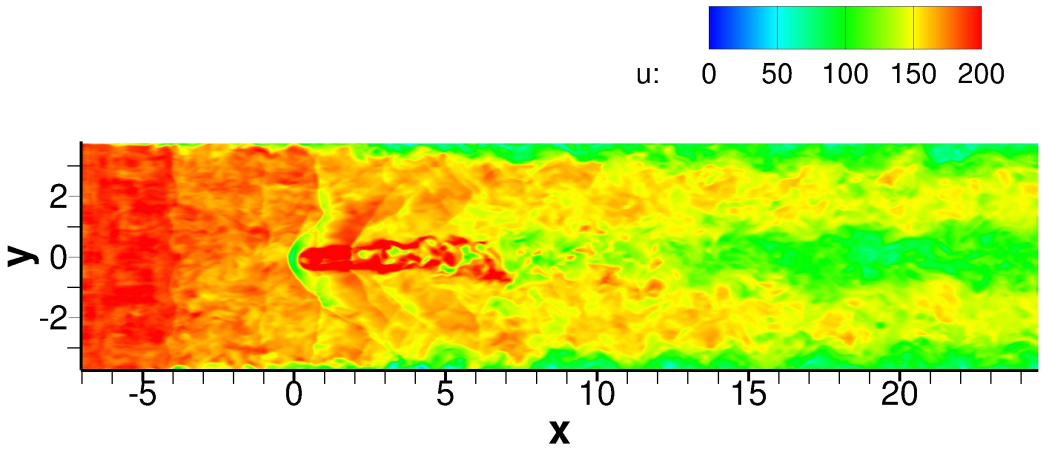


(b) xy plane. (z = 3.2 cm)

Figure 5.6: Velocity profile in the combustion chamber

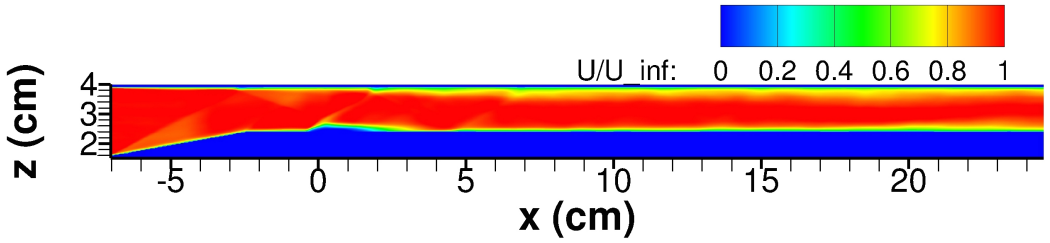


(a) xz plane.(y = 1.6 cm).

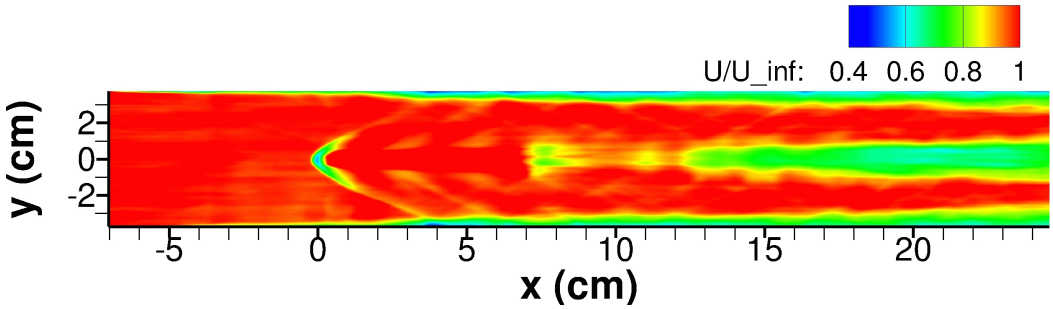


(b) xy plane. (z = 3.2 cm).

Figure 5.7: Normalised velocity in the combustion chamber. $U_{\text{inf}}$ is the main stream velocity.

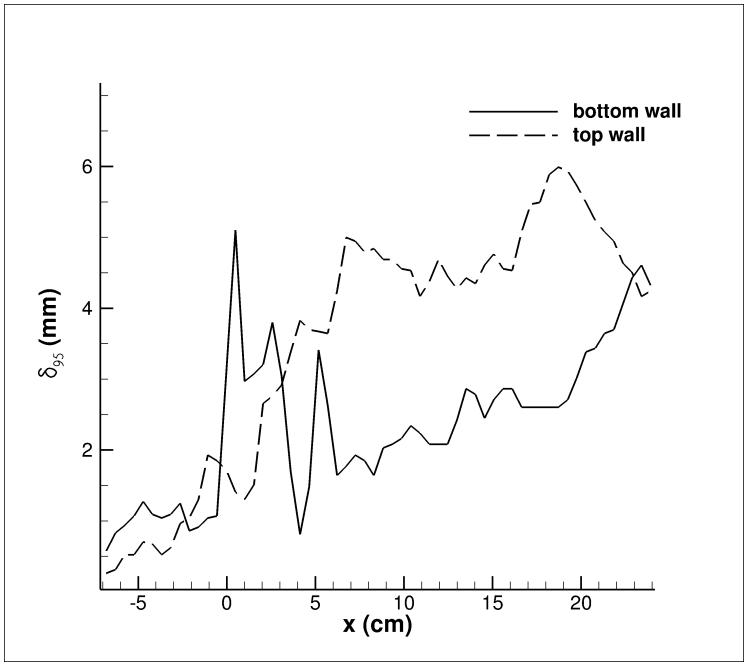


(a) Top and bottom wall.

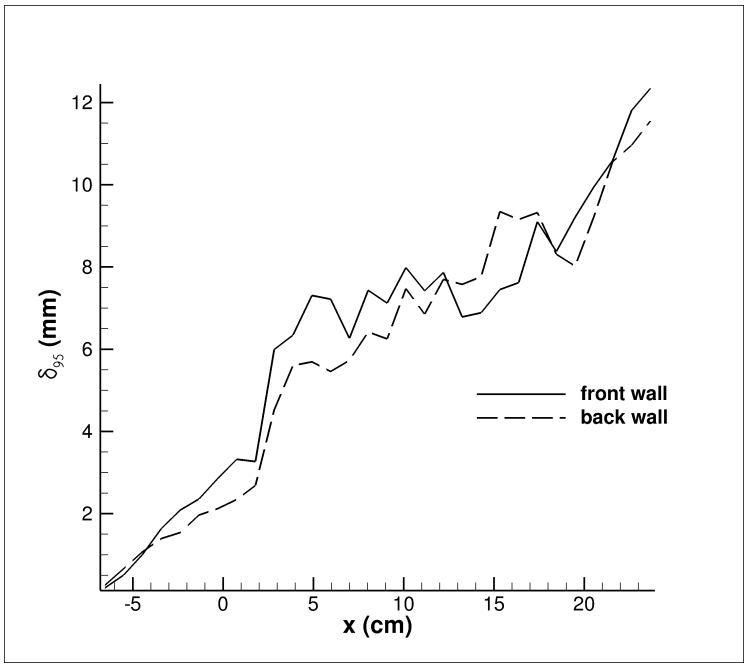


(b) Front and back wall.

Figure 5.8: Boundary layer thickness $\delta_{95}$

main stream velocity. We plot $\delta_{95}$ instead of $\delta_{99}$ because a 1% velocity difference is too small compared with the velocity fluctuations in the interior part of the turbulent chamber to be clearly observable. Near the inlet, the boundary layer at each wall has a thickness of about 1 mm; At most parts of the top wall, boundary layer thickness is about 3 mm, At most parts of the bottom wall, boundary layer thickness is about 5 mm. At most parts of the side walls, boundary layer thickness is larger than 7 mm,

Initially we use the first cell off the wall as the matching point. Based on analysis of Sec 3.5, an 20% error (at most) might occur. This potential error explains the flow blockage, and the high pressure at the outlet. To reduce this error, we might need to abandon the strategy of using the first cell off the wall as the matching point.

According to the analysis of Sec. 3.5.4, we made a better choice of the matching point. The boundary thickness shown in Fig. 5.8 means we allow another choice of the matching point. Near the inlet, we use the first point as the matching point as boundary layer thickness $\delta \approx 1$ mm. At the region $x > 3$ mm we use the interpolated state at $y = 2.5$ mm as the input to the TBL model. According to error analysis of Sec. 3.5.4, the choice could reduce the potential error in the calculation of wall shear stress and heat flux to under 10%.

| | Our Simulation | Stanford PSAAP Center Simulaiton |
|---|---|---|
| Turbulent combustion | finite rate chemistry<br>reduced mechanism | flamelet/progress-variable<br>detailed mechanism |
| | LES | |
| Subgrid turbulent stress | dynamic smargorinky model | eddy-viscosity hypothesis model of Vreman |
| Subgrid convective energy<br>and scalar flux | gradient transport hypotheses<br>with dynamic $\mathrm{Pr}_t$ and $\mathrm{Sc}_t$ | gradient transport hypotheses<br>with fixed $\mathrm{Pr}_t = \mathrm{Sc}_t = 0.5$ |
| Space discritization | uniform grid<br>11M cells | unstructured grid, locally refinement<br>54 M cells |
| Turbulence inflow | Digital filtering method | |
| Turbulent boundary layer | Equilibrium wall model | |

Table 5.1: Computational Set-Ups of our simulation and Stanford PSAAP center's simulation.

## 5.4 Comparison of Finite Rate Chemistry and Flamelet Simulations with Experiment

In this section, we compare the finite rate chemistry and flamelet simulations to each other and to the experiments [21].

### 5.4.1 The 3D Finite Rate Chemistry and Flamelet Simulation Models

Stanford PSAAP center and we conduct large eddy simulation of model scramjet combustor with different physical models, summerized by Table 5.1. We call our simulation "finite rate chemistry simulation" and Stanford PSAAP center's simulation "flamelet simulation".

The finite rate chemistry simulation uses a uniformly grid with 11 million

cells; the mesh size is $[\Delta x, \Delta y, \Delta z]$= [0.5 mm, 0.25 mm, 0.25 mm]. The flamelet model simulation uses an nonuniform grid, refinement near the boundaries and the fuel inlet, with an overall mesh of 54 million cells.

The finite rate chemistry simulation uses the reduced chemistry model discussed in Sec. 4.1, solving the scalar transport equation for all species and calculating the finite rate chemistry source terms directly. Dynamic SGS models are used to compute the turbulent diffusion coefficient in the LES transport equations. Turbulent boundary layers are from the method of [32].

The flamelet methodology, explained in Sec. 4.3, is used as the combustion model. The eddy-viscosity hypothesis model proposed by Vreman [67]. The sub-grid heat flux and species transport are modeled using the gradient transport hypotheses with fixed turbulent Prandtl and Schmidt numbers. The $H_2$ combustion mechanism coincides with the refined model referred in Sec. 4.1. Further details come from the related simulation [38].

### 5.4.2 Comparison of Pressures on Upper Wall

Fig. 5.9 shows the upper pressure, comparing the finite rate chemistry simulation, the flamelet model and experiment [21]. Time averaging of the point-wise pressure removes turbulent fluctuations and records a mean pressure value. The smoother nature of the flamelet plot is due to the use of a longer period for the time averaging.

We divide the combustion chamber into the regions A = [-2, 3] cm, B = [3, 7] cm, C = [7, 11] cm and D = [11, 23] cm. Region A and D show satisfactory agreement among the two simulations and the experiment. Region B, which is the flame ignition regime, shows satisfactory agreement between the finite rate chemistry simulation and the experiment, while the pressure of the flamelet model is too large. The early ignition of famelet model reflects a known weakness of steady flamelet models, which assume steady burning and thus are unable to predict ignition. Consistent early ignition in "Jet In Cross Flow" problem were also observed by Chan [12] when she compared the simulation result of DNS and LES with flamelet model. She attributed the early ignition to the omission of heat-transfer into the one-dimensional flame-structure in flamelet model.

The early ignition in the flamelet-model can be also be seen from a comparison of the water content in region A between the two simulations, see Fig. 5.10. Region C is the reverse, with the flamelet simulation and experiment in satisfactory agreement while the finite rate chemistry simulation has too low a pressure.

### 5.4.3 Comparison of OH Production

We compare the OH concentration with the OH PLIF (Planar Laser-Induced Fluorescence) plots from experiment at several end-view planes from the finite rate chemistry simulation, see Figs. 5.11 and 5.12. The

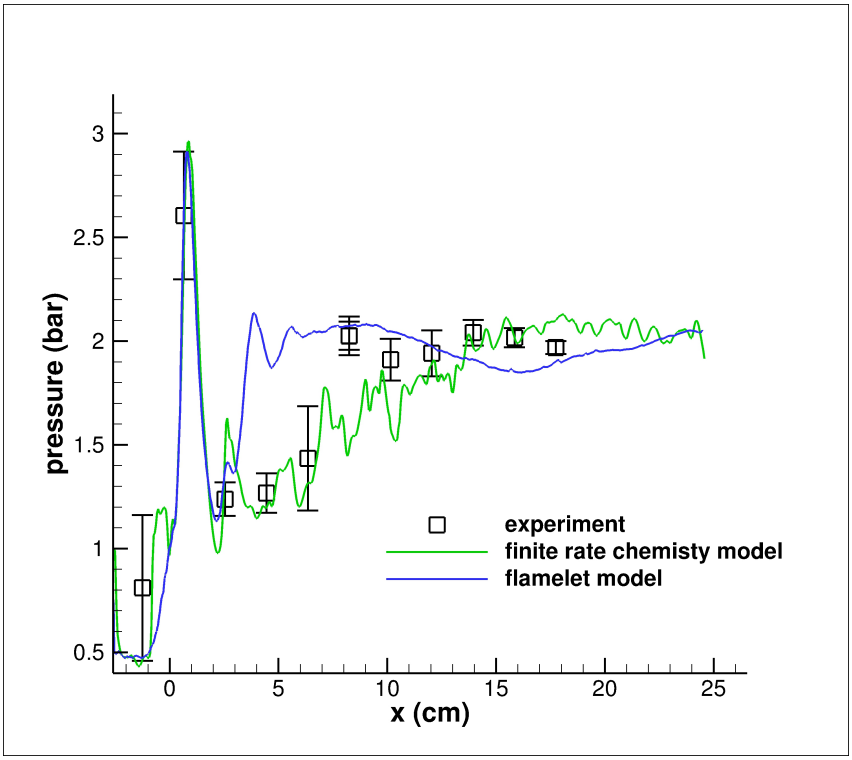


Figure 5.9: Upper wall pressure for the finite rate chemistry model, the flamelet model and experiment

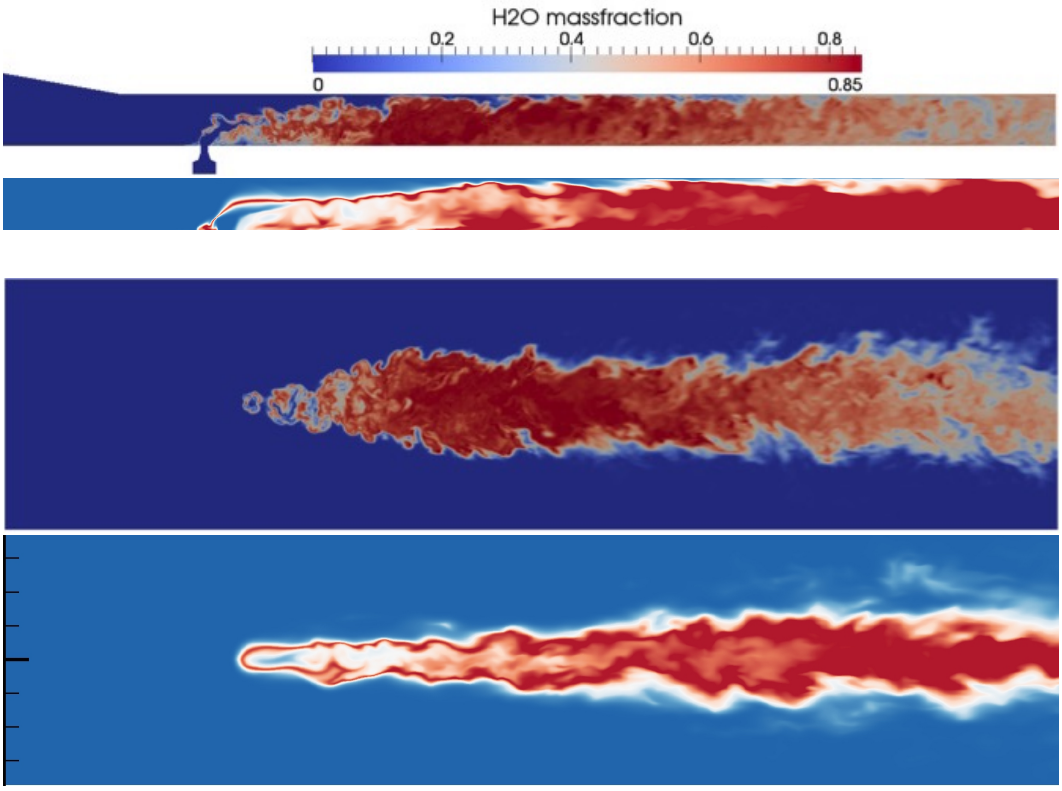


Figure 5.10: Instantaneous snapshot of mass fraction of $H_2O$ in the scramjet. Top to bolttom, frame (a) flamelet (b) finite rate chemistry, both vertical cross section. Frames (c) flamlet, (d) finite rate chemistry, both a horizontal plane.

results appear to be satisfactory, other than the lower level of OH in the simulation along the chamber wall.

### 5.4.4 Comparison of $H_2O$ Production

Fig. 5.10 shows the water content in the combustion chamber by simulation of finite rate chemistry model compared with the flamelet model. The difference appears to be due to two previously noted (see Sec. 5.4.2) features of these simulations. Namely, the delayed burning off the finite rate chemistry and its slow burning after ignition.

## 5.5 Conclusions

We see that the 3D turbulent model modifies the conclusions of Secs. 4.4, 4.5, by a further increase of the turbulent diffusion and thus a further increase in the minimal numerical mesh needed for convergence.

Extensive comparison of the finite rate chemistry and the flamelet model simulations have been conducted. Broadly speaking, these comparisons show consistency and substantial agreement between these two simulations as well as consistency with experiment. Most comparisons to experiments are qualitative, as the experiments did not calibrate the colour images of concentrations with specific concentration values. Figs. 5.11 and 5.12 show satisfactory agreement of the finite rate chemistry simulation with experiment, with the exception of a lower level of chamber

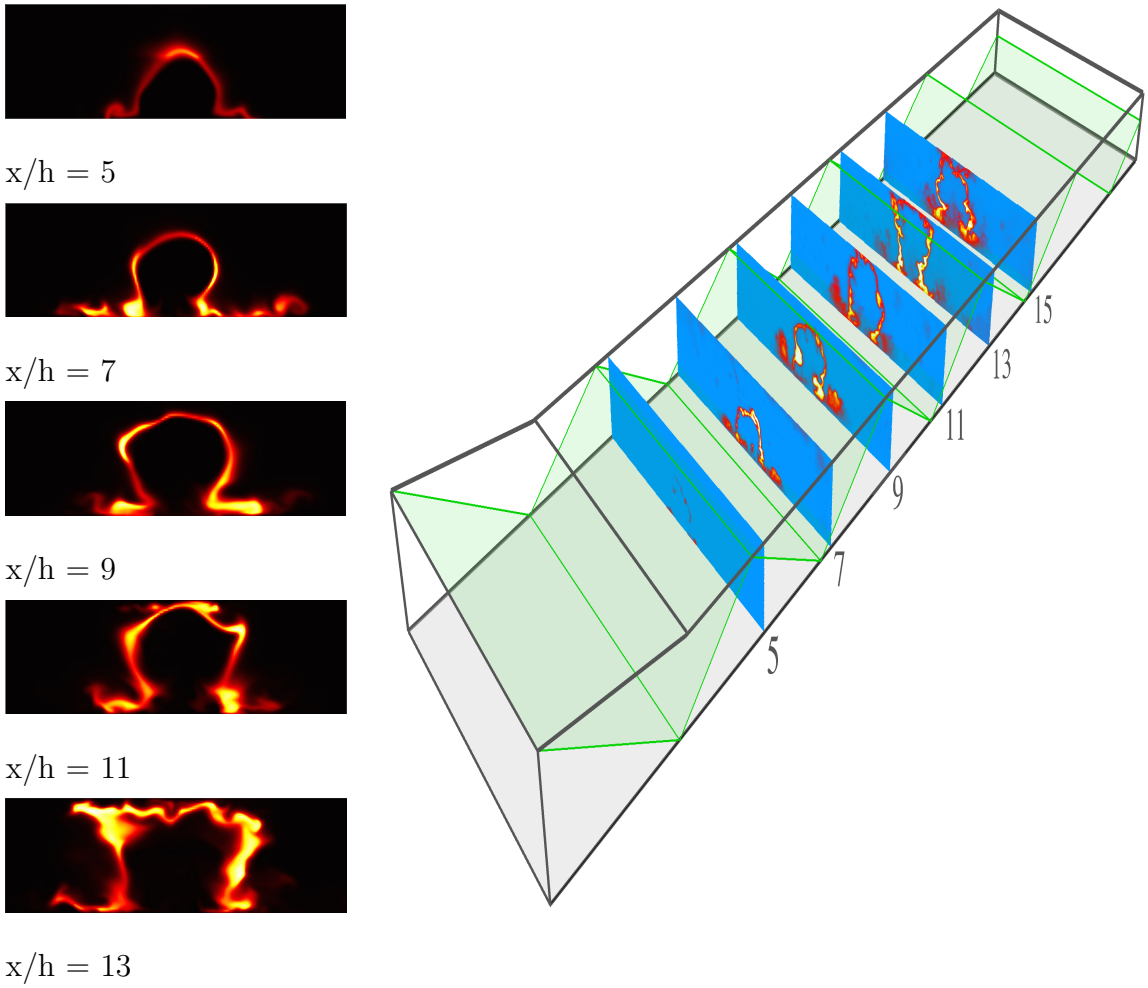


Figure 5.11: Left: Mass fraction of OH in finite rate chemistry simulation in several end-view planes corresponding to the OH PLIF data (right frame) from experiment

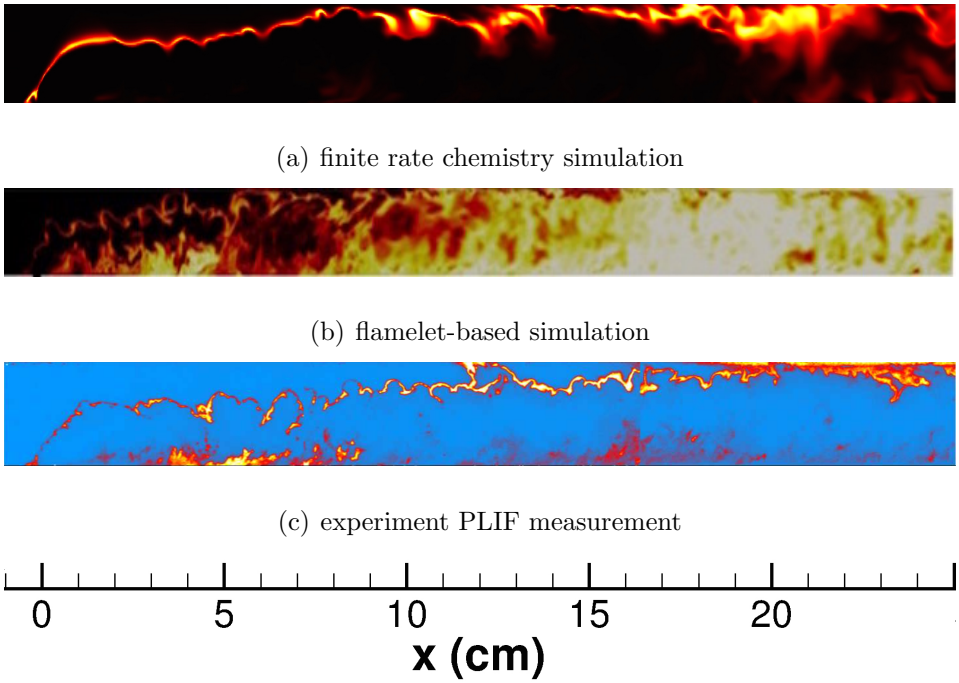


(a) finite rate chemistry simulation

(b) flamelet-based simulation

(c) experiment PLIF measurement

Figure 5.12: OH mass fraction in a vertical cross section., comparing finite rate chemistry simulation, flamelet simulation and experiment

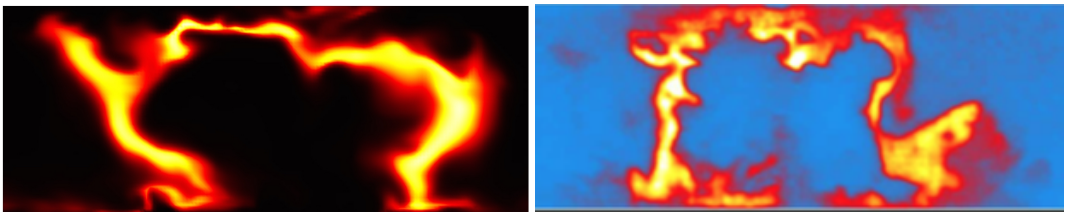

(a) finite rate chemistry simulation

(b) experiment.

Figure 5.13: OH mass fraction in end views of the combustion chamber, comparing finite rate chemistry simulation and experiment

wall burning in the simulation in Fig. 5.12. Fig. 5.10 shows a higher level of burning for the finite rate chemistry simulation, due in part to its early ignition, as noted above. Quantitative experimental data are provided by the pressure measurements on the top wall. Agreement of both simulations with this data is satisfactory with exceptions as noted.

A few consistent differences between the simulations have been noted. The finite rate chemistry simulation tends to burn less, and starts burning more slowly. The second of these properties, the slower start to the combustion, reflects a known weakness of steady flamelet models in not capturing flame ignition. Further details of comparison are not meaningful as neither simulation can be regarded as fully converged.

# Chapter 6

# Conclusions and Future Work

## 6.1 Conclusion

In this thesis, we study the physical processes, including the turbulent boundary layer, turbulent mixing and turbulent combustion, in the model scramjet combustor using Large Eddy Simulation.

In Chap. 3 we explore the turbulent boundary layer model and assess mesh convergence requirements for the averaged value of wall shear stress and heat flux through suits of two-dimensional simulations.

In Chap. 4, we examine the mesh requirement for the finite rate chemistry model to resolve the turbulent combustion through suits of one-dimensional and two-dimensional simulations. There are three prediction approaches:

(a) Convergence study of one-dimensional laminar diffusion flame. We first conduct the simulation with laminar diffusion coefficients. Later

Table 6.1: Summary of minimal mesh requirements for reduced and full chemistry.

| Flow Regime | Full Chemistry (mm) | Reduced Chemistry (mm) |
|---|---|---|
| 1D laminar flame analysis | 0.1 | 0.5 |
| 1D flame analysis with 2D turbulent diffusivity | 0.125 | 0.52 |
| 1D flame analysis with 3D turbulent diffusivity | 0.25 | 0.625 |
| 2D flame width analysis | 0.22 | 0.34 |

we add the turbulent diffusion coefficient from 2D and 3D simulation onto laminar diffusion coefficient and get a less stringent criteria.

(b) Two-dimensional flame width analysis.

The results are summerized in Tab. 6.1. Top four row of Tab. 6.1 predict the mesh needed for the finite rate chemistry model to resolve the chemical reactions. They show some level of consistency (although not perfect consistency). We also find that reduced chemistry, which removes the fast and transient reactions, has a less stringent mesh requirement than the full chemistry.

In Chap. 5 we applied the predictions made in Chap. 3 and Chap. 4 to the 3D simulation of model scramjet combustor. TKE analysis and turbulent resolution analysis in 3D scramjet simulation shows the turbulence in them combustion chamber is well resolved.

The simulation result are compared with the experiment and Stanford's simulation. Qualitative comparison of OH mass fractions show satisfactory agreement of the finite rate chemistry simulation with experiment,

with exceptions of a lower level of chamber wall burning and a higher level of burning near outlet. Quantitative measurements of top wall pressure shows satisfactory agreement of both simulations with experiment except for: flamelet simulation has a higher level of burning due to early ignition; finite rate chemistry model has lower level of burning due to ignition delay. The satisfactory agreement of simulation with the Gamba's experiment data verifies predictions made in Chap. 3 and Chap. 4.

## 6.2 Recommendation for Future Work

Although the current scramjet simulation result presented in this thesis have demonstrated good agreement with the experiment, it could be further developed in a number of ways.

First recommendation is the implementation of local mesh refinement functionality into current FronTier package. The flame thickness list in Tab. 4.5 is the averaged flame thickness in the combustion chamber. Actually the flames near the $H_2$ inflow nozzle has a smaller width than the averaged value. So it is better to have local mesh refinement near $H_2$ inflow nozzle. We can also have less error in the calculation of the wall shear stress and heat flux with mesh refinement near wall.

Another recommendation is the time efficiency optimization of FronTier code especially in

(a) Parallel Computing.

The parallel computing of scramjet project is realized by MPI. In

the implemenation of parallel computing, the scramjet simulation domain are split into several uniform rectangles (subdomains) and each processor is in charge of one subdomain. This kind of splitting is not time efficient because the computational burden is not evenly distributed on these subdomains. Some subdomains contains lots of "obstacle states" and are fast than others. Thus lots of computational resources are wasted when the fast subdomains stops and waits for the slow subdomains. Thus a better subdomain splitting algorithm are needed.

(b) Computation of EOS and transport coefficients.

In scramjet simulation, EOS and transport coefficient functions are called quite frequently by hyperbolic, parabolic, boundary layer and chemistry modules. Calculation of the EOS parameters and the transport coefficients for gas mixtures require lots of computational resources. Optimization of the EOS and transport coefficients code will greatly reduce computational cost.

# Appendices

# Appendix A

# Mathematical Derivation of the Thin Boundary Layer Model for Compressible Flow

In this section we shows the derivation the Thin Boundary Layer Model of [4] from the Navier-Stokes equation. The compressible Navier-Stokes equation expresses conservation of mass, momentum, and energy. The law of conservation of mass is

$$\frac{\partial \rho}{\partial t} + \frac{\partial}{\partial x_j}\Big(\rho u_j\Big) = 0 \ . \tag{A.1}$$

Conservation of momentum is given by the equation

$$\frac{\partial}{\partial t}\Big(\rho u_i\Big) + \frac{\partial}{\partial x_j}\Big(\rho u_i u_j\Big) + \frac{\partial p}{\partial x_i} = \frac{\partial \tau_{ij}}{\partial x_j} \ . \tag{A.2}$$

The equation for conservation of energy is:

$$\frac{\partial E}{\partial t} + \frac{\partial\big[\,(E+p)\,u_j\big]}{\partial x_j} = \frac{\partial}{\partial x_j}\Big(\tau_{ij}u_i\Big) - \frac{\partial q_j}{\partial x_j} \ . \tag{A.3}$$

For a Newtonian fluid, assuming Stokes Law for mono-atomic gases, the viscous stress is given by:

$$\tau_{ij} = 2\mu S^*_{ij} = \mu\left[\left(\frac{\partial u_i}{\partial x_j} + \frac{\partial u_j}{\partial x_i}\right) - \frac{2}{3}\delta_{ij}\frac{\partial u_k}{\partial x_k}\right] \ . \tag{A.4}$$

The energy equation could also be written in terms of physical variable $h_b$:

$$\rho\left(\frac{\partial h_b}{\partial t} + u_i\frac{\partial h_b}{\partial x_i}\right) = \frac{\partial p}{\partial t} + \frac{\partial}{\partial x_j}\left(\tau_{ij}u_i\right) - \frac{\partial q_j}{\partial x_j} \ . \tag{A.5}$$

In this equation, $h_b$ is defined as:

$$h_b = h + \frac{1}{2}u_k^2 \ , \tag{A.6}$$

and the specific enthalpy is given by

$$h = e + \frac{p}{\rho} \tag{A.7}$$

where

$$e = c_v T \tag{A.8}$$

is the specific internal energy. Some authors define $h_b$ to be the total enthalpy and $h$ as the static enthalpy. We assume the perfect gas law is applicable here, which assumes that

$$\frac{p}{\rho} = \frac{R}{M}T = (\gamma - 1)\, c_v T \ , \tag{A.9}$$

$$h = c_v T + (\gamma - 1)\, c_v T = \gamma c_v T = c_p T \ . \tag{A.10}$$

Thus

$$h_b = c_p T + \frac{1}{2}u_k^2 \ . \tag{A.11}$$

The heat flux, $\dot{q}$ is given by Fourier's law

$$\dot{q} = -k\nabla T \ . \tag{A.12}$$

Within the turbulent boundary layer, we replace the instantaneous quantities in the Eqs. (A.1 - A.3). by the sum of their mean and fluctuating parts. We introduce the Reynolds decomposition for $\rho$ and $p$ and the Favre decomposition for $T$, $u_i$, $h_b$ and $h$. By taking an average of the governing equations we have:

$$\frac{\partial \bar{\rho}}{\partial t} + \frac{\partial}{\partial x_j}\left(\bar{\rho}\widetilde{u_j}\right) = 0 \ , \tag{A.13}$$

$$\begin{aligned}
&\frac{\partial}{\partial t}\left(\bar{\rho}\widetilde{u_j}\right) + \frac{\partial}{\partial x_j}\left(\bar{\rho}\widetilde{u_i}\widetilde{u_j}\right) = -\frac{\partial \bar{p}}{\partial x_i} + \frac{\partial \overline{\tau}_{ij}}{\partial x_j} - \frac{\partial}{\partial x_j}\left(\overline{\rho u_i'' u_j''}\right) \ , \\
&\frac{\partial}{\partial t}\left[\bar{\rho}\widetilde{h_b}\right] + \frac{\partial}{\partial x_j}\left[\bar{\rho}\widetilde{u_j}\widetilde{h_b} + \overline{\rho u_j'' h_b''} - \overline{\tau_{ij}u_i} + \overline{q_j}\right] = \frac{\partial P}{\partial t} \ ,
\end{aligned} \tag{A.14}$$

where the density averaged $h_b$ is give by

$$\widetilde{h}_b = c_v\widetilde{T} + \frac{\widetilde{u}_k\widetilde{u}_k}{2} + \frac{\overline{P}}{\overline{\rho}} + \frac{\widetilde{u_k^{''}}}{2} \ . \tag{A.15}$$

Next we substitute the unknown terms into the known terms. For example we have

$$\overline{\tau_{ji}} = \widetilde{\tau_{ji}} + \overline{\tau_{ji}^{''}} \ , \tag{A.16}$$

$$\overline{\rho u_j^{''} h_b} = \overline{\rho u_j^{''}(c_pT + \frac{1}{2}u_i^2)} == \overline{c_p\rho u_i^{''}T} + \widetilde{u}_i\overline{\rho u_i^{''}u_j^{''}} + \frac{1}{2}\overline{\rho u^{''2}_i u_j^{''}} \ , \tag{A.17}$$

$$\overline{q_j} = -k\frac{\partial\overline{T}}{\partial x_j} = -k\frac{\partial\widetilde{T}}{\partial x_j} - k\frac{\partial T^{''}}{\partial x_j} \ , \tag{A.18}$$

and

$$\overline{u_i\tau_{ij}} = \widetilde{u}_i\widetilde{\tau_{ij}} + \overline{u_i^{''}\tau_{ij}} + \widetilde{u}_i\overline{\tau_{ij}^{''}} \ . \tag{A.19}$$

Then we rewrite equations Eqs. (A.1 - A.3) as :

$$\frac{\partial\bar{\rho}}{\partial t} + \frac{\partial}{\partial x_j}\left(\bar{\rho}\widetilde{u_j}\right) = 0 \ , \tag{A.20}$$

$$\frac{\partial}{\partial t}\left(\bar{\rho}\widetilde{u_j}\right) + \frac{\partial}{\partial x_j}\left(\bar{\rho}\widetilde{u_i}\widetilde{u_j} + \overline{\rho u_i^{''}u_j^{''}} - \widetilde{\tau}_{ij} - \overline{\tau_{ij}^{''}}\right) = -\frac{\partial\bar{p}}{\partial x_i} \ , \tag{A.21}$$

$$\begin{aligned}\frac{\partial}{\partial t}\left(\overline{\rho}h_b\right) + \frac{\partial}{\partial x_j}\left(\overline{\rho}\widetilde{u_j}\widetilde{h}_b + \widetilde{u}_i\overline{\rho u_i^{''}u_j^{''}} + \frac{1}{2}\overline{\rho u_j^{''}u_i^{''}u_i^{''}}\right)\\ + \frac{\partial}{\partial x_j}\left(-c_p\overline{\rho u_j^{''}T} - k\frac{\partial\widetilde{T}}{\partial x_j} - \widetilde{u}_i\widetilde{\tau}_{ij} - k\frac{\partial\overline{T^{''}}}{\partial x_j} - \widetilde{\tau}_{ij} - \overline{\tau_{ij}^{''}}\right) = \frac{\partial\overline{p}}{\partial t} \ .\end{aligned} \tag{A.22}$$

These are open equations in that they contain new undefined terms. Closure requires same assumptions. The Reynolds stress $\tau_{ij}^{turb} = \overline{\rho u_i^{''}u_j^{''}}$ can be modelled using an eddy-viscosity assumption:

$$\tau_{ij}^{turb} = -\overline{\rho u_i^{''}u_j^{''}} \approx 2\mu_t\widetilde{S}_{ij}^{*} - \frac{2}{3}\rho k\delta_{ij} \ , \tag{A.23}$$

where $\mu_t$ is the turbulent viscosity. The term $c_p\overline{\rho u_j^{''}T}$ corresponding to turbulent transport of heat, can be modelling using a gradient approximation for the turbulent-flux:

$$q_j^{turb} = c_p\overline{\rho u_j^{''}T} = c_p\frac{\mu_t}{\mathrm{Pr}_t}\frac{\partial\widetilde{T}}{\partial x_j} \ . \tag{A.24}$$

Here $Pr_t$ is the turbulent Prandtl number, which is taken to be a constant with value 0.9. The term $\tau_{ij}^{''}$ is neglected if $\mid \widetilde{\tau}_{ij} \mid >> \mid \overline{\tau}_{ij}^{''} \mid$ which is true for nearly all flows. The terms $c_p k \frac{\partial \overline{T^{''}}}{\partial x_i}$, $\frac{\overline{\rho u_j^{''} u_i^{''} u_i^{''}}}{2}$ and $\widetilde{\tau_{Ia}} \overline{u_i^{''}}$ are neglected for similar reasons. Thus the filtered averaged equations for compressible flow become:

$$\frac{\partial \overline{\rho}}{\partial t} + \frac{\partial}{\partial x_j} \left[ \rho \widetilde{u}_i \right] = 0 \ , \tag{A.25}$$

$$\frac{\rho \widetilde{u}_i}{\partial t} + \frac{\partial}{\partial x_j} \left[ \overline{\rho} \widetilde{u}_i \widetilde{u}_j - (\mu + \mu_t) \left( \frac{\partial \widetilde{u}_i}{\partial x_j} + \frac{\partial \widetilde{u}_j}{\partial x_i} - \frac{2}{3} \frac{\partial \widetilde{u}_k}{\partial x_k} \delta_{ij} \right) \right] + \frac{\partial p}{\partial x_i} = 0 \ , \tag{A.26}$$

and

$$\frac{\rho \widetilde{h}_b}{\partial t} + \frac{\partial}{\partial x_j} \left[ \overline{\rho} \widetilde{u}_j \widetilde{h}_b - \widetilde{u}_i \left( \mu + \mu_t \right) \left( \frac{\partial \widetilde{u}_i}{\partial x_j} + \frac{\partial \widetilde{u}_j}{\partial x_i} - \frac{2}{3} \frac{\partial \widetilde{u}_k}{\partial x_k} \delta_{ij} \right) + \left( c_p \frac{\mu}{Pr} + k \right) \frac{\partial \widetilde{T}}{\partial x_j} \right] = \frac{\partial p}{\partial t} \ . \tag{A.27}$$

For the boundary layer flow, we use an order-of-magnitude analysis to derive a simplified system of equations. If $y$ is the wall normal direction, we assume that

$$\widetilde{v} \ll \widetilde{u}, \, \widetilde{w} \ , \ \frac{\partial}{\partial x}, \frac{\partial}{\partial z} \ll \frac{\partial}{\partial y}$$

Omitting lower order terms, we have the new boundary layer equations (for three dimensional flow):

$$\frac{\partial}{\partial x} \left( \overline{\rho} \widetilde{u} \right) + \frac{\partial}{\partial y} \left( \overline{\rho} \widetilde{v} \right) + \frac{\partial}{\partial z} \left( \overline{\rho} \widetilde{w} \right) = 0 \ , \tag{A.28}$$

$$\frac{\rho \widetilde{u}}{\partial t} + \overline{\rho} \widetilde{u} \frac{\partial \widetilde{u}}{\partial x} + \overline{\rho} \widetilde{w} \frac{\partial \widetilde{w}}{\partial z} + \overline{\rho} \widetilde{v} \frac{\partial \widetilde{u}}{\partial y} + \frac{\partial \widetilde{p}}{\partial x} = \frac{\partial}{\partial y} \left( \mu + \mu_t \right) \frac{\partial \widetilde{u}}{\partial y} \ , \tag{A.29}$$

$$\frac{\rho \widetilde{h}_b}{\partial t} + \overline{\rho} \widetilde{u} \frac{\partial \widetilde{h}_b}{\partial x} + \overline{\rho} \widetilde{v} \frac{\partial \widetilde{h}_b}{\partial y} + \overline{\rho} \widetilde{w} \frac{\partial \widetilde{h}_b}{\partial z} = \frac{\partial}{\partial y} \left[ \widetilde{u} \left( \mu + \mu_t \right) \frac{\partial \widetilde{u}}{\partial y} + \left( k + c_p \frac{\mu_t}{Pr_t} \frac{\partial \widetilde{T}}{\partial y} \right) \right] + \frac{\partial p}{\partial t} \ . \tag{A.30}$$

Our model is a equilibrium stress model without pressure gradient so that the left hand side of the momentum equation is zero. According to Bernoulli's law, $h_b = h + \frac{u_k^2}{2}$ along a stream line is constant, so the left hand side of the energy equation is zero. So our boundary layer equation is further simplified to become:

$$\frac{\partial}{\partial y} \left[ \left( \mu + \mu_t \right) \frac{\partial u}{\partial y} \right] = 0 \ , \tag{A.31}$$

$$\frac{\partial}{\partial y}\left[c_p\left(\frac{\mu_t}{Pr_t}+\frac{\mu}{Pr}\right)\frac{\partial T}{\partial y}+(\mu+\mu_t)\,u\frac{\partial u}{\partial y}\right]=0\ . \tag{A.32}$$

# Bibliography


[1] Laminar diffusion flames, retrieved from http://arrow.utias.utoronto.ca/ ogulder/classnotes8.pdf.

[2] AJ Aspden, MS Day, and JB Bell. Turbulence–flame interactions in lean premixed hydrogen: transition to the distributed burning regime. *Journal of Fluid mechanics*, 680:287–320, 2011.

[3] G Balakrishnan, MD Smooke, and FA Williams. A numerical investigation of extinction and ignition limits in laminar nonpremixed counterflowing hydrogen-air streams for both elementary and reduced chemistry. *Combustion and Flame*, 102(3):329–340, 1995.

[4] Elias Balaras, Carlo Benocci, and Ugo Piomelli. Two-layer approximate boundary conditions for large-eddy simulations. *AIAA journal*, 34(6):1111–1119, 1996.

[5] JB Bell, MS Day, and MJ Lijewski. Simulation of nitrogen emissions in a premixed hydrogen flame stabilized on a low swirl burner. *Proceedings of the Combustion Institute*, 34(1):1173–1182, 2013.

[6] M Berglund, E Fedina, C Fureby, J Tegner, and V Sabel'Nikov. Finite rate chemistry large-eddy simulation of self-ignition in supersonic combustion ramjet. *AIAA journal*, 48(3):540–550, 2010.

[7] G. Boffetta. Energy and enstrophy fluxes in the double cascade of two-dimensional turbulence. *J. Fluid Mech*, 589:253–260, 2007.

[8] Pierre Boivin, Carmen Jiménez, Antonio L Sánchez, and Forman A Williams. A four-step reduced mechanism for syngas combustion. *Combustion and Flame*, 158(6):1059–1063, 2011.

[9] G Boudier, LYM Gicquel, and TJ Poinsot. Effects of mesh resolution on large eddy simulation of reacting flows in complex geometry combustors. *Combustion and Flame*, 155(1):196–214, 2008.

[10] Richard S Brokaw. *Viscosity of gas mixtures*, volume 4496. National Aeronautics and Space Administration, 1968.

[11] Center for Turbulence Research: Stanford University. *Dynamically thickened flame LES model for premixed and non-premixed turbulent combustion*. Citeseer, 2000.

[12] W Chan, Hemanth Kolla, Matthias Ihme, and J Chen. Analysis of a jet in crossflow using an unsteady flamelet model. In *Spring Technical Meeting of the Central States Section of the Combustion Institute*, 2012.

[13] Dean Khalil Chapman. Computational aerodynamics development and outlook. *AIAA journal*, 17(12):1293–1313, 1979.

[14] Dmitry Davidenko, Iskender Gokalp, Emmanuel Dufour, and Philippe Magre. Numerical simulation of hydrogen supersonic combustion and validation of computational approach. *AIAA Paper*, 7033:12, 2003.

[15] Reaction Design. *CHEMKIN Theory Manual*. San Diego, CA, 2007.

[16] M Frenklach, H Wang, C Yu, M Goldenberg, C Bowman, R Hanson, D Davidson, E Chang, G Smith, D Golden, et al. Gri-mech 1.2-an optimized detailed chemical reaction mechanism for methane combustion. Technical Report 1, GRI Tech. Report, 1995.

[17] Ronald S Fry. A century of ramjet propulsion technology evolution. *Journal of propulsion and power*, 20(1):27–58, 2004.

[18] Michiko Furudate, B Lee, and I Jeung. *Computation of hyshot scram jet flows in the T4 experiments*. Number 3353. American Institute of Aeronautics and Astronautics, 2005.

[19] Mohamed Gad-el Hak. *Mems: Applications*. CRC press, 2005.

[20] M. Gamba, M. G. Mungal, and R. K. Hanson. Ignition and near-wall burning in transverse hydrogen jets in supersonic crossflow. In *AIAA-2011-0319*, 2011. 49th AIAA Aerospace Sciences Meeting and Aerospace Exposition.

[21] Mirko Gamba, Victor A Miller, M Godfrey Mungal, and Ronald K Hanson. Combustion characteristics of an inlet/supersonic combustor model. In *50th AIAA Aerospace Sciences Meeting Including the New Horizons Forum and Aerospace Exposition (American Institute of Aeronautics and Astronautics, 2012), paper AIAA*, volume 0612. American Institute of Aeronautics and Astronautics, 2012.

[22] Jade Rachele Garcia, Pedro Mellado, and Bjorn Stevens. *Analysis of the surface layer and the entrainment zone of a convective boundary layer using direct numerical simulation*. PhD thesis, University of Hamburg, 2014.

[23] AD Gardner, Klaus Hannemann, A Pauli, and Johan Steelant. Ground testing of the hyshot supersonic combustion flight experiment in heg. In *Shock Waves*, pages 329–334. Springer, 2005.

[24] M. Germano, U. Piomelli, P. Moin, and W. H. Cabot. A dynamic subgrid scale eddy viscosity model. *Phys. Fluids A*, 3:1760–1765, 1991.

[25] A. Harten, S. Osher, B. Engquist, and S. Chakravarthy. Uniformly high order accurate essentially non-oscillatory schemes, III. *J. Comput. Phys.*, 71:231–303, 1987.

[26] D. J. Hill, C. Pantano, and D. L. Pullin. Large-eddy simulation and multiscale modeling of a Richtmyer-Meshkov instability with reshock. *J. Fluid Mech*, 557:29–61, 2006.

[27] Klaus A Hoffmann and Steve T Chiang. *Computational fluid dynamics, Vol. III*. Wichita, KS: Engineering Education System, 2000.

[28] Zekai Hong, David F Davidson, and Ronald K Hanson. An improved h 2/o 2 mechanism based on recent shock tube/laser absorption measurements. *Combustion and Flame*, 158(4):633–644, 2011.

[29] Antonella Ingenito, Claudio Bruno, and Donato Cecere. Les of the hyshot scramjet combustor. *AIAA paper*, 758, January 2010.

[30] Casimir J Jachimowski. *An analytical study of the hydrogen-air reaction mechanism with application to scramjet combustion*, volume 2791. National Aeronautics and Space Administration, Scientific and Technical Information Division, 1988.

[31] G. Jiang and C.-W. Shu. of weighted ENO schemes. *J. Comput. Phys.*, 126:202–228, 1996.

[32] Soshi Kawai and Johan Larsson. Wall-modeling in large eddy simulation: Length scales, grid resolution, and accuracy. *Physics of Fluids*, 24(1):015105, 2012.

[33] M. Klein, A. Sadiki, and J. Janicka. A digital filter based generation of inflow data for spatially developing direct numerical or large eddy simulations. *J. Comput. Phys.*, 186:652–665, April 2003.

[34] Robert H Kraichnan. Inertial ranges in two-dimensional turbulence. Technical report, DTIC Document, 1967.

[35] Kenneth Kuan-yun Kuo and Ragini Acharya. *Fundamentals of Turbulent and Multi-Phase Combustion*. John Wiley & Sons, 2012.

[36] J. Larsson. Large eddy simulation of the hyshot ii scramjet combustor using a supersonic flamelet model. *AIAA Joint Propulsion Conference*,

4201:2012, 2012. Center for Turbulence Research, NASA Ames/Stanford University.

[37] Johan Larsson. *Towards Large Eddy Simulation of Boundary Layer Flows at High Reynolds Number: Statistical Modeling of the Inner Layer*. PhD thesis, University of waterloo, 2006.

[38] Johan Larsson, Stuart Laurence, Iván Bermejo-Moreno, Julien Bodart, Sebastian Karl, and Ronan Vicquelin. Incipient thermal choking and stable shock-train formation in the heat-release region of a scramjet combustor. part ii: Large eddy simulations. *Combustion and Flame*, 162:907–920, 2014.

[39] Douglas K Lilly. A proposed modification of the germano subgrid-scale closure method. *Physics of Fluids A: Fluid Dynamics (1989-1993)*, 4(3):633–635, 1992.

[40] H. Lim, Y. Yu, J. Glimm, X. L. Li, and D. H. Sharp. Subgrid models for mass and thermal diffusion in turbulent mixing. *Physica Scripta*, T142:014062, 2010. Stony Brook Preprint SUNYSB-AMS-08-07 and Los Alamos National Laboratory Preprint LA-UR 08-07725.

[41] Xu-Dong Liu, Stanley Osher, and Tony Chan. Weighted essentially non-oscillatory schemes. *Journal of computational physics*, 115(1):200–212, 1994.

[42] Thomas S Lund, Xiaohua Wu, and Kyle D Squires. Generation of turbulent inflow data for spatially-developing boundary layer simulations. *Journal of Computational Physics*, 140(2):233–258, 1998.

[43] B. J. McBride, S. Gordon, and M. A. Reno. Coefficients for calculating thermodynamic and transport properties of individual species. TM 4513, NASA Report, 1993.

[44] Jeff McGuire, Russell Boyce, and Neil Mudford. Comparison of computational and experimental studies on shock induced ignition in scramjets. *AIAA Paper*, 3394:2005, 2005.

[45] J. Melvin, P. Rao, R. Kaufman, H. Lim, Y. Yu, J. Glimm, and D. H. Sharp. Turbulent transport at high reynolds numbers in an ICF context. *Journal of Fluids Engineering*, 136(9)(9):091206, 2014.

[46] Charles Meneveau, Thomas S Lund, and William H Cabot. A lagrangian dynamic subgrid-scale model of turbulence. *Journal of Fluid Mechanics*, 319:353–385, 1996.

[47] Robert H Nichols. Turbulence models and their application to complex flows. *University of Alabama at Birmingham, Revision*, 4:89, 2010.

[48] C Pantano. Direct simulation of non-premixed flame extinction in a methane–air jet with reduced chemistry. *Journal of Fluid Mechanics*, 514:231–270, 2004.

[49] René Pecnik, Vincent E Terrapon, Frank Ham, Gianluca Iaccarino, and Heinz Pitsch. Reynolds-averaged navier-stokes simulations of the hyshot ii scramjet. *AIAA journal*, 50(8):1717–1732, 2012.

[50] Norbert Peters. Laminar diffusion flamelet models in non-premixed turbulent combustion. *Progress in energy and combustion science*, 10(3):319–339, 1984.

[51] Norbert Peters. *Turbulent combustion*. Cambridge university press, 2000.

[52] Charles D Pierce and Parviz Moin. Progress-variable approach for large-eddy simulation of non-premixed turbulent combustion. *Journal of Fluid Mechanics*, 504:73–97, 2004.

[53] Ugo Piomelli and Elias Balaras. Wall-layer models for large-eddy simulations. *Annual review of fluid mechanics*, 2002.

[54] H Pitsch. Improved pollutant predictions in large-eddy simulations of turbulent non-premixed combustion by considering scalar dissipation rate fluctuations. *Proceedings of the Combustion Institute*, 29(2):1971–1978, 2002.

[55] Heinz Pitsch. Unsteady flamelet modeling of differential diffusion in turbulent jet diffusion flames. *Combustion and Flame*, 3(3):358–374, 2000.

[56] T. Poinsot and D. Veynante. *Theoretical and Numerical Combustion*. Edwards, Philadelphia, 2005.

[57] Stephen B. Pope. *Turbulent Flows*. Cambridge University Press, 2000.

[58] LF Richardson. Weather prediction by numerical process cambridge university press. *Cambridge*, 1922.

[59] Bernd Rogg. *Reduced kinetic mechanisms for applications in combustion systems*. Springer Science and Business Media, 1993.

[60] Corin Segal. *The scramjet engine: processes and characteristics*, volume 25. Cambridge University Press, 2009.

[61] Chi-Wang Shu. Finite volume weno schemes.

[62] J. Smagorinsky. General circulation experiments with the primitive equations. *Mon. Weather Rev.*, 91:99–165, 1963.

[63] Philippe R Spalart. Direct simulation of a turbulent boundary layer up to r $\theta$= 1410. *Journal of Fluid Mechanics*, 187:61–98, 1988.

[64] Hendrik Tennekes and John Leask Lumley. *A first course in turbulence*. MIT press, 1972.

[65] Emile Touber and Neil D Sandham. Large-eddy simulation of low-frequency unsteadiness in a turbulent shock-induced separation bubble. *Theoretical and Computational Fluid Dynamics*, 23(2):79–107, 2009.

[66] Gerald Urbin and Doyle Knight. Large-eddy simulation of a supersonic boundary layer using an unstructured grid. *AIAA journal*, 39(7):1288–1295, 2001.

[67] AW Vreman. An eddy-viscosity subgrid-scale model for turbulent shear flow: Algebraic theory and applications. *Physics of Fluids*, 16(10):3670–3681, 2004.

[68] FA Williams. Recent advances in theoretical descriptions of turbulent diffusion flames. In S. Murthy, editor, *Turbulent mixing in nonreactive and reactive flows*, pages 189–208. Springer, 1975.

[69] FA Williams. On the reaction zone thickness of premixed laminar flame. *Combustion science and technology*, 43(5-6):329–332, 1985.

[70] FA Williams et al. Chemical-kinetic mechanisms for combustion applications, 2015.

[71] Zheng-Tong Xie and Ian P Castro. Efficient generation of inflow conditions for large eddy simulation of street-scale flows. *Flow, turbulence and combustion*, 81(3):449–470, 2008.

[72] Ying Xu. *Numerical Modeling and Combustion Studies of Scramjet Problem*. PhD thesis, State University of New York at Stony Brook, 2014.

[73] RA Yetter, FL Dryer, and H Rabitz. A comprehensive reaction mechanism for carbon monoxide/hydrogen/oxygen kinetics. *Combustion Science and Technology*, 79(1-3):97–128, 1991.

[74] Akira Yoshizawa. Statistical theory for compressible turbulent shear flows, with the application to subgrid modeling. *Physics of Fluids*, 29(7):2152–2164, 1986.